Delft University of Technology

Structured light assisted coherent fourier scatterometry for physical parameter retrieval of nanostructures

Dou, X.

DOI
10.4233/uuid:2ac46a6e-c97a-495a-b9d3-f65ec8c7cf2b

Publication date
2024

Document Version
Final published version

Important note
To cite this publication, please use the final published version (if applicable).
Please check the document version above.

STRUCTURED LIGHT ASSISTED COHERENT FOURIER SCATTEROMETRY FOR PHYSICAL PARAMETER RETRIEVAL OF NANOSTRUCTURES

STRUCTURED LIGHT ASSISTED COHERENT FOURIER SCATTEROMETRY FOR PHYSICAL PARAMETER RETRIEVAL OF NANOSTRUCTURES

Dissertation

for the purpose of obtaining the degree of doctor
at Delft University of Technology
by the authority of the Rector Magnificus, prof. dr. ir. T.H.J.J. van der Hagen,
chair of the Board for Doctorates
to be defended publicly on Monday 15 April 2024 at 12:30 o'clock

by

Xiujie DOU

Master in Optical Engineering,
Shenzhen University, Shenzhen, China
born in Xingtai, China

This dissertation has been approved by the promotors.

Composition of the doctoral committee:

Rector Magnificus,	chairperson
Prof. dr. H.P. Urbach,	Technische Universiteit Delft, *promotor*
Dr. ir. S.F. Pereira,	Technische Universiteit Delft, *promotor*
Prof. dr. X.C. Yuan,	Shenzhen University, China, *promotor*

Independent members:

Prof. dr. B.R. Brandl	Universiteit Leiden
Prof. dr. W.M.J.M. Coene	Technische Universiteit Delft and ASML Holding N.V.
Dr. N. Bhattacharya	Technische Universiteit Delft
Dr. S. Witte	Advanced Research Center for Nanolithography

Other members:

Dr. C.W. Hagen	Technische Universiteit Delft

Prof. dr. C. Min of Shenzhen University has contributed greatly to the preparation of this dissertation.

An electronic copy of this dissertation is available at https://repository.tudelft.nl/.

Science is a way of thinking much more than it is a body of knowledge.

Carl Sagan

CONTENTS

ABBREVIATIONS

AFM   Atomic Force Microscope

CCD   Charge Coupled Device

CD-SEM   Critical Dimension Scanning Electron Microscope

CD   Critical Dimension

CFS   Coherent Fourier Scatterometry

CVB   Cylindrical Vector Beam

DoF   Degree of Freedom

DUV   Deep Ultraviolet

EUV   Extreme Ultraviolet

FDTD   Finite-Difference Time-Domain

FEM   Finite Element Method

FIB   Focused Ion Beam

FWHM   Full Width at Half Maximum

HG   Hermite-Gaussian

IC   Integrated Circuit

LG   Laguerre-Gaussian

LH   Left-handed

LOS   Longitudinal Optical Singularity

LPB   Linearly Polarized Beam

NA   Numerical Aperture

OAM   Orbital Angular Momentum

OS   Optical Scatterometry

OV   Optical Vortex

PB　　Pancharactnam-Berry

PML　Perfectly Matched Layer

PS　　Poincaré Sphere

RCWA　Rigorous Coupled Wave Analysis

RH　　Right-handed

RPB　Radially Polarized Beam

SEM　Scanning Electron Microscope

SNOM　Scanning Near-field Optical Microscopy

SoP　State of Polarization

STM　Scanning Tunneling Microscope

SWA　Side-wall Angle

TCs　Topological Charges

TEM　Transmission Electron Microscope

TOS　Transversal Optical Singularity

UV　　Ultraviolet

VP　　Vortex waveplate

SUMMARY

In the semiconductor industry, the minimum element size has stepped into nanometer level. To keep the functionality of fabricated nanostructures, there is a huge demand of a technique that can provide non-destructive inspection and allow for in-line or in-situ monitoring during the manufacturing process. Optical scatterometry, which uses the far-field optical scattering information to retrieve the geometrical features of a structure, is a suitable method. As a non-imaging technique, optical scatterometry does not produce images of the illuminated object. Optical scatterometry relies on retrieving nanostructure profile parameters by continuously comparing the given set of predicted signatures expected from a scattering experiment with the actual measured ones. Because we parametrize the structure with a limited set of parameters (i.e. we use prior knowledge of the structure), we can reconstruct the structure with a resolution beyond the diffraction limit. This technique is particularly valuable for characterizing micro- and nano-scale structures that are commonly found in semiconductor devices and integrated circuits.

Coherent Fourier scatterometry (CFS) occupies a very important position in the field of scatterometry, and uses a coherent beam that is focused by a lens to illuminate the structure. The scattering light is then recorded and analyzed at the Fourier plane. CFS has been used for detecting isolated defects on surfaces and determine critical dimensions such as sidewall angle, height and width of printed structures such as lines, gratings, and trenches.

The optical field generation and modulation is an essential topic for coherent beams. Taking this as the standpoint, we further developed and extended the applications of CFS technique in the realm of morphology reconstruction for nanostructures. In this thesis, the primary focus of the study is on exploring aspects such as the generation of a desired light beam, the effect of polarization and optical singularity as extra tools for the identification of certain parameters of nanostructures that have found to be challenging when using uniform light beams.

In Chapter 1, we introduce the current development status and metrology demands of the semiconductor chip industry. Principles and characteristics of the existing methods, including the electron microscopy, scanning probe microscopy, and optical scatterometry, are sketched. Moreover, the basic theories of structured optical fields, from physical properties to generation approach, are formulated.

As the optical field modulation is the central issue in this thesis, the fundamental theory of the relevant methods, as well as the numerical simulation methods, are introduced in Chapter 2. On this basis, we generate a controllable optical field by shaping the Pancharactnam-Berry (PB) phase under a focusing condition in Chapter 3. More precisely, the intensity distribution of the field perpendicular to the optical axis, is structured with a tunable length and subwavelength width in the focal plane.

We then propose a far-field detection system combined with a split detector to retrieve

parameters of a step structure. To demonstrate the feasibility of the method, in Chapter 4, we analyze the impact of the polarization state and focus position of the incident laser beam. Our results indicate that a dedicated polarization mode should be chosen to increase the measurement precision.

Structured light beams with optical singularities always lead to zero-field intensities and possess a high intensity gradient in a region around the singularity. The latter makes the above mentioned method interesting to enhance resolution. To improve the detection accuracy and broaden the measurement methods, we use two novel optical singularities, i.e., the optical polarization singularity and transversal optical phase singularity, as the light source to interact with the nanostructure. The physical properties of the scattered light field with the above optical singularities are analyzed in detail in Chapter 5 and Chapter 6. We demonstrate that for the case of a step structure, both the sidewall angle and height can be retrieved with high precision in a single measurement or a few measurements. Our results illustrate that optical singularities provide an effective and robust approach to determine an accurate profile of nanostructures.

SAMENVATTING

In de halfgeleiderindustrie heeft de minimale elementgrootte het nanometerniveau bereikt. Om de functionaliteit van gefabriceerde nanostructuren te behouden, is er een enorme vraag naar een techniek die niet-destructieve inspectie en in-line- of in-situ-monitoring mogelijk maakt tijdens het productieproces. Optische scatterometrie, die gebruik maakt van informatie van optische verstrooiing in het verre veld om de geometrische kenmerken van een structuur te achterhalen, is een geschikte methode. Als niet-beeldvormende techniek produceert optische scatterometrie geen beelden van het belichte object. Optische scatterometrie is afhankelijk van het verkrijgen van profielparameters van nanostructuren door continu de gegeven set van voorspelde signaturen die uit een verstrooiingsexperiment verwacht worden te vergelijken met de werkelijk gemeten signaturen. Omdat we de structuur parametriseren met een beperkte set parameters (d.w.z. we gebruiken voorkennis van de structuur), kunnen we de structuur reconstrueren met een resolutie beter dan de diffractielimiet. Deze techniek is bijzonder waardevol voor het karakteriseren van micro- en nanostructuren die vaak voorkomen in halfgeleiderapparaten en geïntegreerde schakelingen.

Coherente Fourier-scatterometrie (CFS) neemt een zeer belangrijke positie in op het gebied van scatterometrie en gebruikt een coherente bundel die door een lens wordt gefocust om de structuur te verlichten. Het verstrooide licht wordt vervolgens vastgelegd en geanalyseerd in het Fourier-vlak. CFS is gebruikt voor het detecteren van geïsoleerde defecten op oppervlakken en het bepalen van kritische dimensies zoals zijwandhoek, hoogte en breedte van geprinte structuren zoals lijnen, tralies en sleuven.

Het genereren en moduleren van optische velden is een essentieel onderwerp voor coherente bundels. Met dit als uitgangspunt hebben we de toepassingen van de CFS-techniek verder ontwikkeld en uitgebreid voor de morfologie-reconstructie van nanostructuren. In dit proefschrift ligt de primaire focus van het onderzoek op het verkennen van aspecten zoals het genereren van een gewenste lichtbundel, het effect van polarisatie en optische singulariteit als extra hulpmiddelen voor de identificatie van bepaalde parameters van nanostructuren die een uitdaging zijn gebleken bij het gebruik van uniforme lichtbundels.

In hoofdstuk 1 introduceren we de huidige ontwikkelingsstatus en metrologie-eisen van de halfgeleiderchipindustrie. Principes en karakteristieken van de bestaande methoden, waaronder elektronenmicroscopie, scanningprobemicroscopie en optische scatterometrie, worden geschetst. Bovendien worden de basistheorieën van gestructureerde optische velden, van fysische eigenschappen tot de opwekkingsaanpak, geformuleerd.

Aangezien de optische-veldmodulatie centraal staat in dit proefschrift, wordt de fundamentele theorie van de relevant methoden en de numerieke simulatiemethoden geïntroduceerd in hoofdstuk 2. Op basis hiervan genereren we een controleerbaar optisch veld door het vormen van de Pancharatnam-Berry (PB) fase onder een focusconditie in

hoofdstuk 3. De intensiteitsverdeling van het veld loodrecht op de optische as wordt gestructureerd met een instelbare lengte en sub-golflengte breedte in het brandvlak.

Vervolgens stellen we een verre-veld-detectiesysteem voor in combinatie met een gesplitste detector om de parameters van een stapstructuur te bepalen. Om de haalbaarheid van de methode aan te tonen, analyseren we in hoofdstuk 4 de invloed van de polarisatietoestand en focuspositie van de invallende laserstraal. Onze resultaten geven aan dat een speciale polarisatiemodus moet worden gekozen om de meetprecisie te verhogen.

Gestructureerde lichtbundels met optische singulariteiten leiden altijd tot veldintensiteiten van nul en bezitten een hoge intensiteitsgradiënt in een gebied rond de singulariteit. Dit laatste maakt de bovenstaande methode interessant om de resolutie te verbeteren. Om de detectienauwkeurigheid te verbeteren en de meetmethoden uit te breiden, gebruiken we twee nieuwe singulariteiten in de bundel, namelijk de optische polarisatiesingulariteit en transversale optische fasesingulariteit, als lichtbron om te interageren met de nanostructuur. De fysische eigenschappen van het verstrooide lichtveld met de bovenstaande optische singulariteiten worden in detail geanalyseerd in hoofdstukken 5 en 6. We laten zien dat in het geval van een stapstructuur zowel de zijwandhoek als de hoogte met hoge precisie kunnen worden bepaald met één of enkele metingen. Onze resultaten laten zien dat optische singulariteiten een effectieve en robuuste aanpak bieden om een nauwkeurig profiel van nanostructuren te bepalen.

1

INTRODUCTION

1.1. BACKGROUND

1

An integrated circuit (IC) is a set of electronic circuits formed on a single small flat piece (or 'chip') of semiconductor material, typically silicon. On September 12, 1958, Jack Kilby at Texas Instruments developed the world's first germanium IC, thus marking a significant milestone in the integration of electronic devices into a single semiconductor material. However, Kilby's invention did not constitute a true monolithic IC chip because it relied on external gold-wire connections. Just a few months later, Robert Noyce at Fairchild Semiconductor invented the first true monolithic IC chip, which featured critical on-chip aluminum interconnecting lines on a silicon planar substrate, and this circuit laid the foundation for modern IC chips.

Commercially-produced silicon ICs have played a pivotal role in the semiconductor industry's transition from the 'age of invention' to the 'age of business'. This transition from the small scale to today's very-large-scale integration took slightly more than half a century. The ability of IC integration to keep pace with Moore's law [1], which predicts that the number of transistors that can be integrated on a single chip doubles every 18 months, can be attributed to the continuous advancements and breakthroughs being made in semiconductor manufacturing technologies. This law still provides a reasonably accurate estimate of the scale and timing of the next generation of integrated circuits. However, the doubling period has been extended from 18 months to 24 months at present.

Technological progress, which is characterized by the production of devices with increasingly smaller geometrical parameters, has also pushed the limits of the available manufacturing equipment's capabilities. The IC manufacturing industry optimizes the processes taking into account speed, scalability and economic factors. As result, the use of the lithographic technique represents the only choice available among the nano-manufacturing techniques at present [2–5].

Shortening the operating wavelength is one of the most effective methods to improve the resolution of the lithographic method. Historically, the used wavelength decreased from the traditional ultraviolet (UV) to deep UV (DUV), and now extreme UV (EUV) has been implemented [6–8]. Together with the development of these new lithography techniques there is a need for new metrology and inspection methods. For some products, more than 50% of the manufacturing process requires a measurement or alignment process.

Surface topography control has always been an important topic in manufacturing and in many other engineering and scientific fields. In IC manufacturing, surface measurement of the in-chip regions is almost impossible because of the extremely complex patterns and the disturbances between the layers. Fortunately, analysis of suitably designed test patterns on the lithographic mask or on the wafer has been sufficient to enable evaluation and control of the IC manufacturing process [9]. The test patterns are designed as gratings with different periods and orientations that are etched into the scribe line between the in-chip regions, as shown in Figure 1.1. In the new generations of lithography process, in addition to the critical dimension (CD) of the micro/nanostructures, other parameters such as side wall angle (SWA), roundness of the corners of the gratings, line edge roughness should be determined to guarantee the quality of the end products. Furthermore, control and estimation of the SWA is particularly challenging in chip manufacturing processes.
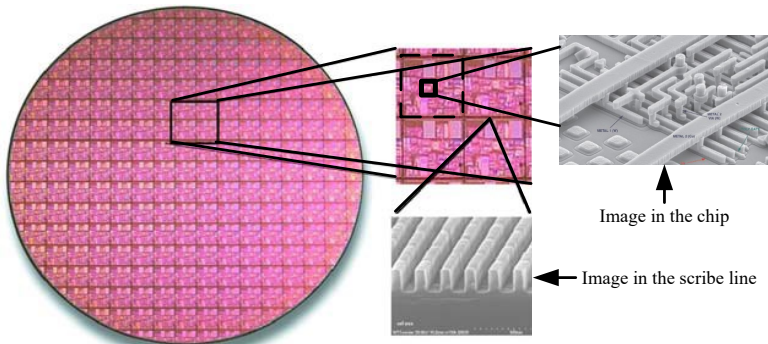
Figure 1.1: Schematic of the IC measurement. Adapted with permission from Ref. [9].

1.2. OVERVIEW OF EXISTING METROLOGY METHODS

Metrology techniques are essential to all aspects of IC research and development, integration, manufacturing process control and testing, where the use of light, electrons, X-rays, and surface forces, among others [10, 11] are applied. These technologies have a broad measurement resolution that spans several orders of magnitude. In the following subsections, the most important technologies in this field along with their advantages and disadvantages are described.

1.2.1. ELECTRON MICROSCOPY

The electron microscope uses electron beams to generate an image with nanometer-order resolution, which is far beyond the resolution of optical microscopes. The first transmission electron microscope (TEM) [12, 13] was developed in the 1930s by two German physicists, Max Knoll and Ernst Ruska, at Siemens. Adenauer improved the design of the TEM in 1937 by establishing the concept of a scanning electron microscope (SEM). In the case of SEM a focused electron beam is scanned [14], the device uses a focused electron beam that moves over the surface of a sample; this bombardment of the sample excites secondary electrons beams, which are then collected to produce a 'backscatter' pattern.

Although the TEM can provide an extremely high lateral resolution (< 50 pm) [15], this microscope is not widely used in the semiconductor field because of the complex sample preparation, limited field of view and vacuum operating environment. SEM is more suitable for surface texture imaging; however, the sample needs to be cut to enable observation of its cross-section, and the high-pressure electron beam used can easily damage the sample.

The specialized critical dimension SEM (CD-SEM) [16, 17] is optimized for the requirements of IC manufacturing for the determination of critical geometric parameters including linewidth, edge roughness, and surface defects from a normal top-down image. The SWA is obtained when the beam or the sample is tilted. Resolution and reproducibility in the sub-nanometer range can be attained by using lower electron energies [18]. Despite its strict operating environment requirements and destructiveness, the CD-SEM

1

remains one of the indispensable techniques for off-line IC measurements due to its ultra-high lateral resolution. Focused ion beams (FIBs) [19] work in a very similar manner to SEMs. FIBs also use secondary electrons excited by the sample to perform imaging, and thus offer the same advantages and disadvantages as the SEM.

1.2.2. SCANNING PROBE MICROSCOPY

In 1981, Gerd Binning and Heinrich Rohrer at IBM in Switzerland built the first scanning tunneling microscope (STM) based on their discovery of the quantum tunneling phenomenon, which refers to a tiny electron flow or a small current that occurs between the sample and the probe. When a small and delicate probe moves across the surface of a sample, STM [20, 21] uses the probe to detect this small current and use it to image the sample; this approach could overcome the shortcomings of conventional image microscopy by eliminating the input sources. With STM one can obtain images on the atomic scale [22].

Another popular scanning probe microscope is the atomic force microscope (AFM) [23], which uses the Van der Waals force acting between the atoms to measure the sample's morphology. In AFM, a probe is attached to one end of a microcantilever and a very small gap is maintained between the top of the probe and the sample surface by controlling the microcantilever; during this process, a weak Van der Waals force occurs. The sample profile information can then be obtained via undulating control of the gap between the probe tip and the surface during the scanning process to ensure that the Van der Waals force remains constant. In AFM, sub-nanometer resolution (< 1 nm lateral and < 0.1 nm vertical) is routinely realized, and true atomic resolution is achievable under appropriate conditions [24]. However, the tip itself has a certain geometric dimension; therefore, for dense structures with small dimensions, there are limitations of this technique, in particular for the case of high-aspect ratio topography measurement, particular in high aspect ratio structures where the SWAs are steeper than the slant angles of the tips.

AFMs are optimized for critical dimensions, and the 3D-AFM in particular [25, 26], is used to measure nanowires and other related dimensional parameters. The 3D-AFM has been developed to perform 3D measurements using two-axis cantilever vibration or tilting of the scanning head. In addition, the 3D-AFM can be used to extract the desired critical geometrical parameters from the 3D image, including measurement of the SWA, which is one of the parameters of interest treated in this dissertation. It has been demonstrated that the 3D-AFM sidewall measurement uncertainty can be reduced to less than 1 nm. Complex feature geometries can then be measured by using tips that are optimized for specific sample. However, the low throughput of AFM represents an obstacle to its use as an in-line inspection method.

In recent years, the advent of microscopic imaging techniques based on a near-field principle has reduced the resolution limit to less than one-tenth of the wavelength (i.e. $\lambda/10$). In scanning near-field optical microscopy (SNOM) [27, 28], the optical lens is replaced with a probe with an aperture that is much smaller than the wavelength. When such a sub-wavelength probe is placed in the near-field region, the diffraction limit is broken due to the coupling of evanescent waves that carry the subwavelength details of the object. However, SNOM suffers from the same problem as AFM since it is also a scanning technique and it is very slow. Additionally, its depth of field is much smaller

that that of the traditional microscope. All these drawbacks have greatly limited the application of SNOMs.

All methods mentioned above can provide extremely highly resolution, and play indispensable roles in the semiconductor industry. However, these methods are either too slow or destructive, and hence there is a huge demand for a fast, far-field, non-destructive measurement methods, as shown in the following section.

1.2.3. OPTICAL SCATTEROMETRY

In the early stage of IC manufacturing, the surface textures of semiconductor chips could be characterized using optical microscopes, and many microscopy-related methods have been developed to improve either the image quality or the detection precision, including differential interference/phase contrast methods [29], confocal laser scanning microscopy [30], and scanning white-light interferometry [31]. Many of these methods remain powerful in many fields today, but they cannot provide adequate resolution or precision for present semiconductor industry. The resolution of a traditional optical system is governed by the Abbe diffraction limit, which states that the smallest resolvable distance d is given by,

$$d = \frac{\lambda}{2\,\mathrm{NA}}.\tag{1.1}$$

where λ is the wavelength and $\mathrm{NA} = n\sin\theta$ is the numerical aperture of the lens with the refractive index n. The geometries of the fabricated structures are often too small to be resolved with conventional microscope systems and other measurement strategies have thus been introduced.

In the late 1990's, a commercial solution that satisfied many of the needs of high-volume IC manufacturing emerged. The technique known as optical scatterometry (OS) [32, 33]. Unlike the image-based metrology techniques, OS is not a 'what you see is what you want' method but it is a statistical model-based method. When the number of unknown parameters is rather limited and the signal to noise ratio is sufficiently large, we parametrize the structure with a priori knowledge, then we can reconstruct the structure with a resolution beyond the diffraction limit. Through measurement and analysis of the light scattered by a structure, it is possible to retrieve certain parameters of the structure. The implementation of optical scatterometry involves two main stages, as illustrated in Figure 1.2, in which the first one is known as the forward problem. The optical 'signature' or 'fingerprint' of the target structure is collected by using a suitable setup. Here, the 'signature' represents the optical response of the sample, which can be related to the structural profile and the material properties of the sample itself. Then the profile of the target structure must first be parameterized according to a priori knowledge and a forward scattering model is built to relate the profile parameters to the simulated optical signature. In the second stage, to address the inverse problem, the profile parameters are retrieved by matching the measured and simulated signatures.

As an example, for the case of a diffraction grating consisting of periodic lines and spaces, the scattered light is governed by the well-known grating equation:

$$\sin(\theta_i) + \sin(\theta_m) = m\frac{\lambda}{\Lambda},\tag{1.2}$$

where θ_i is the angle of incidence, θ_m is the angle of the m-th diffraction order (where m = 0, ±1, ±2, ...), λ is the wavelength, and Λ is the period (pitch) of the grating.

The scattered or diffracted fields are sensitive to the material and the dimensional parameters of the structure, and can thus be regarded as the 'fingerprint' or 'signature' of the grating. Therefore, similar to the use of a fingerprint to identify a person, the scattered or diffracted fields can be used to identify structures. Various scatterometric setups have been established by adjusting the angle of incidence θ_i, the scattering angle θ_m, and the wavelength of the incident light λ, which allows the setups to be basically categorized as angular scatterometer and spectroscopic scatterometer. It should be noted that the grating equation only shows the relationship in terms of the physical location between the angle of the incident light and the diffraction orders, but the interaction between the light and the grating is usually quite complex and rigorous simulations are required to calculate the field in each diffraction order.
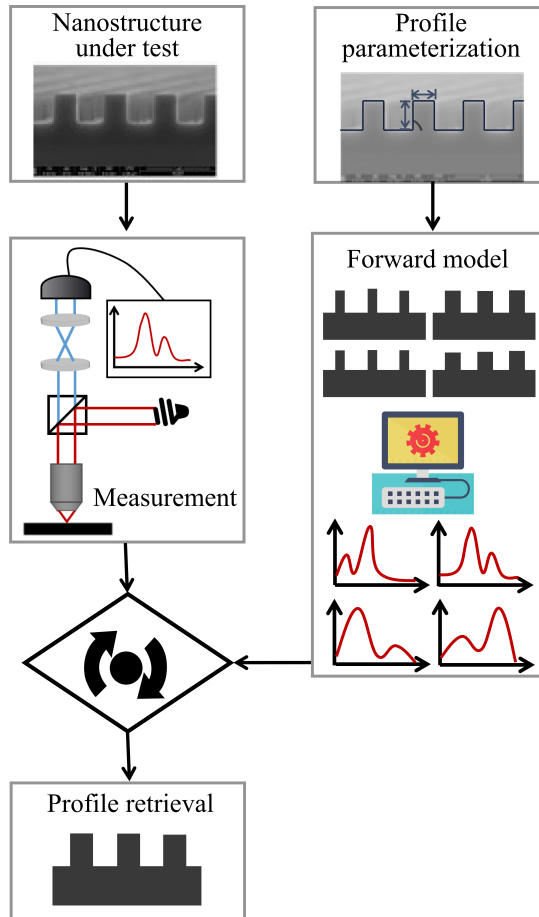

Figure 1.2: The working principle of optical scatterometry.

ANGULAR SCATTEROMETERS

The first attempt of scatterometry in metrology was undertaken by Kleinknecht and Meier in 1978 for monitoring etch rates in SiO_2 and Si_3N_4 [34]. Two years later, their setup was improved to measure the linewidths on IC masks and was used to perform in-process monitoring of these linewidths on wafers [35]. The setup was a static one in which both the incoming beam and the detector were kept at fixed angles, and it is very similar to the current 2-θ scatterometer [36]. The 2-θ scatterometer is a typical angular scatterometer, as illustrated in Figure 1.3(a). In angular scatterometry, a monochromatic light source is incident on the structure at an angle θ_i after passing through an optical system with an angle scanning function. By following Equation 1.2, the detector can locate and measure the diffracted light of any order when the angle of incidence is known.

In Figure 1.3(a), both the input module and the detector module are adjustable to a scanning angle of incidence θ_i, and the detector can move correspondingly to record the reflectance (or transmittance) of the zeroth-order diffracted light θ_0; the reflectance (transmittance) is then plotted as a function of the angle of incidence θ_i. There are two main advantages in recording the zeroth-order diffracted light. One is that the zeroth-order diffracted light generally has the highest intensity as compared to all other diffraction orders, and can thus provide the highest signal-to-noise ratio, which is an important evaluation metric. The other one is that the zeroth-order diffracted light usually exists, regardless of the values of θ_i. The zeroth-order is simply the specular order, and thus the selection of the zeroth-order becomes a study of the specular reflection as a function of the angle of incidence. In the measurements of the specular reflection, the detector is always positioned symmetrically at the normal to the substrate with respect to the incoming light, and this is why the detector is also named the 2-θ scatterometer.

Figure 1.3(b) shows another type of angular scatterometer. Here, the angle of incidence θ_i is fixed at a specific angle, whereas the detector is scanned or an array detector is used to record the diffracted light of the various diffraction orders θ_m. The reflectance (or transmittance) is then plotted as a function of the diffraction angle θ_m. To distinguish it from the aforementioned 2-θ scatterometer, this setup can be called a scattering angle-resolved scatterometer based on its working characteristics; similarly, the 2-θ scatterometer can also be named as incident angle-resolved scatterometer. For a specific ratio of λ/Λ, Equation 1.2 shows that a higher order may not propagate to the far field. To ensure that sufficient scattering information is available to enable accurate profile reconstruction of small-pitch structures, light sources with short illumination wavelengths, e.g. an EUV light source [37] or an X-ray light source [38], can be used in scattering angle-resolved scatterometers.

SPECTROSCOPIC SCATTEROMETERS

Rather than scanning the input/detector angles as the angular scatterometers do, spectroscopic scatterometers instead scan the wavelength of the incoming light. As depicted in Figure 1.3(c), the spectroscopic scatterometer is implemented by using a broadband light source and detects the spectrum of the scattered light on the detector side. According to Equation 1.2, the incident wavelength will also influence the diffraction angle. Except the zeroth-order reflection, the grating will disperse each wavelength into a different diffraction direction when illuminated by a broadband source. Therefore, similar to the 2-θ

scatterometer, the majority of spectroscopic scatterometers only collect the zeroth-order reflection to avoid the cumbersomeness of the first (or higher) orders of the diffraction. The collected intensities of the reflected light can be used to determine parameters of the structure, as can the phase and polarization information. For example, the ellipsometric scatterometer is a well-known type of spectroscopic scatterometers, in which the polarization changes in the scattered light are used to determine the parameters of the structure being illuminated. This technique has been widely used in the measurement of the critical dimensions of grating structures [39, 40].
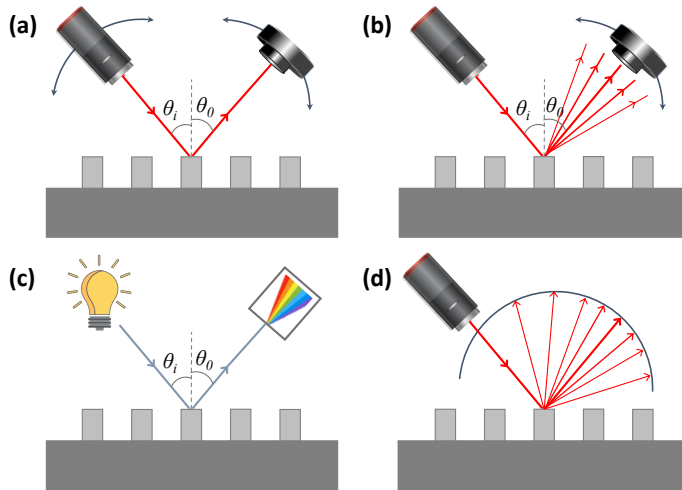
Figure 1.3: Schematics of different scatterometric setups. (a) a 2-θ system in which the incoming light and the detector are moved simultaneously, and (b) a fixed angle setup in which only the detector moves; (c) spectroscopic system without any moving parts. The amplitude, phase and polarization of the light can be used to acquire information about the structure to be analyzed. (d) a hemisphere detector, e.g., a Fourier lens system, which can collect all diffraction orders simultaneously.

By using special optics, multiple diffraction orders can be measured simultaneously, as illustrated in Figure 1.3(d). Optical Fourier scatterometry is a typical example. In an optical Fourier scatterometer, a high-NA objective is employed to focus the beam into the structure and measure the reflectance for different diffraction angles simultaneously in the Fourier plane; the information in the Fourier space is then analyzed to increase the detection capability.

1.3. COHERENT FOURIER SCATTEROMETRY

Coherent Fourier scatterometry (CFS) is a relatively new branch of OS that was originally suggested by El Gawhary et al. [41]. Unlike the scatterometry methods mentioned previously, in which the light source is often a discharge lamp or is quasi-monochromatic,

CFS uses the scattering behavior of a spatially coherent light source. When a discharge lamp or a quasi-monochromatic spatially incoherent light source is used as the incident light, a diffraction-limited spot cannot be generated. This implies that a large spot illuminates a large area of the grating. When compared with the incoherent case, the use of spatially coherent illumination makes CFS a competitive and possibly even superior method when an appropriate strategy is used. In addition to the widespread use for periodic structures, CFS can also be used to study isolated structures. To date, CFS has been applied to the reconstruction of grating profiles and the detection of nanoparticles or defects on substrates made from different materials [42]. In this thesis, one of the main topics is the application of CFS for the reconstruction of the steep SWA of a silicon-based step nanostructure, which represents as a quite challenging problem in IC manufacture.
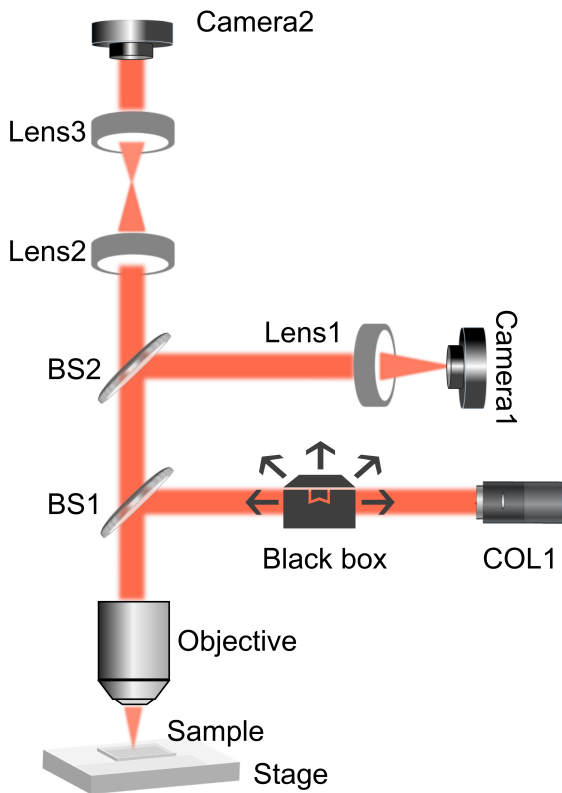
Figure 1.4: Common configuration used for the CFS technique.

A common configuration for CFS is shown in Figure 1.4. The incident beam usually stems from a spatially coherent light source with a specific wavelength; in our case, the selected wavelength is 633 nm, which can be generated by a He-Ne laser. After passing through a specific optical system (indicated by the black box in the incident arm), a light probe with the desired light structure is focused on the sample by using an objective with a specific NA. If a strongly focused coherent illumination is applied, the probe

beam will be sub-micron in size; therefore, to cover the area of interest on the sample, a scanning system such as the typical system based on use of piezoelectric stages can be implemented. The transverse scanning capability of a piezoelectric stage ensures that the sample can be scanned point-by-point in the plane, which is essential for CFS. The same objective is also used to collect the reflected and scattered light, where the far field is imaged on a charge-coupled device (CCD) camera (i.e., camera 2 in Figure 1.4). Additionally, another branch can be implemented to allow imaging of the sample plane on another CCD camera (i.e., camera 1 in Figure 1.4).

The coherence of the illumination provides more degrees of freedom (DoFs) for optical detection. More precisely, this technique not only enables the intensity or phase to be measured, but also enables the measurement of the singularity, the orbital angular momentum, the spin angular momentum, and other optical properties of the light beam. The specific distribution of these optical properties construct a huge family of structured light fields, which has fulfilled many applications. Structured light technology is characterized by its accuracy, so merging structured light field and CFS can be used to improve the sensitivity on the determination of the structural parameters. Hereto, the most concise description of our workflow becomes projecting a known pattern of structured light onto the objects and analyzing the deformations or distortions of the pattern after it has interacted with the objects. By carefully analyzing these distortions, the shape of the objects within the field of view can be reconstructed.

1.4. STRUCTURED LIGHT FIELD

Structured light refers to the generation and application of custom light fields. They can be customized by several optical DoFs, including its wavelength (coherence), amplitude, phase and polarization. Structured light has been proved to be a very useful tool in many fields related to light–matter interactions, from imaging [43], microscopy [44], metrology [45] to optical communication [46], optical tweezers [47], quantum information [48], just to name a few. In the semiconductor industry, structured light may open up new ways to address the challenges in measurement precision.

Many types of structured light have been widely generated and researched. A milestone of structured light are light beams carrying orbital angular momentum (OAM), such as optical vortex with spatial helical phase. Intensive studies of OAM have opened the floodgates of structured light research [49]. Another important branch of structured light is that of the 'Poincaré beams', which are light beams that can have all possible polarization states in their cross-section [50]. The investigation of this kind of 'exotic' beam thrived after it was found that radially and azimuthally polarized beams exhibit very intriguing properties upon tight focusing [51].

In the early 2000s, with the emergence of liquid-crystal spatial light modulators (LC-SLM) [52], digital micromirror devices (DMD) [53] and later geometric phase elements such as q-plates [54] and other spin–orbit approaches [55], it has become possible to reshape the light in all its DoFs outside a laser cavity. To date, many types of spatially structured fields have been widely generated and researched, a glimpse of a manifold of structured beams along with their physical properties is shown in Figure 1.5, including fundamental Gaussian beams as well as higher order Gaussian beams and their superpo-

1

sition beams, propagation-invariant beams and Airy beams. Essentially, these structured beams can be described as the eigenfunctions of linear and angular momentum operators, or as the combinations of these eigenfunctions.
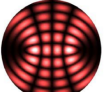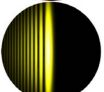
Beam family (eigenfunctions)	Beam profile	Operator	Eigenvalue (if relevant)
Gaussian beams (waist width w_0)		Beam quality factor $\widehat{\mathcal{M}}^2 = \frac{r^2}{w_0^2} + \frac{k^2 w_0^2}{4}\hat{p}^2$	Mode order $N+1$
Propagation-invariant beams		Transverse Laplacian (free-space Hamiltonian) $\hat{p}^2$	k_r^2
HG beams HG_{mn}		Quality factor difference $\widehat{M} = \frac{x^2-y^2}{w_0^2} + \frac{k^2 w_0^2}{4}(\hat{p}_x^2 - \hat{p}_y^2)$	$m-n$
$\left\{ \begin{array}{c} \text{LG beams } \mathrm{LG}_{\pm\ell p} \\ \text{Bessel beams } J_\ell(k_r r)\mathrm{e}^{\mathrm{i}\ell\phi} \\ \text{(propagation invariant)} \end{array} \right\}$		Angular momentum $\widehat{L} = x\hat{p}_y - y\hat{p}_x$	Angular momentum label $\pm\ell$
GHLG beams (label with m,n or $\pm\ell, p$)		Operator superposition $\alpha\widehat{L} + \beta\widehat{M}$	Same eigenvalue $m-n = \pm\ell$
IG beam		Operator superposition $\alpha\widehat{L}^2 + \beta\widehat{M}$	–
Mathieu beam (propagation invariant analogue of IG)		Operator superposition $\alpha\widehat{L}^2 + \beta(\hat{p}_x^2 - \hat{p}_y^2)$	–
Airy beam		Quantum Hamiltonian with linear potential $\hat{p}^2 + \alpha x$	–

Figure 1.5: Typical examples of structured light beams with an operator representation. Adapted with permission from Ref. [56].

Optical singularity is a common phenomenon that can be observed in both Hermite-Gaussian beams and Laguerre-Gaussian beams. An optical singularity occurs at a point (x_0, y_0) where a certain optical property ϕ of the field (such as phase or polarization) is discontinuous, i.e. the limit

$$\lim_{(x,y)\to(x_0,y_0)} \phi(x,y) \tag{1.3}$$

does not exist. This implies that the amplitude at (x_0, y_0) must be 0 and the field gradient in the immediate neighbourhood of the singularity is high. There are two main forms of optical singularities, namely the polarization and phase versions. The just mentioned beam optical vortice is one typical type of phase singularity and is part of the larger subject of singularity optics. Poincaré beams have a polarization singularity on their

1

optical axis. In the following, in accordance with the work for the thesis, I will introduce the basic properties of structured beams with specific phase and polarization singularity distributions.

1.4.1. PHASE SINGULARITY

TYPICAL LASER MODE

When studying Gaussian beams, polarization-dependent effects will be neglected, so we will use the scalar theory. Let E be a component of the electric field of a Gaussian beam and $u(x, y, z)$ or $u(r, \phi, z)$ be the reduced amplitude, then the electric field $E(x, y, z)$ can be written as:

$$E(x, y, z) = u(x, y, z)e^{ikz},\tag{1.4}$$

where $k = 2\pi/\lambda$ is the wavenumber. Under the paraxial approximation, the field $u(x, y, z)$ or $u(r, \phi, z)$ obeys the free-space paraxial Helmholtz equation [57] as

$$\nabla^2 u + 2ik\frac{\partial u}{\partial z} = 0,\tag{1.5}$$

where ∇^2 represents the Laplacian operator in the transverse coordinates. The equation can be gained from the regular Helmholtz equation $(\nabla^2 + k^2)u = 0$ by substituting Equation 1.4 and neglecting the term $\frac{\partial^2 u}{\partial z^2}$. We will consider solutions of the form

$$u(x, y, z) = \mathscr{A}(z)\exp\left[\frac{ik(x^2 + y^2)}{2q(z)}\right].\tag{1.6}$$

Here, $\mathscr{A}(z)$ is a complex-valued function and $q(z)$ is called the complex beam parameter for a Gaussian beam. If the imaginary part of $q(z)$ is negative, Equation 1.6 will have a Gaussian intensity profile perpendicular to the z-direction. The Gaussian beam whose amplitude is a purely exponential function of $x^2 + y^2$ is the well-known fundamental Gaussian mode. There also exists higher-order Gaussian modes for which $\mathscr{A}$ depends on x and y polynomially.

For the fundamental Gaussian mode, substitution of Equation 1.6 in Equation 1.5 gives

$$q(z) = z + q_0,\tag{1.7}$$

for some constant q_0. And

$$\mathscr{A}(z) = \frac{q_0}{q(z)},\tag{1.8}$$

where the integration has been chosen such that $\mathscr{A}(0) = 1$. With Equation 1.7 and 1.8, the Equation 1.6 can be written as:

$$u(x, y, z) = \frac{q_0}{q(z)}\exp\left[\frac{ik(x^2 + y^2)}{2q(z)}\right].\tag{1.9}$$

To interpret this result, we write $1/q(z)$ as the sum of real and imaginary parts with beam curvature $R(z)$ and beam waist $w(z)$ as:

$$\frac{1}{q(z)} = \frac{1}{R(z)} + \frac{i\lambda}{\pi w^2(z)}.\tag{1.10}$$

In Equation 1.10:

$$R(z) = z\left[1 + \left(\frac{z_R}{z}\right)^2\right],$$
$$w^2(z) = w_0^2\left[1 + \left(\frac{z}{z_R}\right)^2\right], \tag{1.11}$$

where w_0 is the beam waist when $z = 0$ and $z_R = \pi w_0^2/\lambda$ is the Rayleigh distance. Furthermore, we have

$$\frac{q_0}{q(z)} = \frac{w_o}{w(z)}\exp\left[-i\arctan(z/z_R)\right]. \tag{1.12}$$

With the help of Equation 1.10 and 1.12, Equation 1.9 can also be further represented in terms of $R(z)$ and $w(z)$:

$$u(x, y, z) = \frac{w_0}{w(z)}\exp\left\{-i\arctan(z/z_R) + \frac{ik(x^2 + y^2)}{2R(z)} - \frac{x^2 + y^2}{w(z)^2}\right\}. \tag{1.13}$$

There also exist higher-order modes whose variation in the plane perpendicular to z-axis is more general and complex. The so-called Hermite-Gaussian (HG) is the paraxial solution in Cartesian coordinates. The Hermite-Gaussian solution HG_{mn} modes, which are obtained by the separating the variables x and y, can be written as:

$$\begin{aligned}
u_{mn}(x, y, z) =& \mathcal{A}_{mn}(q(z))H_m\left(\frac{\sqrt{2}x}{w(z)}\right)H_n\left(\frac{\sqrt{2}y}{w(z)}\right)\exp\left\{\frac{ik(x^2 + y^2)}{2q(z)}\right\} \\
=& H_m\left(\frac{\sqrt{2}x}{w(z)}\right)H_n\left(\frac{\sqrt{2}y}{w(z)}\right)\frac{w_0}{w(z)}\exp\left\{-i(m + n + 1)\arctan(z/z_R)\right\} \\
& \exp\left\{\frac{ik(x^2 + y^2)}{2R(z)} - \frac{x^2 + y^2}{w(z)^2}\right\},
\end{aligned} \tag{1.14}$$

where the amplitude factors H_n denotes the the Hermite polynomials given by:

$$H_n(x) = (-1)^n\exp(x^2)\frac{d^n}{dx^n}\exp(-x^2).$$

Note that the fundamental Gaussian beam can be generated when $m = n = 0$. Every light field that is a solution of the paraxial wave equation can be written as a linear combination of the HG modes. The intensity distribution of the HG modes varies with different values of the parameters m and n, as shown in Figure 1.6.

Another complete basis is the so-called Laguerre-Gaussian (LG) modes, which is the paraxial solution in cylindrical coordinates (r, ϕ, z). The Laguerre-Gaussian solution LG_p^l modes can also be obtained by separating the variables r and ϕ [58]:

$$\begin{aligned}
u_{lp}(r, \phi, z) =& \mathcal{A}_{lp}(q(z))\left(\frac{\sqrt{2}r}{w(z)}\right)^{|l|}L_p^{|l|}\left(\frac{2r^2}{w(z)^2}\right)\exp\left[\frac{ikr^2}{2q(z)}\right]\exp\{il\phi\} \\
=& \left(\frac{\sqrt{2}r}{w(z)}\right)^{|l|}L_p^{|l|}\left(\frac{2r^2}{w(z)^2}\right)\frac{w_0}{w(z)}\exp\{-i(2p + |l| + 1)\arctan(z/z_R)\} \\
& \exp\left\{\frac{ikr^2}{2R(z)} - \frac{r^2}{w(z)^2}\right\}\exp\{il\phi\},
\end{aligned} \tag{1.15}$$
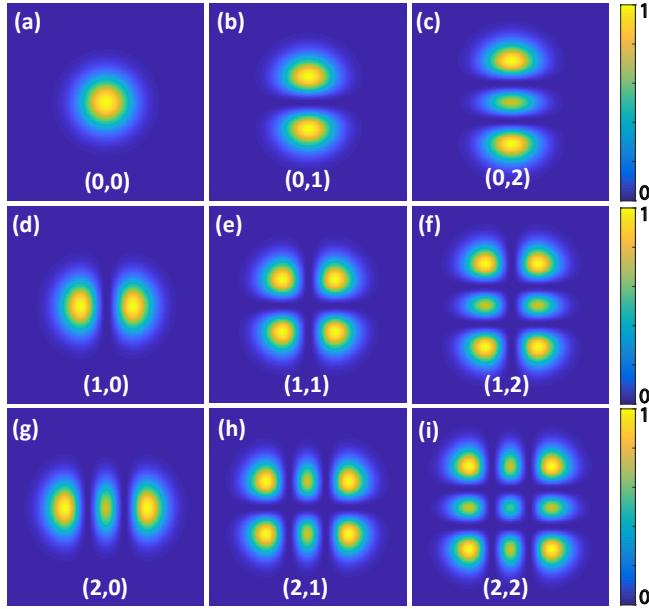
Figure 1.6: Intensity distribution of HG_{mn} mode with different m and n parameters.
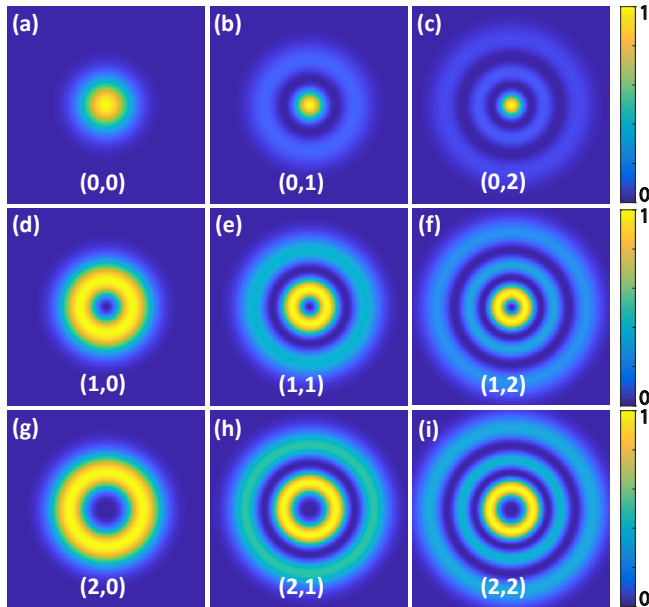
Figure 1.7: Intensity distribution of LG_p^l modes with different p and l parameters.

where the amplitude factor $L_p^l(x)$ is given by the Laguerre polynomial:

$$L_p^l(x) = \frac{\exp(x)x^{-l}}{p!} \frac{d^p}{dx^p}\left(x^{l+p}\exp(-x)\right),$$

the parameter l represents the azimuthal index, which characterizes the order of the phase singularities or vortices. After completion of a full revolution around the central optical singularity, the phase is changed by $2\pi l$. In addition, the parameter p represents the radial index, which determines the number of concentric circles or rings within the intensity distribution of the light spot. Figure 1.7 illustrates the intensity distributions of LG modes with various values of l and p. The simplest and most distinctive LG mode ($LG_{1,0}$) appears as a single annular ring of high intensity with a 2π phase singularity along the beam axis. When $l = p = 0$, this solution reduces to the well-known fundamental Gaussian beam solution as Equation 1.13.
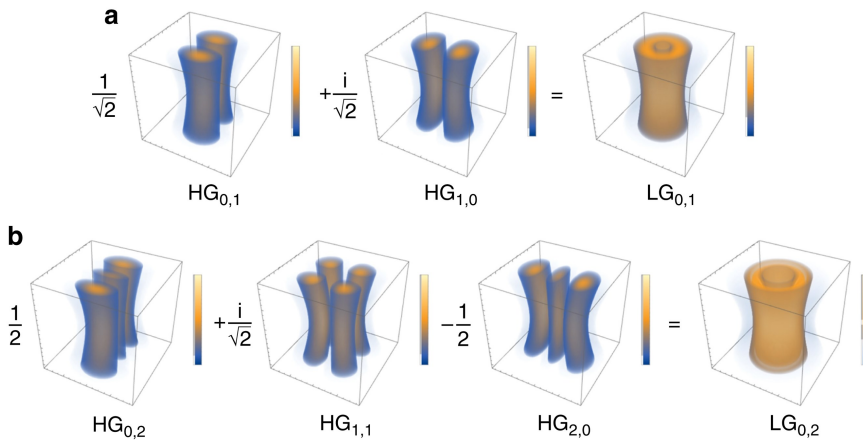
Figure 1.8: Decomposition of LG vortex beams. Examples of the decomposition of LG modes.(a) $LG_{0,1}$ and (b) $LG_{0,2}$ into HG modes. Adapted with permission from Ref. [49].

The above solutions, both the HG modes and the LG modes are the paraxial solutions to the scalar Helmholtz equation that corresponds to homogeneously polarized scalar beams. Every above beam family is known to be a basis for the two-dimensional space, and thus an arbitrary square integrable two-dimensional function can be presented as a series of HG or LG functions. In fact, these two beam families are equivalent, such that any LG_p^l mode can be decomposed into a linear combination of HG_{mn} modes and vice versa, as illustrated in Figure 1.8.

PROPERTIES OF OPTICAL VORTICES

In optical vortex (OV) beams, light is twisted like a corkscrew around its axis of travel. The phase circulates around a zero-field point, thus generating a helical phase front to form a phase singularity in the center. Over the last 30 years, the OV beam has been regarded as

1

one of the most interesting optical modes. In the following, I will briefly introduce the basics of singularities, their properties, their generation, and related applications.

The OV beam has the topological charge (TC) of its helical phase, which depends on how many twists the light does in one wavelength. If the phase angle continually increases along a closed loop and changes by $2\pi l$, then l is the so-called TC, which can be positive or negative, depending on the direction of the twist. In general, the TC is an integer to ensure that the field is uniquely defined and it is defined as:

$$l = \frac{1}{2\pi} \oint_c \nabla\varphi(\mathbf{r}) \cdot d\mathbf{r}, \tag{1.16}$$

where φ is the phase distribution and c is a closed loop that surrounds the singularity.
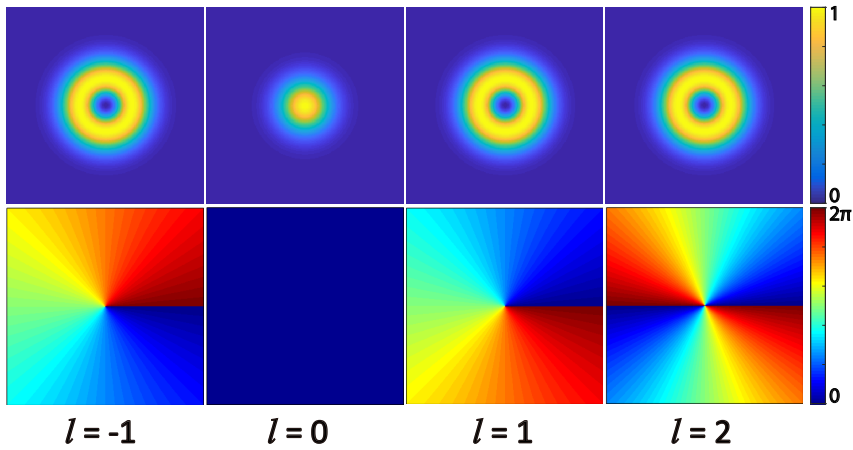
Figure 1.9: The intensity of optical vortex beams with different topological charges and their corresponding phase distribution. The value of l indicates the topological charges of OV beams.

The LG beam is one of the natural laser modes that contains an OV and the mathematical expression for this beam has been given as Equation 1.15. Figure 1.9 depicts the typical geometries of the OV beams. The value l of TC can effect the size of the region of the singularity and also can decide the transverse phase structure. The light beam with helical phase-fronts also carry an orbital angular momentum (OAM) equivalent to $l\hbar$. According to the classification introduced by Nye and Berry [59], a monochromatic light wave can possess two main types of phase singularities: a screw wavefront dislocation and an edge dislocation. Physically, these singularities can be divided into longitudinal and transversal states, i.e., oriented parallel and perpendicular to the propagation direction, respectively. Figure 1.10 shows the schematics of the longitudinal and transversal optical singularities with an OAM. An intuitive difference appears between them, in that the OAM vector is rotated by $\pi/2$ to that of the other singularity. Consequently, a pure screw dislocation is the core of a 'longitudinal' OV, and the edge dislocation produces a 'transversal' OV, with respect to the wave propagation direction.

The transversal optical singularity has been demonstrated to be closely associated with the energy flux, which is usually accompanied by a locally reversed energy flux. The most direct way to produce a singularity is to form an edge dislocation. In 2000, Vasnetsov et al. analyzed the way in which an edge dislocation of a wavefront can be created within an interference field of two paraxial Gaussian beams with different waist parameters [60]. In this case, the phase saddle and the vortex often appear simultaneously. The position of phase saddle point and vortex point in the interference field is related to the off-axis parameters, the waist width, and the phase and relative amplitude of the beams [61]. At a specified value of the governing parameter, the saddle point coincides with the vortex. There is also a case in which the saddle collides with the vortex, which results in the reversal of the sign of the light circulation and the creation of two new circular edge dislocations.

A simpler case is that when an optical field is tightly focused, e.g., in typical dark-hollow Gaussian beams, where transversal vortices and transverse components will appear directly in the focal field [62]. The distributions of the phase singularities are highly dependent on the truncation parameter and the NA of the focusing lens. In particular, the beam order (i.e., the intensity distribution in the cross-section) additionally affects the spatial distributions of the phase singularities, and these phase singularities can then be achieved outside the focal plane.
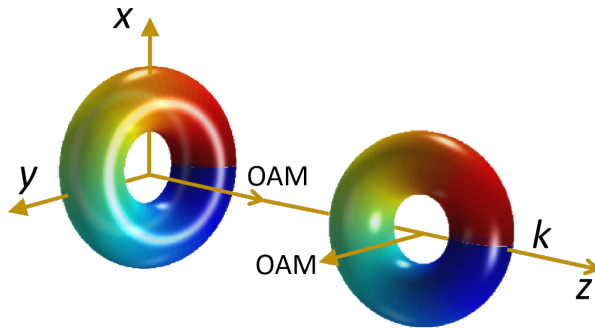
Figure 1.10: Characteristics of longitudinal and transversal optical singularities with a spatial OAM.

In a more general case, when three or more plane waves interfere in space, complete destructive interference occurs on lines called nodal lines, where there occur phase singularities, wave dislocations or optical vortices, as shown in Figure 1.11. The singular nature of the nodes arises in the case where the complex number describing the wave is zero [63]. Provided that an interference pattern is formed by superposing three plane waves, where the sum of the two smallest phasors exceeds the amplitude of the largest, the vortex lines will be both straight and parallel. Therefore, in a cross-section, there is a regular array of vortex points in two dimensions [64]. Here, the distribution of the vortices is highly dependent on the directions and amplitudes of the waves. For situations with four or more instances of laser interference, the properties of the singularities are similar.
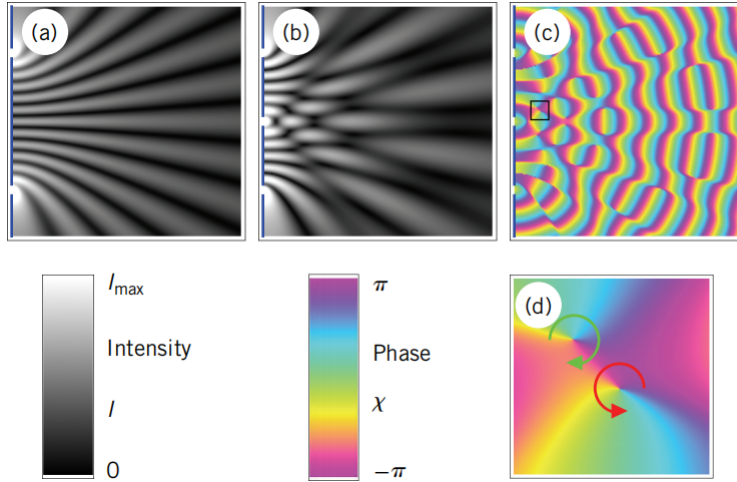
Figure 1.11: Near field for Young's slits. (a) Intensity for two slits, showing bright and dark fringes. (b) Intensity for three slits, where now zeros of intensity occur at points. (c) Phase for three slits, where intensity zeros occur where all phases meet. (d) Inset, showing two phase singularities, whose phases increase in opposite directions. Adapted with permission from Ref.[64].

1.4.2. POLARIZATION SINGULARITY

REPRESENTATION OF POLARIZATION STATE

As we all know, light can occur as a plane wave, which is characterized by a wave vector, an electric vector and a magnetic vector, and these three vectors are perpendicular to each other. Generally, the amplitudes and the phase difference of the two orthogonal components of the electric field vector are used to represent the polarization state of the light. In free space, the plane wave which propagates along the z-direction and its electric displacement vector lies in the xy-plane can be described as follows:

$$
\begin{aligned}
E_x(z, t) &= a_1(z)\cos(\omega t - kz + \delta_1), \\
E_y(z, t) &= a_2(z)\cos(\omega t - kz + \delta_2), \\
E_z &= 0.
\end{aligned}
\tag{1.17}
$$

where $a_n(z)(n = 1, 2)$ is the amplitude of the wave, ω is the angular frequency, k is the wave number, and δ_n $(n = 1, 2)$ is the corresponding initial phase. Further transformation then gives:

$$
\left(\frac{E_x}{a_1}\right)^2 + \left(\frac{E_y}{a_2}\right)^2 - 2\frac{E_x}{a_1}\frac{E_y}{a_2}\cos\delta = \sin^2\delta,
\tag{1.18}
$$

where $\delta = \delta_2 - \delta_1$ denotes the phase shift between the x and y components. Equation 1.18 implies that the electric field vector describes an ellipse as a function of time at a fixed position z, and the polarization characteristics of this elliptically polarized light can be uniquely determined as long as a specific set of parameters (a_1, a_2, δ) is provided.

Generally, the two axes of the ellipse are not in the Ox and Oy directions in the Cartesian coordinate system. Let $O\xi$ and $O\eta$ be a set of new coordinate axes oriented along the major and minor axes of the ellipse, respectively, and let φ be the angle between Ox and the major axis of the ellipse $O\xi$, as shown in Figure 1.12. If $2a$ and $2b$ ($a \geq b \geq 0$) are the axis lengths of the ellipse and $A = \sqrt{a^2 + b^2}$, then the ellipse equations in the $O\xi$, $O\eta$ coordinate system are

$$
\begin{aligned}
E_\xi(z, t) &= A\cos\chi\cos(\omega t - kz), \\
E_\eta(z, t) &= \pm A\sin\chi\sin(\omega t - kz).
\end{aligned}
\tag{1.19}
$$

The positive and negative signs before A represent the two possible directions that the endpoints of the electric vector can follow along the ellipse as time t increases. The polarization state of the same polarization ellipse can also be uniquely described by this set characteristic parameters (A, φ, χ), where φ denotes the orientation of the major axis of the ellipse, and χ is used to calculate the ellipticity $\tau = \tan\chi = \mp b/a$. When $\tau = 0$, indicates that E is linearly polarized, $\tau = \mp 1$ represents left- and right-handed circular polarised light, respectively, $0 < \tau < 1$ represents the left-handed elliptical polarization state, and $-1 < \tau < 0$ represents the right-handed elliptical polarization state.
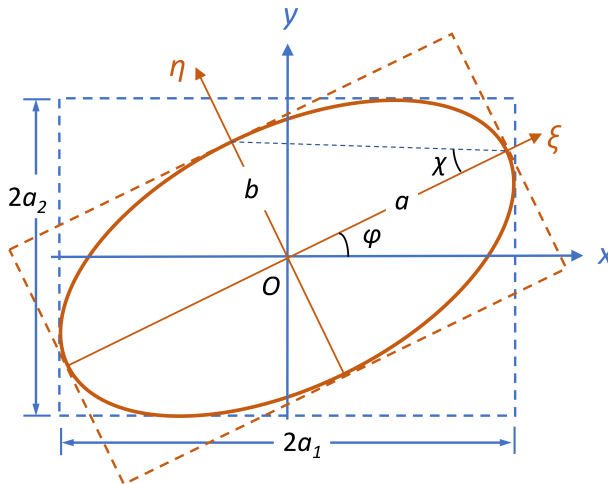
Figure 1.12: The polarization ellipse.

Characterization of the polarization ellipse requires three independent quantities, namely the amplitudes a_1, a_2 and the phase difference δ, or the total amplitude A, the angle χ representing the ellipticity and the orientation of the major axis φ. These two sets of characteristic parameters, (a_1, a_2, δ) and (A, φ, χ), can be mutually converted. However, the period of the light field is too short to allow direct observation of the polarization ellipse and therefore a more intuitive description of the polarization state is required. In 1852, George Gabriel Stokes proposed that the polarization state of a light field can be

expressed using four quantities, namely the Stokes parameters.

$$s_0 = a_1^2 + a_2^2, \tag{1.20a}$$

$$s_1 = a_1^2 - a_2^2, \tag{1.20b}$$

$$s_2 = 2a_1 a_2 \cos\delta, \tag{1.20c}$$

$$s_3 = 2a_1 a_2 \sin\delta. \tag{1.20d}$$

The parameter s_0 is proportional to the wave intensity, and the parameters s_1, s_2, and s_3 have the following relationships with φ ($-\pi/2 \le \varphi \le \pi/2$) and χ ($-\pi/4 \le \alpha \le \pi/4$)

$$s_1 = s_0 \cos 2\chi \cos 2\varphi, \tag{1.21a}$$

$$s_2 = s_0 \cos 2\chi \sin 2\varphi, \tag{1.21b}$$

$$s_3 = s_0 \sin 2\chi. \tag{1.21c}$$

A polarized beam such as Equation.1.18 satisfies:

$$s_0^2 = s_1^2 + s_2^2 + s_3^2. \tag{1.22}$$

whereas a partially polarized beam satisfies:

$$s_0^2 > s_1^2 + s_2^2 + s_3^2. \tag{1.23}$$

To describe all the possible states of polarization (SoP) of a polarized plane-wave, the Poincaré sphere (PS) provides a prominent geometric representation, where the SoP is represented by a point on the surface [65].The PS is constructed based on the coordinates $\mathbf{s}_n = s_n/s_0, (n = 1, 2, 3)$, and 2θ and 2φ denote the longitude and latitude of the point in the spherical coordinate system respectively, as shown in Figure 1.13. The north and south poles correspond to right- and left-handed circular polarization, the equator to linear polarization, and intermediate points between the poles and equators to elliptical polarization. The northern and southern hemispheres separate right- and left-handed ellipticity. For arbitrary meridian circles, the orientations of the SoPs produce no change although changes in ellipticity from the south to the north poles, where positive and negative values represent left-handed and right-handed SoPs, respectively. Similarly, for arbitrary latitude circles, the ellipticity of the SoPs produce no change with the orientations changes.

Finally, the state of polarization of a fully polarized monochromatic beam can be expressed as a two-dimensional Jones vector with respect to an orthonormal basis $(\hat{\mathbf{e}}_1, \hat{\mathbf{e}}_2)$ in the form

$$\boldsymbol{E} = \cos\chi\, \hat{\mathbf{e}}_1 + \sin\chi \exp\left(i\varphi\right) \hat{\mathbf{e}}_2. \tag{1.24}$$

The angle χ is a measure to control the relative amplitudes of the two components of $\boldsymbol{E}$, and the angle φ is related to their phase difference. Currently, the two most common used orthonormal basis are the Cartesian representation $(\hat{\mathbf{e}}_x, \hat{\mathbf{e}}_y)$ and the helicity representation $(\hat{\mathbf{e}}_r, \hat{\mathbf{e}}_l)$, during which $\hat{\mathbf{e}}_x$ and $\hat{\mathbf{e}}_y$ denote unit linear polarized state along x and y direction, and $\hat{\mathbf{e}}_r$ and $\hat{\mathbf{e}}_l$ denote right-hand and left-hand circularly polarized state.
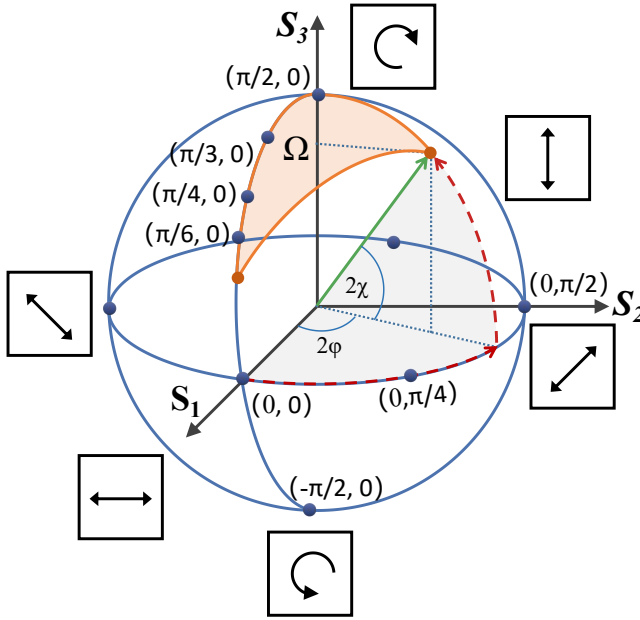
Figure 1.13: Standard Poincaré sphere representation for plane waves with arbitrary ellipticity, orientation and handedness.

PROPERTIES OF CYLINDRICAL VECTOR BEAMS

Polarization is another fundamental property of light, which has been used to initiate different types of light-induced process by varying the incident polarization states. From a physical perspective, a polarized beam features a spatially independent or dependent distribution and its polarization distribution can be either homogeneous or inhomogeneous. The latter is a typical type of structured beams. Polarization singularities appear widely in polarized structured beams, which has been demonstrated to show extreme sensitivity when detecting slight changes due to interaction with (nanoscale) objects. One particular example is that of laser beams with cylindrical symmetry in their polarization, known as cylindrical vector beams (CVBs), which can be described in terms of higher order or hybrid order Poincaré spheres [66, 67].

Polarization singularities can be classified into two categories. For a circular polarization where the polarization ellipse's orientation is undefined, it is defined as the C-point. The other kind is the V-point, which generally appears in local linearly polarized optical fields, and both the orientation and the handedness of the polarization ellipse can be considered to be indeterminate. In random fields, elliptical and linear polarization states can occur in different regions in the same field.

The CVBs are vector beam solutions to Maxwell's equations that obey axial symmetry in terms of both amplitude and phase. Consider the full vector wave equation with the electric field

$$\nabla \times \nabla \times \boldsymbol{E} - k^2 \boldsymbol{E} = 0. \tag{1.25}$$

An axially symmetric vector solution with the electric field aligned to the azimuthal direction can be written as:

$$\boldsymbol{E}(r,z) = U(r,z) \exp\left[i(kz - \omega t)\right]\mathbf{e}_\phi, \tag{1.26}$$

where $\mathbf{e}_\phi$ is the unit vector in the azimuthal direction and $U(r,z)$ should satisfy the following equation under the paraxial approximation:

$$\frac{1}{r}\left(r\frac{\partial U}{\partial r}\right) - \frac{U}{r^2} + 2ik\frac{\partial U}{\partial z} = 0. \tag{1.27}$$

There is a clear difference for Equation 1.5 and Equation 1.27. The solution that obey azimuthal polarization symmetry has the trial solution as [68]

$$U(r,z) = E_0 J_1\left(\frac{\beta\gamma}{1 + iz/z_R}\right)\exp\left[-\frac{i\beta^2 z/(2k)}{1 + iz/z_R}\right]u(r,z), \tag{1.28}$$

where β is a constant scale parameter, $J_1(x)$ is the first-order Bessel function of the first kind and $u(r,z)$ is the fundamental Gaussian solution in cylindrical coordinates. This solution corresponds to an azimuthally polarized vector Bessel-Gaussian beam solution. In many applications, the simplified distribution is widely used. For a small value of β, the vector Bessel–Gaussian beam at the beam waist can be approximated as:

$$\boldsymbol{E}(r,z) = Ar\exp\left(-\frac{r^2}{w(z)^2}\right)\mathbf{e}_i, i = r, \phi. \tag{1.29}$$

The amplitude profile is exactly that of the LG_{01} mode without the vortex phase $\exp(i\phi)$. In the same way as for the scalar situation, with reference to Equations. 1.14 and 1.15, the radial $\boldsymbol{E}_r$ and azimuthal $\boldsymbol{E}_\phi$ polarizations denote can also be expressed as a superposition of the orthogonally polarized HG_{01} and HG_{10} modes [69]

$$\begin{aligned}\boldsymbol{E}_r &= HG_{10}\hat{e}_x + HG_{01}\hat{e}_y, \\ \boldsymbol{E}_\phi &= HG_{01}\hat{e}_x + HG_{10}\hat{e}_y.\end{aligned} \tag{1.30}$$

The state of polarization of the modes shown in Figure 1.14 (a)-(c) are the radial polarized, azimuthal polarized and the linear superposition of these two. Figure 1.14 (d) and (e) illustrates the formation of the radial and azimuthal polarization beams by using the linear superposition of orthogonally polarized HG modes, as demonstrated in Equation 1.30.

1.4.3. PANCHARATNAM-BERRY PHASE

Pancharatnam–Berry (PB) phase, also known as geometric phase, is distinct from the dynamic phase that we are familiar with. Dynamic phase refers to the phase changes that result from changes in optical path length as a light wave propagates through a material. This phase is associated with the changes in both the optical path length and the refractive indices properties of the material. In contrast, the PB phase refers to the accumulation of an additional phase caused by a change in the polarization state that occurs when
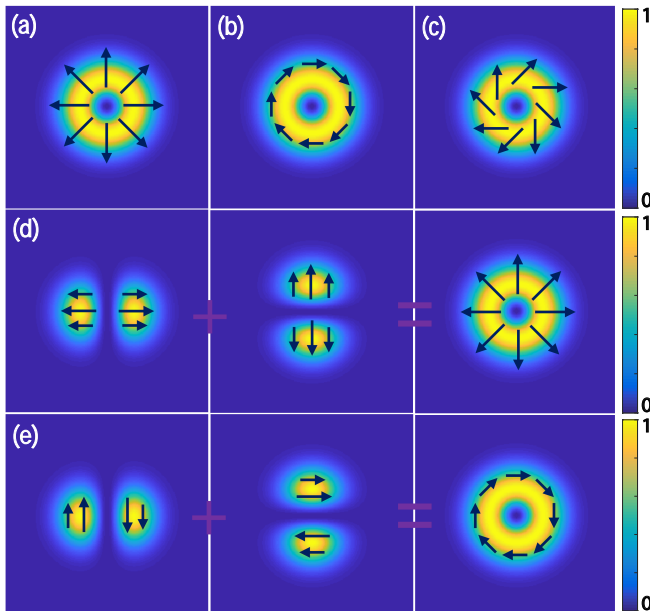
Figure 1.14: Geometry of Cylindrical Vector Beams. (a) radially polarized mode; (b) azimuthally polarized mode; (c) generalized CV beams as a linear superposition of (a) and (b). (d) radial and (e) azimuthal polarizations can be formed using linear superposition of orthogonally polarized HG modes.

a light wave passes through an an-isotropic optical element or experiences geometric transformations in the parameter spaces.

The PB phase was first put forward by Pancharatnam in his study of the interference of polarized beams in 1956 [70]. His central result, also known as Pancharatnam's rule or theorem, is that when a polarized beam returns to its original state of polarization via two intermediate polarizations, the phase does not return to its original value but increases by a phase factor equal to half of the solid angle spanned on the PS. Later in 1984 Berry discovered a geometric phase factor in a quantum systems whose parameter are cyclically altered and he also pointed out its connection with Pancharatnam's optical phase [71]. This phase was soon realized to be quite general because it occurs in various systems [72–74]. Most importantly, the PB phase enables the manipulation of light polarization, leading to the creation of vector optical fields with spatially in-homogeneous states of polarization [75, 76]. The geometric configuration of states of polarization provides an additional and powerful intrinsic DoF to control light.

PANCHARATNAM'S CONNECTION

To give a clear understanding on how the PB phase build up, we will give a brief introduction of Pancharatnam's theorem. The key concept behind Pancharatnam's theorem is the so-called Pancharatnam's connection, the criterion that two beams with different polar-

ization states are in phase when their superposition give maximum intensity. According to Equation 1.24, two different polarization states, a and b, can be written as

$$
\begin{aligned}
\boldsymbol{E}_a &= (\cos\chi_a, \sin\chi_a \exp(i\varphi_a))^T, \\
\boldsymbol{E}_b &= \exp(i\gamma_{ab})(\cos\chi_b, \sin\chi_b \exp(i\varphi_b))^T,
\end{aligned}
\tag{1.31}
$$

where γ_{ab} is the overall phase difference. According to Pancharatnam's connection, the intensity

$$
I = |\boldsymbol{E}_a + \boldsymbol{E}_b|^2 = |\boldsymbol{E}_a|^2 + |\boldsymbol{E}_b|^2 + 2\Re(\boldsymbol{E}_a^* \cdot \boldsymbol{E}_b)
\tag{1.32}
$$

reaches its maximum value, implying that

$$
\Re(\boldsymbol{E}_a^* \cdot \boldsymbol{E}_b) > 0,
\tag{1.33a}
$$

$$
\Im(\boldsymbol{E}_a^* \cdot \boldsymbol{E}_b) = 0,
\tag{1.33b}
$$

where $\Re$ denotes the real part and $\Im$ denotes the imaginary part. These two conditions can uniquely determine the phase difference γ_{ab}.

As depicted in Figure 1.13, the orange line represents the evolution of the polarization state on the PS, where the value of the PB phase ϕ_B is equal to half of the solid angle Ω enclosed by the beam's route [71, 77, 78]. In recent years, the study of the PB phase has gained significant attention in the area of structured light fields, and the creation of customized optical patterns to satisfy specific needs in all kinds of applications [79–85]. To mention a few examples, a needle of either a longitudinally or transversely polarized beam has been proposed assisted by amplitude, polarization, and phase modulations of the input light in tight focusing systems [79, 84], wherein the electric field permits a significant enhancement along the optical axis the transversal direction is suppressed, resulting in a tighter hot spot with long depth of focus. PB phase offers promising opportunities for the control and manipulation of light waves with tailored polarization states, which would enable a wide range of applications including optical information processing, quantum computing, and high accuracy measurements.

1.5. GOALS AND OUTLINE OF THE THESIS

The goal of this work is to construct effective and robust methods to improve the characterization of nanostructures by employing structured optical fields, and provide a guidance for wider industrial inspections. In this thesis, we used an analytical model to analyze and control the characteristics of focused optical fields. Then, we used a semi-analytical model to deal with the interaction process between the optical field and the structures, by monitoring the scattered field at the far field. Furthermore, the influence of the polarization state and optical singularities on the scattered field are analyzed in detail in the following chapters:

- Chapter 2: We introduce the fundamental theory of the analytical methods which are employed in this thesis to describe the scattering problems. The vectorial diffraction theory is firstly introduced, which is an analytical model and has been widely used to investigate the optical field distribution especially for highly focused conditions. After that, numerical simulation methods, which are commonly used in

optical scatterometry to predict the scattered field, are briefly introduced. Finally, the theory for analyzing the propagating characteristics the scattering field from the near field to the far field are further explained. These theories constitute the theoretical basis of this dissertation.

- Chapter 3: The properties of the incident field are the most essential topic in optical scatterometry. To generate a controllable optical field, we demonstrate an elongated focused field by specially shaping the Pancharactnam–Berry (PB) phase. Moreover, with the Richards and Wolf vectorial diffraction method, the strength vectors and energy flux of the electromagnetic fields are derived. On this basis, the transverse enhancement of a focused optical field is controllable through the phase index in the PB phase. This lays the foundation for structured light field modulation, that can play a role in the interaction of light with structures.

- Chapter 4: We propose a far-field detection system to determine the sidewall angle (SWA) of a cliff-shape step structure. Numerical calculations are carried out to verify the detection capabilities of the scheme. In the simulations, the impact of the polarization state and focus position of the incident laser beam have been considered. The results indicate that the TM polarization is more suitable for steep SWA detection than the TE mode, meanwhile, a feasible focus interval can be optimized to retrieve steep SWAs. Overall, the proposed method is fast, extremely sensitive and easy to implement, and provides a powerful approach to investigate the scattering behavior of nanostructures.

- Chapter 5: To improve the detection accuracy and broaden the measurement methods of the physical parameters of nanostructures, a novel metrology method has been proposed and demonstrated to determine simultaneously the height and side-wall angle of a step-shaped nanostructure. A Hermite-Gaussian singular beam is employed into a typical coherent Fourier scatterometry system to improve the sensitivity in retrieving parameters such as SWA and height of cliff-like nanostructures. Due to the high sensitivity driven by the singularity line of the beam, both parameters can be retrieved by analyzing the intensity profile of the far-field scattering pattern while changing the relative direction between the singularity and structure. This is an effective and robust method, and could provide a good complementary information to the CFS technique.

- Chapter 6: The transversal optical singularity (TOS) occurs perpendicular to the propagation direction, and its phase integral is 2π in nature. The TOS usually emerges within a nano-size range; thus, it provides a great possibility for accurate determination of parameters of nanostructures. We show simulations of a TOS array field that can be obtained by a three-wave interference. Our results show that the TOS scatters into the far field after its interaction with a step shaped nanostructure, and the propagation direction of the scattered TOS shows a close relation with the parameters of the step structure. Finally, by monitoring the spatial coordinates of the scattered TOS, e.g, the angle between the fitted propagation line and the axes, the physical parameters of the step nanostructure are retrieved with high precision.

1

- Chapter 7: Conclusion and outlook. A summary of the thesis and discussions for potential future work is presented.

References

[1]   G. E. Moore. "Cramming more components onto integrated circuits". In: *Proceedings of the IEEE* 86.1 (1998), pp. 82–85.

[2]   M. D. Austin and S. Y. Chou. "Fabrication of 70 nm channel length polymer organic thin-film transistors using nanoimprint lithography". In: *Applied Physics Letters* 81.23 (2002), pp. 4431–4433.

[3]   T. Mårtensson, P. Carlberg, M. Borgström, L. Montelius, W. Seifert, and L. Samuelson. "Nanowire arrays defined by nanoimprint lithography". In: *Nano letters* 4.4 (2004), pp. 699–702.

[4]   O. P. Lee, A. T. Yiu, P. M. Beaujuge, C. H. Woo, T. W. Holcombe, J. E. Millstone, J. D. Douglas, M. S. Chen, and J. M. Fréchet. "Efficient small molecule bulk heterojunction solar cells with high fill factors via pyrene-directed molecular self-assembly". In: *Advanced Materials* 23.45 (2011), pp. 5359–5363.

[5]   L. Pan, Y. Park, Y. Xiong, E. Ulin-Avila, Y. Wang, L. Zeng, S. Xiong, J. Rho, C. Sun, D. B. Bogy, *et al.* "Maskless plasmonic lithography at 22 nm resolution". In: *Scientific reports* 1.1 (2011), p. 175.

[6]   J. Benschop, V. Banine, S. Lok, and E. Loopstra. "Extreme ultraviolet lithography: Status and prospects". In: *Journal of Vacuum Science & Technology B: Microelectronics and Nanometer Structures Processing, Measurement, and Phenomena* 26.6 (2008), pp. 2204–2207.

[7]   C. W. Gwyn, R. Stulen, D. Sweeney, and D. Attwood. "Extreme ultraviolet lithography". In: *Journal of Vacuum Science & Technology B: Microelectronics and Nanometer Structures Processing, Measurement, and Phenomena* 16.6 (1998), pp. 3142–3149.

[8]   B. Wu and A. Kumar. "Extreme ultraviolet lithography: A review". In: *Journal of Vacuum Science & Technology B: Microelectronics and Nanometer Structures Processing, Measurement, and Phenomena* 25.6 (2007), pp. 1743–1761.

[9]   J. Zhu. "Profile Reconstruction Methods in Optical Scatterometry based Nanostructure Metrology". PhD thesis. Huazhong University, 2015.

[10] N. G. Orji, M. Badaroglu, B. M. Barnes, C. Beitia, B. D. Bunday, U. Celano, R. J. Kline, M. Neisser, Y. Obeng, and A. Vladar. "Metrology for the next generation of semiconductor devices". In: *Nature electronics* 1.10 (2018), pp. 532–547.

[11] Y. Shimizu, L.-C. Chen, D. W. Kim, X. Chen, X. Li, and H. Matsukuma. "An insight into optical metrology in manufacturing". In: *Measurement Science and Technology* 32.4 (2021), p. 042003.

[12] M. Haider, H. Rose, S. Uhlemann, E. Schwan, B. Kabius, and K. Urban. "A spherical-aberration-corrected 200 kV transmission electron microscope". In: *Ultramicroscopy* 75.1 (1998), pp. 53–60.

[13] M. Lentzen, B. Jahnen, C. Jia, A. Thust, K. Tillmann, and K. Urban. "High-resolution imaging with an aberration-corrected transmission electron microscope". In: *Ultramicros copy* 92.3-4 (2002), pp. 233–242.

[14] K. D. Vernon-Parry. "Scanning electron microscopy: an introduction". In: *III-Vs Review* 13.4 (2000), pp. 40–44.

[15] R. Erni, M. D. Rossell, C. Kisielowski, and U. Dahmen. "Atomic-resolution imaging with a sub-50-pm electron probe". In: *Physical review letters* 102.9 (2009), p. 096101.

[16] C. G. Frase, E. Buhr, and K. Dirscherl. "CD characterization of nanostructures in SEM metrology". In: *Measurement Science and Technology* 18.2 (2007), p. 510.

[17] C. A. Mack and B. Bunday. "CD-SEM algorithm optimization for line roughness metrology (Conference Presentation)". In: *Metrology, Inspection, and Process Control for Microlithography XXXII*. Vol. 10585. SPIE. 2018, 105850G.

[18] J. S. Villarrubia, A. Vladár, B. Ming, R. J. Kline, D. F. Sunday, J. Chawla, and S. List. "Scanning electron microscope measurement of width and shape of 10 nm patterned lines using a JMONSEL-modeled library". In: *Ultramicroscopy* 154 (2015), pp. 15–28.

[19] L. A. Giannuzzi and F. A. Stevie. "A review of focused ion beam milling techniques for TEM specimen preparation". In: *Micron* 30.3 (1999), pp. 197–204.

[20] J. Tersoff and D. R. Hamann. "Theory and application for the scanning tunneling microscope". In: *Physical review letters* 50.25 (1983), p. 1998.

[21] J. Tersoff and D. R. Hamann. "Theory of the scanning tunneling microscope". In: *Physical Review B* 31.2 (1985), p. 805.

[22] L. Tapasztó, G. Dobrik, P. Lambin, and L. P. Biro. "Tailoring the atomic structure of graphene nanoribbons by scanning tunnelling microscope lithography". In: *Nature nanotechnology* 3.7 (2008), pp. 397–401.

[23] F. J. Giessibl. "Advances in atomic force microscopy". In: *Reviews of modern physics* 75.3 (2003), p. 949.

[24] O. Custance, R. Perez, and S. Morita. "Atomic force microscopy as a tool for atom manipulation". In: *Nature nanotechnology* 4.12 (2009), pp. 803–810.

[25] S.-J. Cho, B.-W. Ahn, J. Kim, J.-M. Lee, Y. Hua, Y. K. Yoo, and S.-i. Park. "Three-dimensional imaging of undercut and sidewall structures by atomic force micros copy". In: *Review of Scientific Instruments* 82.2 (2011).

[26] R. Kizu, I. Misumi, A. Hirai, K. Kinoshita, and S. Gonda. "Development of a metrological atomic force microscope with a tip-tilting mechanism for 3D nanometrology". In: *Measurement Science and Technology* 29.7 (2018), p. 075005.

[27] T. Sugiura, T. Okada, Y. Inouye, O. Nakamura, and S. Kawata. "Gold-bead scanning near-field optical microscope with laser-force position control". In: *Optics letters* 22.22 (1997), pp. 1663–1665.

[28] A. Nesci, R. Dändliker, and H. P. Herzig. "Quantitative amplitude and phase measurement by use of a heterodyne scanning near-field optical microscope". In: *Optics letters* 26.4 (2001), pp. 208–210.

1

[29]   W. Amos, S. Reichelt, D. Cattermole, and J. Laufer. "Re-evaluation of differential phase contrast (DPC) in a scanning laser microscope using a split detector as an alternative to differential interference contrast (DIC) optics". In: *Journal of microscopy* 210.2 (2003), pp. 166–175.

[30]   H. Shang, D. Sun, P. Yu, Q. Sun, J. Gao, and T. J. Hall. "Analysis for system errors in measuring the sidewall angle of a silica waveguide with confocal laser scanning microscope (CLSM)". In: *Measurement Science and Technology* 30.2 (2019), p. 025004.

[31]   B. Maniscalco, P. Kaminski, and J. Walls. "Thin film thickness measurements using scanning white light interferometry". In: *Thin Solid Films* 550 (2014), pp. 10–16.

[32]   C. J. Raymond. "Scatterometry for semiconductor metrology". In: *Handbook of silicon semiconductor metrology*. CRC Press, 2001, pp. 389–418.

[33]   C. Raymond. "Overview of scatterometry applications in high volume silicon manufacturing". In: *AIP Conference Proceedings*. Vol. 788. 1. American Institute of Physics. 2005, pp. 394–402.

[34]   H. Kleinknecht and H. Meier. "Optical Monitoring of the Etching of SiO2 and Si3 N 4 on Si by the Use of Grating Test Patterns". In: *Journal of The Electrochemical Society* 125.5 (1978), p. 798.

[35]   H. Kleinknecht and H. Meier. "Linewidth measurement on IC masks and wafers by grating test patterns". In: *Applied Optics* 19.4 (1980), pp. 525–533.

[36]   S. Naqvi, J. McNeil, R. Krukar, and K. Bishop. "Scatterometry and the simulation of diffraction-based metrology". In: *Microlithogr. World* 2.3 (1993), pp. 5–16.

[37]   P. Ansuinelli, W. M. Coene, and H. P. Urbach. "Automatic feature selection in EUV scatterometry". In: *Applied Optics* 58.22 (2019), pp. 5916–5923.

[38]   R. L. Jones, T. Hu, E. K. Lin, W.-L. Wu, R. Kolb, D. M. Casa, P. J. Bolton, and G. G. Barclay. "Small angle x-ray scattering for sub-100 nm pattern characterization". In: *Applied physics letters* 83.19 (2003), pp. 4059–4061.

[39]   T. Novikova, A. De Martino, S. B. Hatit, and B. Drévillon. "Application of Mueller polarimetry in conical diffraction for critical dimension measurements in microelectronics". In: *Applied optics* 45.16 (2006), pp. 3688–3697.

[40]   S. Liu, X. Chen, and C. Zhang. "Development of a broadband Mueller matrix ellipsometer as a powerful tool for nanostructure metrology". In: *Thin Solid Films* 584 (2015), pp. 176–185.

[41]   O. El Gawhary, N. Kumar, S. F. Pereira, W. Coene, and H. P. Urbach. "Performance analysis of coherent optical scatterometry". In: *Applied Physics B* 105 (2011), pp. 775–781.

[42]   S. Roy, A. C. Assafrao, S. F. Pereira, and H. P. Urbach. "Coherent Fourier scatterometry for detection of nanometer-sized particles on a planar substrate surface". In: *Optics express* 22.11 (2014), pp. 13250–13262.

[43]   J. Geng. "Structured-light 3D surface imaging: a tutorial". In: *Advances in optics and photonics* 3.2 (2011), pp. 128–160.

[44]   M. Saxena, G. Eluru, and S. S. Gorthi. "Structured illumination microscopy". In: *Advances in Optics and Photonics* 7.2 (2015), pp. 241–275.

[45]   M.-J. Tsai and C.-C. Hung. "Development of a high-precision surface metrology system using structured light projection". In: *Measurement* 38.3 (2005), pp. 236–247.

[46]   A. Trichili, K.-H. Park, M. Zghal, B. S. Ooi, and M.-S. Alouini. "Communicating using spatial mode multiplexing: Potentials, challenges, and perspectives". In: *IEEE Communications Surveys & Tutorials* 21.4 (2019), pp. 3175–3203.

[47]   Y. Yang, Y.-X. Ren, M. Chen, Y. Arita, and C. Rosales-Guzmán. "Optical trapping with structured light: a review". In: *Advanced Photonics* 3.3 (2021), pp. 034001–034001.

[48]   M. Erhard, R. Fickler, M. Krenn, and A. Zeilinger. "Twisted photons: new quantum perspectives in high dimensions". In: *Light: Science & Applications* 7.3 (2018), pp. 17146–17146.

[49]   Y. Shen, X. Wang, Z. Xie, C. Min, X. Fu, Q. Liu, M. Gong, and X. Yuan. "Optical vortices 30 years on: OAM manipulation from topological charge to multiple singularities". In: *Light: Science & Applications* 8.1 (2019), p. 90.

[50]   Z. Liu, Y. Liu, Y. Ke, Y. Liu, W. Shu, H. Luo, and S. Wen. "Generation of arbitrary vector vortex beams on hybrid-order Poincaré sphere". In: *Photonics Research* 5.1 (2017), pp. 15–21.

[51]   K. S. Youngworth and T. G. Brown. "Focusing of high numerical aperture cylindrical-vector beams". In: *Optics Express* 7.2 (2000), pp. 77–87.

[52]   G. Lazarev, P.-J. Chen, J. Strauss, N. Fontaine, and A. Forbes. "Beyond the display: phase-only liquid crystal on silicon devices and their applications in photonics". In: *Optics express* 27.11 (2019), pp. 16206–16249.

[53]   Y.-X. Ren, R.-D. Lu, and L. Gong. "Tailoring light with a digital micromirror device". In: *Annalen der physik* 527.7-8 (2015), pp. 447–470.

[54]   A. Rubano, F. Cardano, B. Piccirillo, and L. Marrucci. "Q-plate technology: a progress review". In: *JOSA B* 36.5 (2019), pp. D70–D87.

[55]   K. Y. Bliokh, F. J. Rodríguez-Fortuño, F. Nori, and A. V. Zayats. "Spin–orbit interactions of light". In: *Nature Photonics* 9.12 (2015), pp. 796–808.

[56]   A. Forbes, M. de Oliveira, and M. R. Dennis. "Structured light". In: *Nature Photonics* 15.4 (2021), pp. 253–262.

[57]   R. Grella. "Fresnel propagation and diffraction and paraxial wave equation". In: *Journal of Optics* 13.6 (1982), p. 367.

[58]   L. Allen, M. W. Beijersbergen, R. Spreeuw, and J. Woerdman. "Orbital angular momentum of light and the transformation of Laguerre-Gaussian laser modes". In: *Physical review A* 45.11 (1992), p. 8185.

[59]   J. F. Nye and M. V. Berry. "Dislocations in wave trains". In: *Proceedings of the Royal Society of London. A. Mathematical and Physical Sciences* 336.1605 (1974), pp. 165–190.

1

[60] M. Vasnetsov, V. Gorshkov, I. Marienko, and M. Soskin. "Wavefront motion in the vicinity of a phase dislocation:"optical vortex"". In: *Optics and Spectroscopy* 88 (2000), pp. 260–265.

[61] L. Wang, Q.-F. Wang, X.-Q. Wang, and B.-D. Lü. "Transversal optical vortex in the interference field of two off-axis Gaussian beams". In: (2007).

[62] P. Liu and B. Lü. "Phase singularities of the transverse field component of high numerical aperture dark-hollow Gaussian beams in the focal region". In: *Optics communications* 272.1 (2007), pp. 1–8.

[63] K. O'holleran, M. J. Padgett, and M. R. Dennis. "Topology of optical vortex lines formed by the interference of three, four, and five plane waves". In: *Optics Express* 14.7 (2006), pp. 3039–3044.

[64] M. R. Dennis, K. O'holleran, and M. J. Padgett. "Singular optics: optical vortices and polarization singularities". In: *Progress in optics*. Vol. 53. Elsevier, 2009, pp. 293–363.

[65] Q. Wang, C.-H. Tu, Y.-N. Li, and H.-T. Wang. "Polarization singularities: Progress, fundamental physics, and prospects". In: *Apl Photonics* 6.4 (2021), p. 040901.

[66] Z. Man, S. Fu, and G. Wei. "Focus engineering based on analytical formulae for tightly focused polarized beams with arbitrary geometric configurations of linear polarization". In: *JOSA A* 34.8 (2017), pp. 1384–1391.

[67] G. Arora, P. Senthilkumaran, *et al.* "Hybrid order Poincaré spheres for Stokes singularities". In: *Optics Letters* 45.18 (2020), pp. 5136–5139.

[68] D. G. Hall. "Vector-beam solutions of Maxwell's wave equation". In: *Optics letters* 21.1 (1996), pp. 9–11.

[69] L. Novotny and B. Hecht. "Surface plasmons". In: *Principles of Nano-Optics* 90 (2006), p. 378.

[70] S. Pancharatnam and S. Pancharatnam. "Generalized theory of interference, and its applications". In: *Resonance* 18.4 (2013), pp. 387–389.

[71] M. V. Berry. "The adiabatic phase and Pancharatnam's phase for polarized light". In: *Journal of Modern Optics* 34.11 (1987), pp. 1401–1407.

[72] J. Samuel and R. Bhandari. "General setting for Berry's phase". In: *Physical Review Letters* 60.23 (1988), p. 2339.

[73] T. F. Jordan. "Berry phases for partial cycles". In: *Physical Review A* 38.3 (1988), p. 1590.

[74] M. Berry *et al.* "Anticipations of the geometric phase". In: *Physics Today* 43.12 (1990), pp. 34–40.

[75] Z. Bomzon, V. Kleiner, and E. Hasman. "Pancharatnam–Berry phase in space-variant polarization-state manipulations with subwavelength gratings". In: *Optics letters* 26.18 (2001), pp. 1424–1426.

[76] J. B. Mueller, N. A. Rubin, R. C. Devlin, B. Groever, and F. Capasso. "Metasurface polarization optics: independent phase control of arbitrary orthogonal states of polarization". In: *Physical review letters* 118.11 (2017), p. 113901.

1

[77]   R. Bhandari. "Polarization of light and topological phases". In: *Physics Reports* 281.1 (1997), pp. 1–64.

[78]   T. Van Dijk, H. F. Schouten, W. Ubachs, and T. D. Visser. "The Pancharatnam-Berry phase for non-cyclic polarization changes". In: *Optics Express* 18.10 (2010), pp. 10796–10804.

[79]   H. Wang, L. Shi, B. Lukyanchuk, C. Sheppard, and C. T. Chong. "Creation of a needle of longitudinally polarized light in vacuum using binary optics". In: *Nature photonics* 2.8 (2008), pp. 501–505.

[80]   F. Maucher, S. Skupin, S. Gardiner, and I. Hughes. "Creating complex optical longitudinal polarization structures". In: *Physical Review Letters* 120.16 (2018), p. 163903.

[81]   T. Bauer, P. Banzer, E. Karimi, S. Orlov, A. Rubano, L. Marrucci, E. Santamato, R. W. Boyd, and G. Leuchs. "Observation of optical polarization Möbius strips". In: *Science* 347.6225 (2015), pp. 964–966.

[82]   F. Bouchard, H. Larocque, A. M. Yao, C. Travis, I. De Leon, A. Rubano, E. Karimi, G.-L. Oppo, and R. W. Boyd. "Polarization shaping for control of nonlinear propagation". In: *Physical Review Letters* 117.23 (2016), p. 233903.

[83]   P. Li, X. Guo, S. Qi, L. Han, Y. Zhang, S. Liu, Y. Li, and J. Zhao. "Creation of independently controllable multiple focal spots from segmented Pancharatnam-Berry phases". In: *Scientific Reports* 8.1 (2018), p. 9831.

[84]   Z. Man, C. Min, L. Du, Y. Zhang, S. Zhu, and X. Yuan. "Sub-wavelength sized transversely polarized optical needle with exceptionally suppressed side-lobes". In: *Optics Express* 24.2 (2016), pp. 874–882.

[85]   V. V. Kotlyar, A. A. Kovalev, and A. G. Nalimov. "Energy density and energy flux in the focus of an optical vortex: reverse flux of light energy". In: *Optics Letters* 43.12 (2018), pp. 2921–2924.

2

A SEMI-ANALYTICAL METHOD FOR THE SCATTERING PROBLEM

2.1. INTRODUCTION

We have discussed in Section 1.3 how one can implement CFS technique to deal with the problem of structural parameter measurement. Unlike the conventional angular and the spectroscopic scatterometers, CFS uses a beam of light focused by a objective with a specified NA. The field distribution in the focal region needs to be calculated by a suitable method according to different focusing conditions. For instance, when the NA of the objective lens is relatively small, the focused field can be calculated by the scalar diffraction theory, whereas when the NA gradually increases, the field distribution at the focal region will have not only transversal but also longitudinal components due to depolarisation effects. Thus, the scalar theory is no longer able to accurately describe the behavior of the focused field, and therefore a vectorial diffraction theory has to be adopted. The analytical model for a high NA focusing system is first presented in Section 2.2. Following that, we take the properties of the input beam into account and further provide the analytical expressions for arbitrary polarized beam, which is the most important mathematical basis for the generation of the desired structured light field. We further evaluate the effect of input ellipticity, handedness, and orientation on all components of the electric and magnetic field strengths, as well as the Poynting vector near focus.

The investigation of scattering behavior of the desired light probe after interacting with the sample of interest is a crucial part in CFS. Establishing an analytical solution to explain the scattering problem between the focusing field and complex structures is challenging, and in most case, even impossible. The scattering problem has consistently posed difficulties in the field of optics and holds a long-standing history dating back over a century. Gustav Mie derived a rigorous mathematical solution for elastic scattering of a homogeneous sphere by solving Maxwell's equations in 1908. This renowned solution, known as Mie scattering theory, enables an analytical calculation of scattering from spherical particles of varying sizes and materials.

If we employ the Mie scattering theory to deal with the scattering behavior of irregular (asymmetric) objects, it typically requires a multipole expansion, which represents the scattering field of the irregular object as a linear combination of a series of multipole moments to approximate the scattering behavior. The accuracy of the expansion depends on the number of multipole orders, and higher orders generally lead to more accurate results but also increase computational complexity. It is important to note that the multipole expansion remains an approximation method in the calculation of scattering from irregular objects, and it may have limitations when dealing with complex geometric shapes or non-uniform scattering characteristics. For more accurate results, other methods such as numerical simulations and experimental measurements are commonly used to solve the scattering problem. Numerical simulations based on electromagnetic theory offer a more feasible method, which facilitates rapid modeling, optimization of structural parameters, and reduction of experimental costs. In this thesis, we mainly rely on the Finite Difference Time Domain (FDTD) method to carry out our numerical modeling task. In Section 2.3, a detailed explanation of FDTD algorithm and a brief introduction of the solver are presented.

As a far-field detection method, the obtained near-field scattering signals in CFS need to be projected to the far-field for further processing. We discuss about the relevant theories

of near-field and far-field transformation in Section 2.4. In conclusion, we established a semi-analytical method to solve the scattering problem for the structural parameter retrieval.

2.2. THE TIGHT-FOCUSING ANALYSIS OF VECTOR BEAM

The Richard-Wolf vector diffraction theory [2, 3] is the most widely used vectorial diffraction method to express a tightly focused field. Such field is calculated by solving the diffraction integral of the focused field spectrum, and then using the Debye-Wolf approximation for the beams [4, 5]. The well defined integral representation of the focused field is called the Debye-Wolf integral, which is the kernel part to generate our desired illumination in this thesis. We rely on the references [6–8] to give the following detailed expressions.
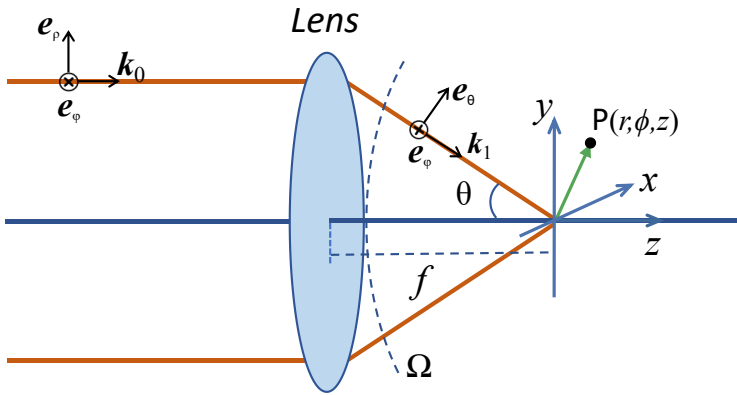
Figure 2.1: Schematic of an incident paraxial ray focusing through an objective lens with high NA.

Consider a monochromatic plane wave $\boldsymbol{E}_{\text{in}}$ propagating along the z direction, which will pass through a spherical objective lens with focal distance f. The time harmonic electric field for an arbitrary point $P(x, y, z)$ in the image space, which contains time dependence in the form of $e^{-i\omega t}$, is given by:

$$
\begin{aligned}
\boldsymbol{E}(P, t) &= \Re\left[\boldsymbol{e}(P) e^{-i\omega t}\right], \\
\boldsymbol{H}(P, t) &= \Re\left[\boldsymbol{h}(P) e^{-i\omega t}\right],
\end{aligned}
\tag{2.1}
$$

where $\boldsymbol{e}(P)$ and $\boldsymbol{h}(P)$ are the complex electric and magnetic field vectors, which can be obtained by integrating over the exit pupil (dk_x, dk_y). The field in the focal region is given

by:

$$e(P) = -\frac{ik}{2\pi} \iint_\Omega \frac{\mathbf{a}(k_x, k_y)}{k_z} \exp\{i\mathbf{k}\cdot\mathbf{r}_P\} dk_x dk_y,$$
$$h(P) = -\frac{ik}{2\pi} \iint_\Omega \frac{\mathbf{b}(k_x, k_y)}{k_z} \exp\{i\mathbf{k}\cdot\mathbf{r}_P\} dk_x dk_y,$$

(2.2)

where Ω is the solid angle subtended by the aperture of the lens at the paraxial focal point, which is controlled by the maximum incidence angle θ of the lens and $d\Omega = 1/k_z dk_x dk_y$ is an element of the solid angle formed by the k-directions, $\mathbf{a}(k_x, k_y)$ and $\mathbf{b}(k_x, k_y)$ are the 'strength factors' of the unperturbed electromagnetic field, $\mathbf{k}$ is the wave vector pointing from the spherical pupil to the focus, $\mathbf{r}_P$ is the vector from the focus to the point P. $\mathbf{a}(k_x, k_y)$ and $\mathbf{b}(k_x, k_y)$ are defined by the following relations

$$\mathbf{b}(k_x, k_y) = \sqrt{\frac{\varepsilon}{\mu}} \mathbf{k} \times \mathbf{a}(k_x, k_y),$$

(2.3)

where ε and μ represent the permittivity and permeability in the image space.

It is convenient to use polar coordinates (e_ρ, e_φ, e_z) in the entrance pupil and use spherical variables $(e_\theta, e_\varphi, e_r)$ in $\mathbf{k}$-space for the rays derived upon refraction through lens, as shown in Figure 2.1. Upon the refraction surface, vectors e_ρ and e_z transform into e_θ, and e_r, respectively, while e_φ remains the same. Also defined are the angles α and ϕ used to describe the direction of the wave vector in the focal plane. Assume that the lens fulfills the Abbe sine condition $\rho = f \sin\alpha$, and the polar coordinates of the pupil point corresponding to the wave vector satisfy the following relationship $\phi = \varphi + \pi$. For an aplanatic system, the refraction surface is a spherical shell limited by its numerical aperture $NA = n \sin\alpha$, where n is the refractive index of the medium between the lens and the focal region. We then express the propagation vector $\mathbf{k}$ in image space in spherical coordinates, and the arbitrary point P in image space in cylindrical coordinates, as follows:

$$\mathbf{k} = (k\sin\theta\cos\phi, k\sin\theta\sin\phi, k\cos\theta),$$
$$= (-\sin\theta\cos\varphi, -\sin\theta\sin\varphi, \cos\theta),$$
$$\mathbf{r}_P = (r_P\cos\phi_P, r_P\sin\phi_P, z_P).$$

(2.4)

Upon solving for $1/k_z dk_x dk_y = \sin\theta d\theta d\varphi$, we can rewrite the integral Equation 2.2 in the following form:

$$e(P) = -\frac{ik}{2\pi} \int_0^\alpha \int_0^{2\pi} \mathbf{a}(\theta, \varphi) \exp\{ik[-r_P\sin\theta\cos(\varphi-\phi_P) + z_P\cos\theta]\} \sin\theta d\theta d\varphi$$
$$h(P) = -\frac{ik}{2\pi} \int_0^\alpha \int_0^{2\pi} \mathbf{b}(\theta, \varphi) \exp\{ik[-r_P\sin\theta\cos(\varphi-\phi_P) + z_P\cos\theta]\} \sin\theta d\theta d\varphi.$$

(2.5)

The strength factor $\mathbf{a}(\theta, \varphi)$ and $\mathbf{b}(\theta, \varphi)$ (for the detailed derivation of see Appendix A, are

given by

$$
\mathbf{a}(\theta,\varphi) = f\,l_{\text{in}}\sqrt{\cos\theta}
\begin{bmatrix}
e_{\text{in}}^x\{\cos\theta + \sin^2\varphi(1-\cos\theta)\} + e_{\text{in}}^y\{\cos\varphi\sin\varphi(\cos\theta-1)\} \\
e_{\text{in}}^x\{\cos\varphi\sin\varphi(\cos\theta-1)\} + e_{\text{in}}^y\{1 - \sin^2\varphi(1-\cos\theta)\} \\
e_{\text{in}}^x\sin\theta\cos\varphi + e_{\text{in}}^y\sin\theta\sin\varphi
\end{bmatrix},
$$

$$
\mathbf{b}(\theta,\varphi) = \sqrt{\frac{\varepsilon}{\mu}}\,f\,l_{\text{in}}\sqrt{\cos\theta}
\begin{bmatrix}
-e_{\text{in}}^y\{\cos\theta + \sin^2\varphi(1-\cos\theta)\} + e_{\text{in}}^x\{\cos\varphi\sin\varphi(\cos\theta-1)\} \\
-e_{\text{in}}^y\{\cos\varphi\sin\varphi(\cos\theta-1)\} + e_{\text{in}}^x\{1 - \sin^2\varphi(1-\cos\theta)\} \\
-e_{\text{in}}^y\sin\theta\cos\varphi + e_{\text{in}}^x\sin\theta\sin\varphi.
\end{bmatrix}
$$

(2.6)

where l_{in} is the input beam, e_{in}^x and e_{in}^y are the corresponding amplitudes of the input beam in global Cartesian coordinates. Substituting Equation 2.6 into Equation 2.5, gives the electric field distribution as:

$$
\boldsymbol{e}(P) = -\frac{ikf}{2\pi}\int_0^\alpha\int_0^{2\pi} l_{\text{in}}\sqrt{\cos\theta}\sin\theta\exp\{ik[-r_P\sin\theta\cos(\varphi-\phi_P)+\cos\theta z_P]\}
$$
$$
\begin{bmatrix}
e_{\text{in}}^x\{\cos\theta + \sin^2\varphi(1-\cos\theta)\} + e_{\text{in}}^y\{\cos\varphi\sin\varphi(\cos\theta-1)\} \\
e_{\text{in}}^x\{\cos\varphi\sin\varphi(\cos\theta-1)\} + e_{\text{in}}^y\{1 - \sin^2\varphi(1-\cos\theta)\} \\
e_{\text{in}}^x\sin\theta\cos\varphi + e_{\text{in}}^y\sin\theta\sin\varphi
\end{bmatrix} d\theta d\varphi.
$$

$$
\boldsymbol{h}(P) = -\frac{ikf}{2\pi}\sqrt{\frac{\varepsilon}{\mu}}\int_0^\alpha\int_0^{2\pi} l_{\text{in}}\sqrt{\cos\theta}\sin\theta\exp\{ik[-r_P\sin\theta\cos(\varphi-\phi_P)+\cos\theta z_P]\}
$$
$$
\begin{bmatrix}
-e_{\text{in}}^y\{\cos\theta + \sin^2\varphi(1-\cos\theta)\} + e_{\text{in}}^x\{\cos\varphi\sin\varphi(\cos\theta-1)\} \\
-e_{\text{in}}^y\{\cos\varphi\sin\varphi(\cos\theta-1)\} + e_{\text{in}}^x\{1 - \sin^2\varphi(1-\cos\theta)\} \\
-e_{\text{in}}^y\sin\theta\cos\varphi + e_{\text{in}}^x\sin\theta\sin\varphi
\end{bmatrix} d\theta d\varphi.
$$

(2.7)

By employing the aforementioned expression, an analytical expression for the focusing field corresponding to arbitrary paraxial input field ($e_{\text{in}}^x\boldsymbol{e}_x, e_{\text{in}}^y\boldsymbol{e}_y, 0$) can be obtained.

As we know, for any given polarized optical field, its corresponding state of polarization (SoP) in theory may be described by a combination of a pair of orthogonal base vectors. Mathematically, all SoPs on the standard PS may be described in the Cartesian coordinate system as a unit vector given by

$$
\boldsymbol{V} = \frac{1}{\sqrt{2}}\left[\exp(ia)(\cos b\boldsymbol{e}_x + \sin b\boldsymbol{e}_y) + \exp(-ia)(-\sin b\boldsymbol{e}_x + \cos b\boldsymbol{e}_y)\right],
\tag{2.8}
$$

where both a and b are constants, controlling the ellipticity and orientation, respectively. The unit vectors $\boldsymbol{e}_x$ and $\boldsymbol{e}_y$, are directed along the x and y axes, respectively.

When the input field with polarization distribution represented by Equation 2.8 is incident upon this focusing system, then based on the Equation 2.7, the electric field at any point $P(r_P, \phi_P, z_P)$ near focus can be expressed in a more compact form as

$$
\boldsymbol{e}(P) = \begin{bmatrix} E_x(r_P,\phi_P,z_P) \\ E_y(r_P,\phi_P,z_P) \\ E_z(r_P,\phi_P,z_P) \end{bmatrix}
$$
$$
= -\frac{ikf}{2\pi}\int_0^\alpha\int_0^{2\pi}\sqrt{\cos\theta}\,l_0(\theta)K(\varphi,\theta)\boldsymbol{M}_E\sin\theta d\varphi d\theta.
$$

(2.9)

For our following calculations, we chose NA = 0.95 and $n = 1$; the function $l_0(\theta)$, which represents the input amplitude distribution, has the form

$$l_0(\theta) = \exp\left[-\beta^2\left(\frac{\sin\theta}{\sin\alpha}\right)^2\right]J_1\left(2\beta\frac{\sin\theta}{\sin\alpha}\right), \tag{2.10}$$

where β is the ratio of the pupil radius to the beam waist, which we take as unity in our configuration, J_1 the first-order Bessel function of the first kind, and $K(\varphi,\theta)$ is the focusing propagation factor given by

$$K(\varphi,\theta) = \exp\left\{ik[-r_p\sin\theta\cos(\varphi-\phi_p)+z_p\cos\theta]\right\}. \tag{2.11}$$

In equation 2.9, $\boldsymbol{M}_E$ is the electric polarization vector in the strongly focused field and stems from the polarization contribution of the incident light field. When the input SoP is denoted by equation 2.8, the corresponding focusing electric polarization vector is

$$M_E^x = \frac{1}{\sqrt{2}}\{[\cos(b-\varphi)\cos\theta\cos\varphi - \sin(b-\varphi)\sin\varphi]\exp(ia) \tag{2.12a}$$
$$- [\sin(b-\varphi)\cos\theta\cos\varphi + \cos(b-\varphi)\sin\varphi]\exp(-ia)\},$$

$$M_E^y = \frac{1}{\sqrt{2}}\{[\cos(b-\varphi)\cos\theta\sin\varphi + \sin(b-\varphi)\cos\varphi]\exp(ia) \tag{2.12b}$$
$$- [\sin(b-\varphi)\cos\theta\sin\varphi - \cos(b-\varphi)\cos\varphi]\exp(-ia)\},$$

$$M_E^z = \frac{1}{\sqrt{2}}\{\cos(b-\varphi)\sin\theta\exp(ia) - \sin(b-\varphi)\sin\theta\exp(-ia)\}. \tag{2.12c}$$

The integrations over φ can be accomplished using the identity:

$$\int_0^{2\pi} e^{-ikr_P\sin\theta\cos(\varphi-\phi_P)}e^{im\varphi}d\varphi = 2\pi i^m J_m(-kr_P\sin\theta)e^{im\phi_P}, \tag{2.13}$$

where J_m is the Bessel function of the first kind of order m. The electric fields near focus then have the following form:

$$E_x(r_P,\phi_P,z_P) = -\frac{ikf}{2\sqrt{2}}\int_0^\alpha \sqrt{\cos\theta}\, l_0(\theta)\sin\theta\cdot \tag{2.14a}$$
$$\Big\{\big[\cos b(\cos\theta+1)J_0(-kr_P\sin\theta)$$
$$+ \cos(b-2\phi_P)\times(1-\cos\theta)J_2(-kr_P\sin\theta)\big]e^{ia}$$
$$- \big[\sin b(\cos\theta+1)J_0(-kr_P\sin\theta)$$
$$+ \sin(b-2\phi_P)\times(1-\cos\theta)J_2(-kr_P\sin\theta)\big]e^{-ia}\Big\}e^{ikz_P\cos\theta}d\theta,$$

$$E_y(r_P,\phi_P,z_P) = -\frac{ikf}{2\sqrt{2}}\int_0^\alpha \sqrt{\cos\theta}\, l_0(\theta)\sin\theta\cdot \tag{2.14b}$$
$$\Big\{\big[\sin b(\cos\theta+1)J_0(-kr_P\sin\theta)$$

$$-\sin(b-2\phi_P)\times(1-\cos\theta)J_2(-kr_P\sin\theta)\big]e^{ia}$$
$$-\big[\cos b(\cos\theta+1)J_0(-kr_P\sin\theta)$$
$$-\cos(b-2\phi_P)\times(1-\cos\theta)J_2(-kr_P\sin\theta)\big]e^{-ia}\Big\}e^{ikz_P\cos\theta}\,d\theta,$$

$$E_z(r_P,\phi_P,z_P) = \frac{kf}{\sqrt{2}}\int_0^\alpha \sqrt{\cos\theta}\,l_0(\theta)\sin\theta^2 J_0(-kr_P\sin\theta)\cdot \tag{2.14c}$$
$$\big[\cos(b-\phi_P)e^{ia}-\sin(b-\phi_P)e^{-ia}\big]e^{ikz_P\cos\theta}\,d\theta.$$

Obviously, the three mutually perpendicular polarization components are nonzero, which means that the local polarization ellipse of the focused field is not purely in the transverse plane or longitudinal plane. Similarly, the corresponding magnetic field at any point $P(r_P,\phi_P,z_P)$ near focus can be expressed as

$$\boldsymbol{h}(P) = \begin{bmatrix} H_x(r_P,\phi_P,z_P) \\ H_y(r_P,\phi_P,z_P) \\ H_z(r_P,\phi_P,z_P) \end{bmatrix} \tag{2.15}$$
$$= -\frac{ikf}{2\pi}\int_0^\alpha\int_0^{2\pi}\sqrt{\cos\theta}\,l_0(\theta)K(\varphi,\theta)\boldsymbol{M}_H\sin\theta\,d\varphi\,d\theta,$$

where $\boldsymbol{M}_H$ is the magnetic polarization vector in the tightly focused field given by

$$M_H^x = \sqrt{\frac{\varepsilon}{2\mu}}\{[-\sin(b-\varphi)\cos\theta\cos\varphi-\cos(b-\varphi)\sin\varphi]\exp(ia) \tag{2.16a}$$
$$-[\cos(b-\varphi)\cos\theta\cos\varphi-\sin(b-\varphi)\sin\varphi]\exp(-ia)\},$$

$$M_H^y = \sqrt{\frac{\varepsilon}{2\mu}}\{[-\sin(b-\varphi)\cos\theta\sin\varphi+\cos(b-\varphi)\cos\varphi]\exp(ia) \tag{2.16b}$$
$$-[\cos(b-\varphi)\cos\theta\sin\varphi+\sin(b-\varphi)\cos\varphi]\exp(-ia)\},$$

$$M_H^z = \sqrt{\frac{\varepsilon}{2\mu}}\{-\sin(b-\varphi)\sin\theta\exp(ia)-\cos(b-\varphi)\sin\theta\exp(-ia)\}. \tag{2.16c}$$

The integrations over φ can be accomplished as before, yielding

$$H_x(r_P,\phi_P,z_P) = -\frac{ikf\sqrt{\varepsilon/\mu}}{2\sqrt{2}}\int_0^\alpha\sqrt{\cos\theta}\,l_0(\theta)\sin\theta\cdot \tag{2.17a}$$
$$\Big\{\big[-\sin b(\cos\theta+1)J_0(-kr_P\sin\theta)$$
$$-\sin(b-2\phi_P)\times(1-\cos\theta)J_2(-kr_P\sin\theta)\big]e^{ia}$$
$$-\big[\cos b(\cos\theta+1)J_0(-kr_P\sin\theta)$$
$$+\cos(b-2\phi_P)\times(1-\cos\theta)J_2(-kr_P\sin\theta)\big]e^{-ia}\Big\}e^{ikz_P\cos\theta}\,d\theta,$$

$$H_y(r_P,\phi_P,z_P) = -\frac{ikf\sqrt{\varepsilon/\mu}}{2\sqrt{2}}\int_0^\alpha\sqrt{\cos\theta}\,l_0(\theta)\sin\theta\cdot \tag{2.17b}$$

$$\left\{\left[\cos b(\cos\theta+1)J_0(-kr_P\sin\theta)\right.\right.$$
$$\left.-\cos(b-2\phi_P)\times(1-\cos\theta)J_2(-kr_P\sin\theta)\right]e^{ia}$$
$$-\left[\sin b(\cos\theta+1)J_0(-kr_P\sin\theta)\right.$$
$$\left.\left.-\sin(b-2\phi_P)\times(1-\cos\theta)J_2(-kr_P\sin\theta)\right]e^{-ia}\right\}e^{ikz_P\cos\theta}d\theta,$$

$$H_z(r_P,\phi_P,z_P)=\frac{ikf\sqrt{\varepsilon/\mu}}{\sqrt{2}}\int_0^\alpha\sqrt{\cos\theta}\,l_0(\theta)\sin2\theta J_1(-kr_P\sin\theta)\cdot \tag{2.17c}$$
$$\left[-\sin(b-\phi_P)e^{ia}-\cos(b-\phi_P)e^{-ia}\right]e^{ikz_P\cos\theta}d\theta.$$

In terms of the three-dimensional electric and magnetic fields, the energy flux is given by the time-averaged Poynting vector

$$\mathbf{P}\propto\Re(\mathbf{e}\times\mathbf{h}^*). \tag{2.18}$$

We calculate the energy flux of the tightly focused standard full Poincaré beams using Equations 2.14, 2.17 and 2.18.
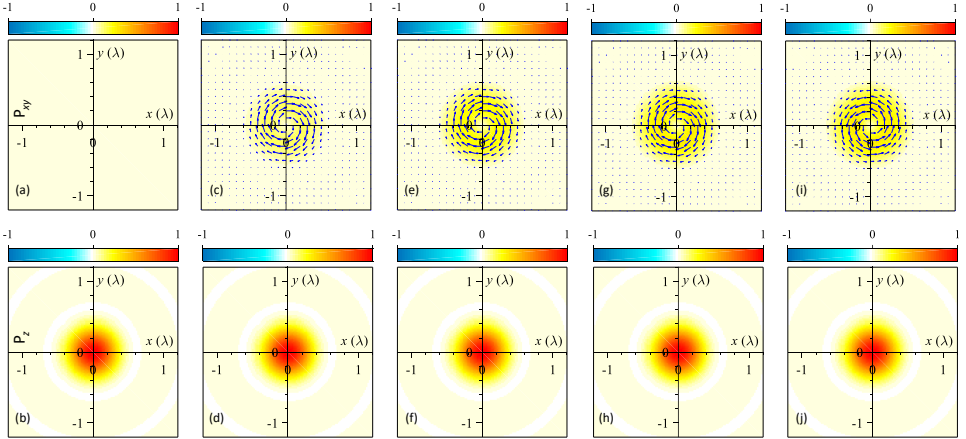
Figure 2.2: Theory-derived Poynting vector in the focal plane of tightly focused input fields with $a=0,\pi/12,\pi/6,\pi/4$ and $-\pi/4$ when $b=-\pi/4$. The upper and lower rows depict the transverse and longitudinal components of the energy flux, respectively. All distributions of the energy flux are normalized to their maximum values of the total energy flux for each input field to enable a direct comparison between the five beams.

Next, we discuss the effect of the optical DoFs including ellipticity and handedness on the energy flux. By calculation, we find that both ellipticity and handedness mainly affect the transverse energy flow, and the longitudinal energy flow remains almost unchanged regardless of ellipticity and handedness. The Poynting vectors of the five tightly focused electric fields are drawn in Figure 2.2. We see that the transverse energy flow is zero for a spin-free input field ($a=0$), whereas for other values of this flow exists and always exhibits a doughnut-shaped pattern [Figure 2.2(c), (e), (g), and (i)], arising from the spin-to-orbital angular momentum conversion. Furthermore, the magnitude of the transverse

component of the Poynting vector, compared with the longitudinal component [Figure 2.2(b), (d), (f), (h), and (i)], gradually increases as $|a|$ increases. Moreover, we find that the handedness of the input field only affects the direction of the transverse energy flow and has no effect on the magnetic field [Figure 2.2(g) and (i)].
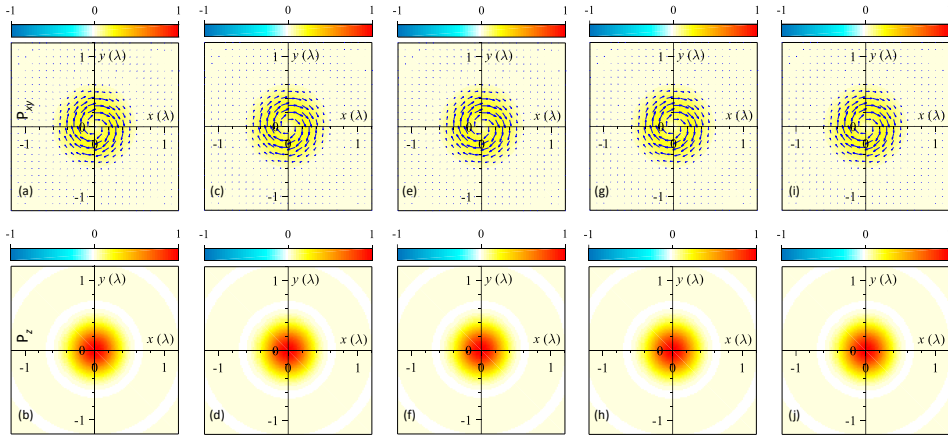

Figure 2.3: Same as for Figure 2.2 but with $b = -\pi/4$, $-\pi/8$, 0, $\pi/8$ and $\pi/4$ when $a = -\pi/8$.

In contrast to the optical DoFs, i.e. ellipticity and handedness, orientation has no effect on both the transverse and longitudinal energy flows (see Figure 2.3 depicting the energy flux in the focal plane of five input fields). Apparently, the transverse energy, which has a ring-shaped pattern, always exhibits the same magnitude and direction with a change of input orientation (upper row in Figure 2.3). Similarly, the longitudinal energy flow has a hot spot located on-axis (lower row in Figure 2.3).

2.3. NUMERICAL SIMULATION METHOD

In optical scatterometry, several methods are commonly used to numerically compute the solution of an electromagnetic scattering problem. These include: the rigorous coupled wave analysis (RCWA) [9], the finite element method (FEM) [10], and the finite difference time domain (FDTD) method [11].

RCWA, also known as the Fourier modal method, is a numerical method for solving grating problems. It slices the grating geometry into slabs, treating them as periodically modulated planar waveguides. By solving eigenequations of waveguide modes through Maxwell's equations and matching the field at interfaces of the slabs, the electromagnetic field and diffraction efficiencies outside the grating structure can be obtained. RCWA provides a fast and reliable calculation of the diffraction field of periodic structures.

FEM is a numerical method originally applied in structural mechanics and thermo-dynamic theory. Its main principle involves decomposing the complex large-area continuous field into a series of non-overlapping small-area discrete fields. Approximate solutions are then used for these small areas. It is characterized by its ability to handle complex geometries and material inhomogeneity, the capability to bring thermal or me-

chanical solutions into electromagnetic results, and its applicability to multi-disciplinary problems.

FDTD is a numerical method that directly solves Maxwell's equations in the time domain. In this method, the equations are represented in terms of central-difference equations, and the components of the electromagnetic field are sampled alternately in space and time domains. This allows for the calculation of electric and magnetic field distributions corresponding to different times and space points. FDTD is suitable for arbitrarily complex geometries and is used in this thesis for modeling the interaction of focused light with nano-structures. It is worth mentioning that although the FEM also can simulate the interaction between the focusing field and nanostructures, it consumes more computational resources than FDTD. Therefore, when dealing exclusively with electromagnetic field problems, FDTD is both faster and more resource-efficient. The following section will provide a brief introduction to its working principle.

2.3.1. FDTD ALGORITHM

Maxwell's equations consist of four equations which are a set of fundamental equations that govern macroscopic electromagnetic phenomena. This set of equations can be written in both differential form and integral form. Considering a source-free situation (no electric and magnetic current source), the partial differential form of Maxwell's equations in time domain is:

$$\nabla \times \boldsymbol{H} = \frac{\partial \boldsymbol{D}}{\partial t} + \boldsymbol{J},$$
$$\nabla \times \boldsymbol{E} = -\frac{\partial \boldsymbol{B}}{\partial t} - \boldsymbol{J}^*,$$
$$\nabla \bullet \boldsymbol{D} = 0, \qquad (2.19)$$
$$\nabla \bullet \boldsymbol{B} = 0.$$

where $\boldsymbol{H}$ is the magnetic field strength, $\boldsymbol{E}$ is the electric field strength, $\boldsymbol{D}$ is the electric induction strength, $\boldsymbol{B}$ is the magnetic induction strength, $\boldsymbol{J}$ is the current density, $\boldsymbol{J}^*$ is an imaginary magnetic current density, to make the equations symmetric without introducing complexity. These currents are excited inside the materials.

Maxwell's equations also require constitutive relations between field components to form complete equations. These are given by:

$$\boldsymbol{D} = \varepsilon \boldsymbol{E},$$
$$\boldsymbol{B} = \mu \boldsymbol{H},$$
$$\boldsymbol{J} = \sigma \boldsymbol{E}, \qquad (2.20)$$
$$\boldsymbol{J}^* = \sigma^* \boldsymbol{H}.$$

where ε, μ, σ, σ^* are the permittivity, permeability, electrical conductivity and magnetic resistivity of the material, respectively. They are scalars for isotropic media and tensors for anisotropic media. For homogeneous media, they are constant, while for inhomogeneous media, they vary with spatial location. Here we take the simplest case, assuming that the space under study is passive and parameters of the medium also do not vary in time and space.

In a rectangular coordinate system, $\boldsymbol{E}$ and $\boldsymbol{H}$ can be decomposed as follows $\boldsymbol{E} = E_x \boldsymbol{a}_x + E_y \boldsymbol{a}_y + E_z \boldsymbol{a}_z$, $\boldsymbol{H} = H_x \boldsymbol{a}_x + H_y \boldsymbol{a}_y + H_z \boldsymbol{a}_z$. The two curl equations in Maxwell's equations can be expressed as six scalar equations:

$$\frac{H_z}{\partial y} - \frac{H_y}{\partial z} = \varepsilon \frac{E_x}{\partial t} + \sigma E_x, \tag{2.21a}$$

$$\frac{H_x}{\partial z} - \frac{H_z}{\partial x} = \varepsilon \frac{E_y}{\partial t} + \sigma E_y, \tag{2.21b}$$

$$\frac{H_y}{\partial x} - \frac{H_x}{\partial y} = \varepsilon \frac{E_z}{\partial t} + \sigma E_z, \tag{2.21c}$$

$$\frac{E_z}{\partial y} - \frac{E_y}{\partial z} = -\mu \frac{H_x}{\partial t} - \sigma^* H_x, \tag{2.21d}$$

$$\frac{E_x}{\partial z} - \frac{E_z}{\partial x} = -\mu \frac{H_y}{\partial t} - \sigma^* H_y, \tag{2.21e}$$

$$\frac{E_y}{\partial x} - \frac{E_x}{\partial y} = -\mu \frac{H_z}{\partial t} - \sigma^* H_z. \tag{2.21f}$$

To show how FDTD solves these equations iteratively, these equations are next represented in terms of finite difference by using the Yee's algorithm [12]. In 1996, K. S. Yee first expressed the Maxwell's six scalar equations by using the FDTD method. In order to discretize each electromagnetic field component in the above six scalar equations in space and time, the 3-D space is divided into numerous small cubic cells, and the six components of the electromagnetic field are configured at special positions on each cubic cell, known as Yee cells, as shown in Figure 2.4. Spatially, E_x, E_y and E_z are discretized at each edge of every Yee cell and H_x, H_y and H_z are discretized at the center position of each face of every Yee cell. Each electric field component is surrounded by four magnetic field components, and similarly, each magnetic field component is surrounded by four electric field components. The sampling time of the electric field component is set to be an integer time step, and the magnetic field component is sampled at a half-integer time step. That is, sampling of $\boldsymbol{E}$ and $\boldsymbol{H}$ is done alternately on the time axis and the electric and magnetic components always differ by half a grid step in either direction.

The sampled electric and magnetic field components are written as $E_x^{n+1}(i + \frac{1}{2}, j, k)$, $E_y^{n+1}(i, j + \frac{1}{2}, k)$, $E_z^{n+1}(i, j, k + \frac{1}{2})$, $H_x^{n+\frac{1}{2}}(i + \frac{1}{2}, j, k)$, $H_y^{n+\frac{1}{2}}(i, j + \frac{1}{2}, k)$, $H_z^{n+\frac{1}{2}}(i, j, k + \frac{1}{2})$, respectively. The spatial coordinates of each grid point can be expressed as $(i, j, k) = (i\Delta x, j\Delta y, k\Delta z)$, among which Δx, Δy, Δz denote the grid steps of the Yee cell along the three coordinate axes, respectively, and i, j, k denote the number of spatial steps in respective directions. Therefore, the function at any space and time can be represented by

$$f^{t_n}(i, j, k) = f(x, y, z, t_n) = f(i\Delta x, j\Delta y, k\Delta z, n\Delta t), \tag{2.22}$$

where Δt denotes the time step and n denotes the number of the time step.

The central difference approximation with second-order accuracy is used both in the temporal and spatial domain to substitute the space and time derivatives in the six scalar equations. The first partial derivative for each space component, evaluated at time

$t_n = n\Delta t$, is given by:

$$\frac{\partial f^{t_n}(u)}{\partial u} \approx \frac{f^{t_n}(u + \frac{\Delta u}{2}) - f^{t_n}(u - \frac{\Delta u}{2})}{\Delta u} + o(\Delta u^2) \quad (u = x, y, z), \tag{2.23}$$

where Δu is the step interval. Then, the first partial derivative with respect to time for a particular space point is given by:

$$\frac{\partial f^{t_n}(u)}{\partial t} \approx \frac{f^{t_{n+1/2}}(u) - f^{t_{n-1/2}}(u)}{\Delta t} + o(\Delta t^2). \tag{2.24}$$
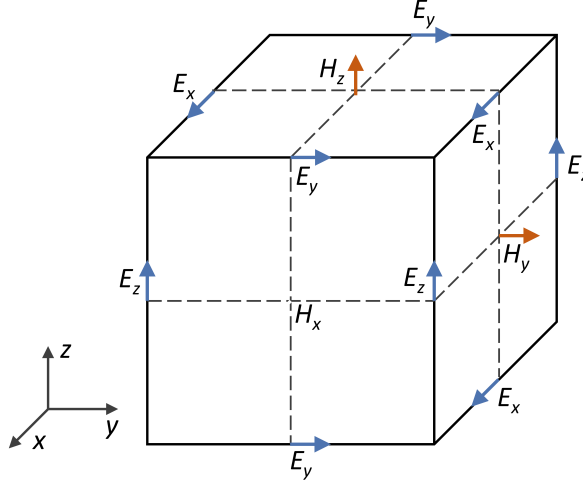

Figure 2.4: Schematic of electric and magnetic components in Yee cell.

The time and space derivatives of the electromagnetic field in the six scalar equations of Equation 2.21(a)-(f) are approximated by Equation 2.23 and Equation 2.24 to obtain the finite-difference form for each electromagnetic field component, as

$$\begin{aligned}
E_x^{n+1}(i + \frac{1}{2}, j, k) =& C(i + \frac{1}{2}, j, k) E_x^n(i + \frac{1}{2}, j, k) \\
&+ D(i + \frac{1}{2}, j, k)\left(\frac{H_z^{n+\frac{1}{2}}(i + \frac{1}{2}, j + \frac{1}{2}, k) - H_z^{n+\frac{1}{2}}(i + \frac{1}{2}, j - \frac{1}{2}, k)}{\Delta y}\right) \\
&- D(i + \frac{1}{2}, j, k)\left(\frac{H_y^{n+\frac{1}{2}}(i + \frac{1}{2}, j, k + \frac{1}{2}) - H_y^{n+\frac{1}{2}}(i + \frac{1}{2}, j, k - \frac{1}{2})}{\Delta z}\right),
\end{aligned} \tag{2.25}$$

among which

$$C(i, j, k) = \frac{2\varepsilon(i, j, k) - \sigma(j, j, k)\Delta t}{2\varepsilon(i, j, k) + \sigma(j, j, k)\Delta t}, \qquad C^*(i, j, k) = \frac{2\mu(i, j, k) - \sigma^*(j, j, k)\Delta t}{2\mu(i, j, k) + \sigma^*(j, j, k)\Delta t},$$

$$D(i, j, k) = \frac{2\Delta t}{2\varepsilon(i, j, k) + \sigma(j, j, k)\Delta t}, \qquad D^*(i, j, k) = \frac{2\Delta t}{2\mu(i, j, k) + \sigma^*(j, j, k)\Delta t}.$$

The finite difference equations corresponding to Equation 2.21(b) and (c), respectively, can be similarly constructed.

$$
\begin{aligned}
H_x^{n+\frac{1}{2}}(i, j+\tfrac{1}{2}, k+\tfrac{1}{2}) = {}& C^*(i, j+\tfrac{1}{2}, k+\tfrac{1}{2}) H_x^{n-\frac{1}{2}}(i, j+\tfrac{1}{2}, k+\tfrac{1}{2}) \\
& - D^*(i, j+\tfrac{1}{2}, k+\tfrac{1}{2}) \left(\frac{E_z^n(i, j+1, k+\tfrac{1}{2}) - E_z^n(i, j, k+\tfrac{1}{2})}{\Delta y} \right) \\
& + D^*(i, j+\tfrac{1}{2}, k+\tfrac{1}{2}) \left(\frac{E_y^n(i, j+\tfrac{1}{2}, k+1) - E_y^n(i, j+\tfrac{1}{2}, k)}{\Delta z} \right).
\end{aligned}
\tag{2.26}
$$

The finite difference equations corresponding to Equation 2.21(e) and (f), respectively, can be similarly constructed.

The above FDTD equations indicate that the electric (magnetic) field at any time depends on the electric (magnetic) field of the previous time step, the adjacent magnetic (electric) field of the first half time step on the surface orthogonal to this electric (magnetic) field, and the electromagnetic parameters of the medium. The FDTD method takes the electromagnetic problem as the initial value problem, the electromagnetic field in the simulation region is zero at the initial moment. Under the source excitation, the resulting equation is solved in a leapfrog manner. In other words, the electric field is computed at a given instant in time, then the magnetic field is computed at the next instant in time, and this process is gradually advanced in time until convergence. To achieve convergence of the electromagnetic field, the time step must be chosen sufficiently small.

2.3.2. THE FDTD SOLVER

Benefiting from the rapid development of computing power, commercial simulation software has developed very rapidly, and simulation packages based on the FDTD method have been made. The Lumerical FDTD Solution of Ansys company is the main numerical simulation software used in this dissertation, which can quickly and accurately solve the 2-D and 3-D electromagnetic field Maxwell's equations.

In FDTD simulation, difference equations are used to calculate spatial electromagnetic field distribution, so the space needs to be divided into grids, like the Yee cells do. The size of the grid directly determines the accuracy of the numerical calculation and the running time of the system. In general, the mesh size should be smaller than $\lambda/10$, and for small irregular structural elements such as tips, slope, holes, and so on, a smaller mesh size is necessary to obtain accurate results. It is computationally unfeasible to solve a scattering problem in infinite space, so it is necessary to introduce boundary conditions to calculate the distribution of electromagnetic field in a bounded part of space. It is worth mentioning that perfectly matched layer (PML) can simulate the propagation of electromagnetic waves to infinity, which corresponds to the actual situation and saves computing resources. In addition to the widely used PML, there are also Bloch boundary, symmetric-antisymmetric boundary, periodic boundary, etc. Different boundary conditions need to be used for different structures and incident field conditions. The selected boundary condition restricts the EMF simulation region to be contained by the boundary and this divides the whole space into the inner space where the spatial field needs to be calculated and the outer space where the spatial field does not need to be calculated.

In the Lumerical FDTD solver, the geometrical characteristics and refractive index of the structure can be set using a library with structure and material parameter values to establish the model. The initial value of the electromagnetic field is given by adding appropriate light sources. These sources can be the built-in sources of the solver, such as a dipole or optical fields like plane wave, Gaussian beam, etc. and could also be generated by a customized script. The desired output field can be extracted from the monitors that one can choose, which include the electric and magnetic components, and even the Poynting vector and power if needed.

2.4. FAR-FIELD OF SCATTERING FIELD

In the previous sections, we discussed the generation of the incident field, as well as the acquisition of the scattering field through numerical simulation methods. The final step is propagating the scattering near field into the far-field for further analysis.

Now, let us consider a plane wave encountering a lens with z as its optical axis, and finite extension in transverse xy plane. Under the assumption of the thin lens and paraxial approximation, the transmittance function of this lens can be characterized by a parabolic phase delay to the incident wavefront. The finite extent of the lens can be treated by a pupil function $P(x, y)$ related to the lens defined as

$$P(x, y) = \begin{cases} 1, & \text{inside the lens aperture,} \\ 0, & \text{else.} \end{cases} \quad (2.27)$$

The transformation function of the lens with focal distance f is represented by:

$$t(x, y) = P(x, y) \exp\left[-i\frac{k}{2f}(x^2 + y^2)\right]. \quad (2.28)$$

Assume that the light incident on the lens is denoted as $U(x, y, 0)$, and the light behind the lens is denoted as $U'(x, y, 0)$. The field distribution of $U'(x, y, 0)$ is given by

$$U'(x, y, 0) = U(x, y, 0)P(x, y) \exp\left[-i\frac{k}{2f}(x^2 + y^2)\right]. \quad (2.29)$$

We use the Fresnel diffraction integral to get the field distribution in the back focal plane $(z = f)$. If the back focal plane coordinates are (x_f, y_f), the result is given by:

$$U(x_f, y_f, f) = \frac{\exp(ikf)\exp\left[i\frac{k}{2f}(x_f^2 + y_f^2)\right]}{i\lambda f}$$
$$\times \iint\limits_{-\infty}^{\infty} U'(x, y, 0) \exp\left[i\frac{k}{2f}(x^2 + y^2)\right] \exp\left[-i\frac{2\pi}{\lambda f}(x_f x + y_f y)\right] dx dy. \quad (2.30)$$

Inserting the Equation 2.29 into Equation 2.30, gives

$$U(x_f, y_f, f) = \frac{\exp\left[i\frac{k}{2f}(x_f^2 + y_f^2)\right]}{i\lambda f}$$

$$\times \iint\limits_{-\infty}^{\infty} U(x, y, 0)P(x, y)\exp[-i2\pi(f_x x + f_y y)]dxdy \qquad (2.31)$$

$$= \frac{\exp\left[i\frac{k}{2f}(x_f^2 + y_f^2)\right]}{i\lambda f}\mathscr{F}\{U(x, y, 0)P(x, y)\}(f_x, f_y),$$

where $\mathscr{F}(\cdot)$ denotes the 2D Fourier transform and the spatial frequencies are $f_x = x_f/\lambda f$, $f_y = y_f/\lambda f$ (f is the focal length), and the constant phase change given by the factor $\exp(ikf)$ is omitted. Equation 2.31 shows that the output complex amplitude $U(x_f, y_f, f)$ is the Fraunhofer diffraction pattern of the input complex amplitude $U(x, y, 0)$ within the aperture enclosed by the lens ($P(x, y)$). Although the distance of the observation plane is equal to the focal length of the lens, which is much shorter than the typical distance required for Fraunhofer diffraction, we can still observe the Fraunhofer diffraction pattern at the back focal plane due to the presence of the lens. Because of the presence of the quadratic phase factor in front of the integral sign, the relationship between the input plane and the back focal plane is not an exact Fourier transform, in other words, there is a phase distortion between the field distribution in the back focal plane of a lens and its frequency spectrum.

The Fresnel propagation of waves can also be described by the angular spectrum theory. Considering a wave field $U(x, y, z)$ propagating in the z-direction. Let $z = -d(d > 0)$, the 2D Fourier representation of $U(x, y, -d)$ is

$$U(x, y, -d) = \iint\limits_{-\infty}^{\infty} A(f_x, f_y, -d)\exp[i2\pi(xf_x + yf_y)]df_xdf_y, \qquad (2.32)$$

where

$$A(f_x, f_y, -d) = \iint\limits_{-\infty}^{\infty} U(x, y, -d)\exp[-i2\pi(xf_x + yf_y)]dxdy, \qquad (2.33)$$

is called the angular spectrum of $U(x, y, -d)$. According to angular spectrum theory, we can assign a physical meaning to the above Equation 2.32. The complex exponential function $\exp[i2\pi(xf_x + yf_y)]$ can be regarded as a plane wave with the propagation direction ($\alpha = \lambda f_x, \beta = \lambda f_y, \gamma = \sqrt{1 - \alpha^2 - \beta^2}$) and $A(f_x, f_y, -d)$ is the complex amplitude in the plane $z = -d$ of this plane wave. In this theory, any wave can be represented as a superposition of plane waves propagating at different angles with different wavevectors and amplitudes.

We can see that the angular spectrum of the field is the Fourier transform of this field, so this field can also be expressed as the inverse Fourier transform of the angular spectrum. Let us assume that $U(x, y, 0)$ and $U(x_f, y_f, f)$ still represent the field incident on the lens and on the back focal plane respectively. The angular spectrum of $U(x, y, 0)$ is given by

$$A(f_x, f_y, 0) = \iint\limits_{-\infty}^{\infty} U(x, y, 0) \exp\left[-i2\pi(xf_x + yf_y)\right] dx dy, \tag{2.34}$$

and the Fourier representation of $U(x, y, 0)$ is given by

$$U(x, y, 0) = \iint\limits_{-\infty}^{\infty} A(f_x, f_y, 0) \exp\left[i2\pi(xf_x + yf_y)\right] df_x df_y. \tag{2.35}$$

In addition, $U(x, y, 0)$ must satisfy the Helmholtz equation at all points without sources, namely

$$\nabla^2 U(x, y, 0) + k^2 U(x, y, 0) = 0. \tag{2.36}$$

Substitution of Equation 2.35 into Equation 2.36 yields:

$$\iint\limits_{-\infty}^{\infty} \left[\frac{\partial^2}{\partial z^2} A(f_X, f_Y, 0) + (k^2 - 4\pi^2(f_x^2 - f_y^2)) A(f_x, f_y, 0) \right] \exp\left\{i2\pi(xf_x + yf_y)\right\} df_x df_y = 0, \tag{2.37}$$

this is true for all waves only if the integrand is zero:

$$\frac{\partial^2}{\partial z^2} A(f_x, f_y, 0) + (k^2 - 4\pi^2(f_x^2 - f_y^2)) A(f_X, f_Y, 0) = 0. \tag{2.38}$$

The solution which corresponds to a wave propagating in the positive z-direction is:

$$A(f_x, f_y, 0) = A(f_x, f_y, -d) \exp\left\{i(-d)\sqrt{k^2 - 4\pi^2(f_x^2 - f_y^2)}\right\}. \tag{2.39}$$

The above equation shows that the propagation of waves only change the relative phase to the angular spectrum, and the function of $\exp\left\{i(-d)\sqrt{k^2 - 4\pi^2(f_x^2 - f_y^2)}\right\}$ can be regarded as the propagator of the diffraction system.

In the Fresnel or paraxial approximation, the propagator in Equation 2.39 is given by

$$\exp\left\{i(-d)\sqrt{k^2 - 4\pi^2(f_x^2 - f_y^2)}\right\} \approx \exp\left\{ik(-d)\exp\left[-i\pi\lambda(-d)(f_x^2 + f_y^2)\right]\right\}, \tag{2.40}$$

and the relationship between $A(f_x, f_y, -d)$, $A(f_X, f_Y, 0)$ becomes

$$A(f_x, f_y, 0) = A(f_x, f_y, -d) \exp\left(ik(-d)\right) \exp\left[-i\pi\lambda(-d)(f_x^2 + f_y^2)\right]. \tag{2.41}$$

If the extent of the field $U(x, y, 0)$ is smaller than the extent of $P(x, y)$, Equation 2.31 can be written as

$$U(x_f, y_f, f) = \frac{\exp\left[i\frac{k}{2f}(x_f^2 + y_f^2)\right]}{i\lambda f} A(f_x, f_y, 0), \tag{2.42}$$

or, using Equation 2.41

$$U(x_f, y_f, f) = \frac{\exp\left[i\frac{k}{2f}(1 - \frac{d}{f})(u^2 + v^2)\right]}{i\lambda f} A(f_x, f_y, -d). \tag{2.43}$$

Thus, for an input field placed at a distance d before a lens, the field at the back focal plane of the lens is given by the Fourier transform of the initial field multiplied by a quadratic phase factor that depends on the distance d. With $d = f$, the above equation becomes

$$U(x_f, y_f, f) = A(f_z, f_y, -f).$$

(2.44)

Obviously, $z = f$ makes the phase distortion disappear, and the relationship between the front and back focal plane becomes the exact Fourier transform. This formula is valid to describe the input-output relation for the lens.

To CFS, the same objective lens is used to focus the incident light onto the structure and collect the scattering light from the structure. The presence of the lens allows CFS to collect all the scattering light which fits in the numerical aperture of the lens, and conveniently perform Fourier analysis on the back focal plane without being affected by the quadratic phase factor. After obtaining the near-field data from the Lumerical FDTD solver, we can further perform a near-to-far transformation by the analytical methods, both the Fresnel diffraction integral and the Fast Fourier transform method are considered.

In this chapter, we present the semi-analytical research method that we have considered to investigate the scattering problem between structured light field and the object. We will carry out our researches in the following chapters according to these concepts.

REFERENCES

[1]   Z. Man, **X. Dou**, and H. P. Urbach. "The evolutions of spin density and energy flux of strongly focused standard full Poincaré beams". In: *Optics Communications* 458 (2020), p. 124790.

[2]   E. Wolf. "Electromagnetic diffraction in optical systems-I. An integral representation of the image field". In: *Proceedings of the Royal Society of London. Series A. Mathematical and Physical Sciences* 253.1274 (1959), pp. 349–357.

[3]   B. Richards and E. Wolf. "Electromagnetic diffraction in optical systems, II. Structure of the image field in an aplanatic system". In: *Proceedings of the Royal Society of London. Series A. Mathematical and Physical Sciences* 253.1274 (1959), pp. 358–379.

[4]   E. Wolf and Y. Li. "Conditions for the validity of the Debye integral representation of focused fields". In: *Optics Communications* 39.4 (1981), pp. 205–210.

[5]   M. Gu. *Advanced optical imaging theory*. Vol. 75. Springer Science & Business Media, 2000.

[6]   J. Lin, O. Rodrıguez-Herrera, F. Kenny, D. Lara, and J. Dainty. "Fast vectorial calculation of the volumetric focused field distribution by using a three-dimensional Fourier transform". In: *Optics express* 20.2 (2012), pp. 1060–1069.

[7]   A. S. van de Nes, L. Billy, S. F. Pereira, and J. J. M. Braat. "Calculation of the vectorial field distribution in a stratified focal region of a high numerical aperture imaging system". In: *Optics Express* 12.7 (2004), pp. 1281–1293.

[8]   C. Prajapati. "Numerical study of spin–orbit interaction of light in nonparaxial focusing of Gaussian beams". In: *Optik* 228 (2021), p. 166199.

2

[9]   M. Moharam and T. Gaylord. "Rigorous coupled-wave analysis of planar-grating diffraction". In: *JOSA* 71.7 (1981), pp. 811–818.

[10]   P. Monk *et al. Finite element methods for Maxwell's equations.* Oxford University Press, 2003.

[11]   A. Taflove, S. C. Hagness, and M. Piket-May. "Computational electromagnetics: the finite-difference time-domain method". In: *The Electrical Engineering Handbook* 3 (2005), pp. 629–670.

[12]   K. Yee. "Numerical solution of initial boundary value problems involving Maxwell's equations in isotropic media". In: *IEEE Transactions on antennas and propagation* 14.3 (1966), pp. 302–307.

3

CONTROL THE PROPERTIES OF A TIGHTLY FOCUSED FIELD

In this chapter, we show that elongating a tightly focused field in the direction perpendicular to the optical axis is possible. We demonstrate our approach by specially shaping the Pancharactnam–Berry (PB) phase. The analytical formulae required to calculate the vectors and energy flux of the three-dimensional electromagnetic fields near the focus of an aplanatic optical system are derived by using the Richards and Wolf vectorial diffraction methods. Calculations reveal that the transverse enhancement is controllable and depend on the phase index in the PB phase, thereby giving rise to a focus with tunable length and sub-wavelength width in the focal plane.

3.1. Introduction

For a sensible interpretation of the image formation and information retrieval, it is necessary to have a good understanding of the field used for illumination of the sample. The ability to generate light fields with almost any desired structure has renewed interest in generating and analysing optical fields with new shapes. Novel techniques involving the manipulation and structuring of light have been recently introduced in the field of optical metrology, with the goal of finding new solutions to old problems.

In view of the practical needs of CFS, it is common to use a focused light spot of the order of a wavelength as the measurement probe. A focused light spot is easy to generate, but is not always the optimal probe. Since the focused light spot can only illuminate a small area, in order to cover all the areas of interest, we must scan this region. For the grating structure commonly encountered in IC measurement, one of its axes remains unchanged. In this situation, using a larger-sized line shape focused field for detection would undoubtedly save a lot of time. To date, however, attempts to target transverse elongation of the focus in the focal plane have not been undertaken, which is highly desired in practical applications. In this chapter, we demonstrate an new approach by specially shaping the PB phase to elongate a tightly focused field in the direction perpendicular to the optical axis.

3.2. The method of PB phase shaping

In this section, we propose a method to elongate the tightly focused field in the direction perpendicular to the optical axis assisted by PB-phase shaping. The expressions for calculating the electromagnetic strength vectors and energy flux near focus are derived using the vectorial diffraction methods of Richards and Wolf. Based on an analytical model, the transverse enhancement was found only to depend on the phase index of the PB phase. As a result, a focus with controllable length and subwavelength width in the focal plane is achieved. Furthermore, the corresponding Poynting vector distributions are studied in detail to provide a better understanding of the transverse enhancement of focusing.

To give a clear understanding of the PB phases, a brief analysis concerning its origin is necessary. Because PB phases are related to variations in the SoPs, we assume there are two polarization states in terms of an initial one E_1 and a final one E_2. For simplicity and without loss of generality, E_1 corresponds to a linear polarization with an orientation with respect to the x-axis denoted by c. Hence, it may be represented as a two-dimensional Jones vector such that

$$E_1 = \cos c\, \hat{\mathbf{e}}_x + \sin c\, \hat{\mathbf{e}}_y = \frac{1}{\sqrt{2}} \left[\exp\left(-ic\right)\hat{\mathbf{e}}_l + \exp\left(ic\right)\hat{\mathbf{e}}_r \right], \tag{3.1}$$

where $\hat{\mathbf{e}}_x$ and $\hat{\mathbf{e}}_y$ denote unit vectors directed along the x- and y-axes, respectively, of the linear polarization; similarly, $\hat{\mathbf{e}}_l$ and $\hat{\mathbf{e}}_r$ denote unit vectors of left-handed (LH) and right-handed (RH) circular polarization. For arbitrary light beams with a homogeneously linear SoP, the two components expressed in terms of LH and RH circular vibrations have opposite initial phases, the value of which determines the orientation of the linear vibration. After a polarization transformation, if the PB phases acquired by the LH and

RH circular components are, respectively, ε_l and ε_r, the resultant final polarization state $\boldsymbol{E}_2$ is then expressed as [2]

$$
\begin{aligned}
\boldsymbol{E}_2 &= \frac{1}{\sqrt{2}} \left\{ \exp\left[i\left(\varepsilon_l - c\right)\right]\hat{\mathbf{e}}_l + \exp\left[i\left(\varepsilon_r + c\right)\right]\hat{\mathbf{e}}_r \right\} \\
&= e^{\left(i\frac{\varepsilon_r + \varepsilon_l}{2}\right)} \left\{ \left[\cos\left(\frac{\varepsilon_r - \varepsilon_l}{2} + c\right)\right]\hat{\mathbf{e}}_x + \left[\sin\left(\frac{\varepsilon_r - \varepsilon_l}{2} + c\right)\right]\hat{\mathbf{e}}_y \right\}.
\end{aligned}
\tag{3.2}
$$

Unfortunately, a dynamic phase appears in Equation 3.2, indicating a phase retardation of $(\varepsilon_r + \varepsilon_l)/2$ compared with that in Equation 3.1. However, if we choose $\varepsilon_r = -\varepsilon_l = \varepsilon_e$, this phase disappears. The PB phase ε_e as an intrinsic optical degree of freedom may have arbitrary distributions in theory, and thus provides a powerful means to manipulate light. Indeed, great success has been achieved in enabling transformations from states $\boldsymbol{E}_1$ to $\boldsymbol{E}_2$, such as wave plates and subwavelength gratings as well as specially designed optical systems [3–6].

Numerous practical applications ranging from microscopy to data storage as well as micromanipulation require tight focusing. Different from previous results suggesting tightly focused fields permit a significant enhancement in the direction along the optical axis, a tunable enhancement in the direction perpendicular to the latter is found also to be possible when setting

$$
\varepsilon_e = 2\pi v (r\sin\varphi/r_0)^3,
\tag{3.3}
$$

where v is the phase index, r and φ denote the polar radius and azimuthal angle, respectively, and r_0 is the radius of the input field. In this case, ε_e is a function of both r and φ; thus, the resultant PB phase get a space-variant distribution. Referring to the Equation 2.7 in Chapter 2, the corresponding three-dimensional electric field near the focus can be given as

$$
\boldsymbol{E}_{\text{out}}(\rho,\,\phi,\,z) = \frac{-ikf}{2\pi} \int_0^{2\pi}\int_0^{\alpha} \sqrt{\cos\theta}\, l_{\text{in}}(\theta)\sin\theta\, \boldsymbol{M}_E
\tag{3.4}
$$
$$
\times\, e^{\{ik[-\rho\sin\theta\cos(\varphi-\phi)+z\cos\theta]\}}\, d\varphi d\theta,
$$

where (ρ, ϕ, z) are the cylindrical coordinates of the image space; k and f denote the wave number and focal length, respectively, θ is the tangential angle with respect to the z-axis, $\alpha = \arcsin(\text{NA}/n)$ with NA the numerical aperture of the focusing objective lens and n the refractive index in the image space, which we take as 0.95 and 1, respectively. The function $l_{\text{in}}(\theta)$ represents the complex amplitude distribution of the incident beam, having the form [7]

$$
l_{\text{in}}(\theta) = \exp\left[-\beta^2\left(\frac{\sin\theta}{\sin\alpha}\right)^2\right] J_1\left(2\beta\frac{\sin\theta}{\sin\alpha}\right),
\tag{3.5}
$$

where β is the ratio of the pupil radius to the beam waist, which we choose as 1 in our configuration; $J_1(x)$ is the first kind of first order Bessel function. In Equation 3.4, $\boldsymbol{M}_E$ represents the electric field polarization vector in the image space contributed by the input polarization and its explicit forms is

$$\boldsymbol{M}_E = M_E^x \hat{\mathbf{e}}_x + M_E^y \hat{\mathbf{e}}_y + M_E^z \hat{\mathbf{e}}_z \tag{3.6}$$

$$M_E^x = \sin\left[\varphi - 2\pi v\left(\frac{\sin\theta\sin\varphi}{\sin\alpha}\right)^3 - c\right]\sin\varphi \tag{3.7a}$$
$$+ \cos\left[2\pi v\left(\frac{\sin\theta\sin\varphi}{\sin\alpha}\right)^3 + c - \varphi\right]\cos\theta\cos\varphi,$$

$$M_E^y = -\sin\left[\varphi - 2\pi v\left(\frac{\sin\theta\sin\varphi}{\sin\alpha}\right)^3 - c\right]\cos\varphi \tag{3.7b}$$
$$+ \cos\left[2\pi v\left(\frac{\sin\theta\sin\varphi}{\sin\alpha}\right)^3 + c - \varphi\right]\cos\theta\sin\varphi,$$

$$M_E^z = \cos\left[2\pi v\left(\frac{\sin\theta\sin\varphi}{\sin\alpha}\right)^3 + c - \varphi\right]\sin\theta. \tag{3.7c}$$

Next, we analyze the tightly focused electric field distributions based on Equations 3.4-3.7. As examples, we explore the focal behaviors of three different optical fields with $(v, c) = (0, \pi/2)(1, \pi/2)$ and $(20, \pi/2)$; the corresponding input polarization and intensity distributions are depicted in Figure 3.1, with the focusing conditions mentioned above. For $(v, c) = (0, \pi/2)$ [Figure 3.1(a)], the beam is linearly polarized with spatially invariant SoPs. Its orientation is parallel to the y-axis direction. However, for a nonzero value of v, the beam has a spatially varying SoP [Figure 3.1(b) and (c)], with the orientation of the local vibration varying along the y-axis but has no change in the direction perpendicular to it.
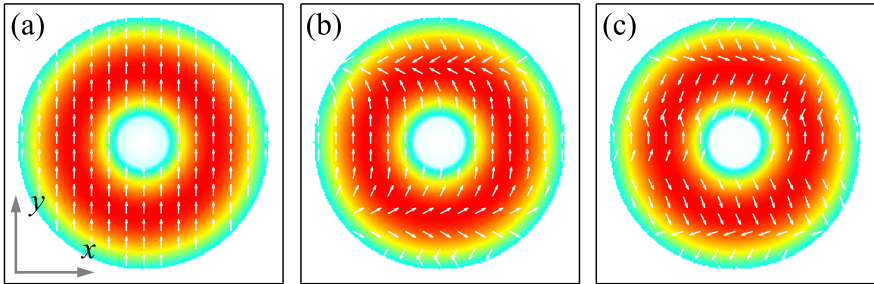

Figure 3.1: Polarization and intensity distributions of three different pupil fields with $(v, c) = (0, \pi/2), (1, \pi/2),$ and $(20, \pi/2)$

3.3. THE CONTROLLABLE TRANSVERSE ENHANCEMENT

The corresponding normalized electric field distributions in the focal plane are depicted in Figure 3.2. Apparently, the y-polarized component [Figure 3.2(b), (f), and (g)], is much larger than the x-component [Figure 3.2(a), (e), (i)] and the z-component [Figure 3.2(c), (g), (k)] is much bigger and dominates the total field for all the three cases. Specifically,
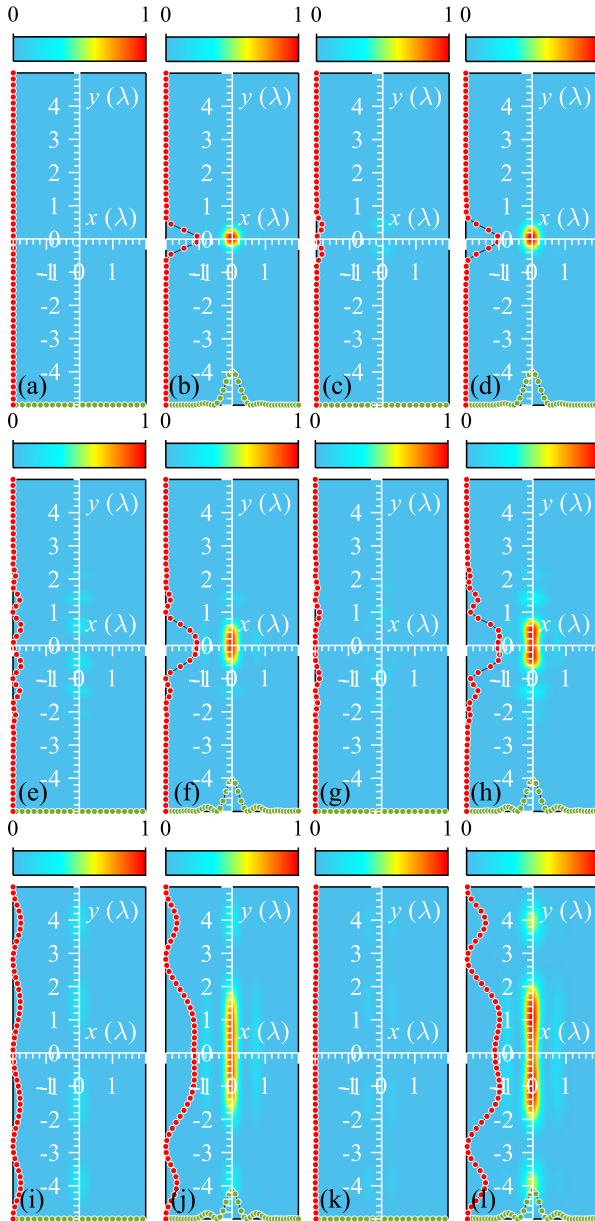
Figure 3.2: Electric field intensity distributions of tightly focused pupil fields with $(v, c) =$ $(0, \pi/2), (1, \pi/2)$, and $(20, \pi/2)$ (upper, middle, and lower rows, respectively). From left to right, the four columns show the x-, y-, and z-polarized components and the total electric field. The insets for each image depict the normalized intensity profiles along the x (green curve) and y axes (red curve), respectively. All intensity distributions are normalized by the maximum intensity in the focal plane for each input light mode.

almost no field is found for the x-polarized component [Figure 3.2(a)] of the linearly polarized input beam. However, the on-axis quasi-circular intensity distribution for the y-polarized component [Figure 3.2(b)] and twin focal spots located along the y-axis for the z-polarized component [Figure 3.2(c)] play a dominant role, resulting in an elliptically shaped pattern for the total field [Figure 3.2(d)] with the major-axis direction being in accordance with the orientation of the input field [Figure 3.1(a)]. Most importantly, all three electric field components [Figure 3.2(e)–(g) and 3.2(i)–(k)] permit a significant transverse enhancement along the y-axis with increasing v, resulting in a tunable length of focus in the direction perpendicular to the optical axis for the total field [Figure 3.2(h) and (l)] accompanied with the increase of side lobes. Such fascinating focal behaviors are attributed to the one-dimensional manipulation of the input SoPs. As a result, a transverse elongation of focus is also possible, complementing the well-known long depth of focus. Moreover, the long foci exhibit high uniformity as they are intensity profiles with near-flat tops; see insets in Figure 3.2(h) and (l).
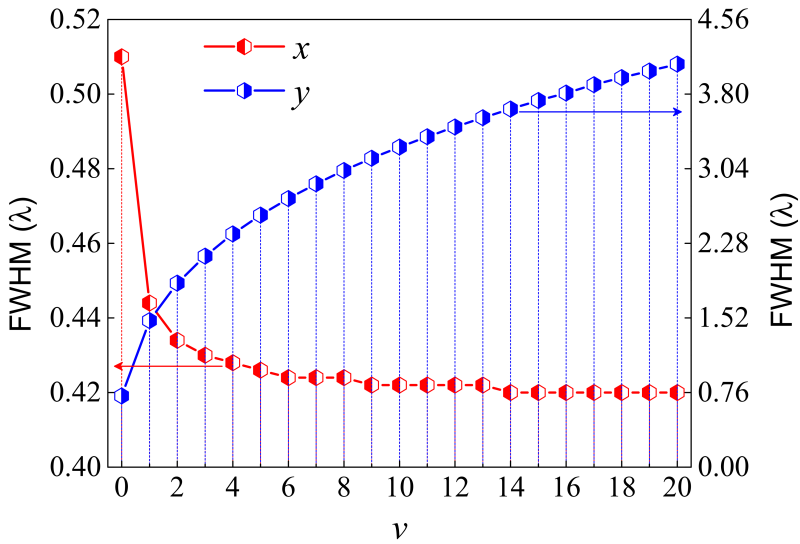

Figure 3.3: Full width at half-maximum (FWHM) values of the electric field intensity along the x- and y-axes versus the phase index v with NA = 0.95.

The value of the phase index v in the specially designed PB phase ε affects significantly the transverse enhancement of the focus, as seen in Figure 3.2. To detail and quantify the relationship between v and the length and width of the focus, Figure 3.3 shows the full width at half-maximum (FWHM) values along both the x- and y-axes versus v; the FWHW/ values are from left to right for $v=0, 1, \ldots, 20$, respectively: 0.510, 0.444, 0.434, 0.430, 0.428, 0.426, 0.424, 0.424, 0.424, 0.422, 0.422, 0.422, 0.422, 0.422, 0.420, 0.420, 0.420, 0.420, 0.420, 0.420, 0.420 along the x-axis and 0.726, 1.492, 1.872, 2.150, 2.376, 2.568, 2.736, 2.886, 3.022, 3.146, 3.260, 3.366, 3.466, 3.560, 3.648, 3.734, 3.810, 3.896, 3.968, 4.036, and 4.106 along the y-axis. Obviously, a linearly polarized beam may be used to create an

elliptical spot under tight focusing conditions because this focal field has different FWHM values along the x- and y-directions. Furthermore, with increasing v, the FWHM values along the x and y-axis decrease and increase, respectively, which are smaller than the diffraction limit for this focusing lens $\lambda/(2NA) = 0.526$ and different from the line-focusing of a cylindrical lens. Therefore, a tunable transverse enhancement of focusing controlled by phase index v is achieved.

3.4. THE ENERGY FLUX OF THE FOCUSING FIELD

To provide a better understanding of the transverse enhancement of focusing assisted by the shaping of the PB phase, its energy flux needs to be evaluated. The corresponding three-dimensional magnetic field near focus may be similarly derived to the electric field [8],

$$\boldsymbol{H}_{\text{out}}(\rho,\ \phi,\ z) = \frac{-ikf\sqrt{\varepsilon/\mu}}{2\pi} \int\limits_{0}^{2\pi}\int\limits_{0}^{\alpha} \sqrt{\cos\theta}\, l_{\text{in}}(\theta)\sin\theta\, \boldsymbol{M}_H$$

$$\times\, e^{\{ik[-\rho\sin\theta\cos(\varphi-\phi)+z\cos\theta]\}}\, d\varphi d\theta, \tag{3.8}$$

and $\boldsymbol{M}_H$ represents the magnetic field polarization vector in the image space contributed by the input polarization and its explicit forms are

$$\boldsymbol{M}_H = M_H^x\hat{\mathbf{e}}_x + M_H^y\hat{\mathbf{e}}_y + M_H^z\hat{\mathbf{e}}_z, \tag{3.9}$$

$$M_H^x = -\cos\left[\varphi - 2\pi v\left(\frac{\sin\theta\sin\varphi}{\sin\alpha}\right)^3 - c\right]\sin\varphi \tag{3.10a}$$
$$+ \sin\left[\varphi - 2\pi v\left(\frac{\sin\theta\sin\varphi}{\sin\alpha}\right)^3 - c\right]\cos\theta\cos\varphi,$$

$$M_H^y = \cos\left[\varphi - 2\pi v\left(\frac{\sin\theta\sin\varphi}{\sin\alpha}\right)^3 - c\right]\cos\varphi \tag{3.10b}$$
$$+ \sin\left[\varphi - 2\pi v\left(\frac{\sin\theta\sin\varphi}{\sin\alpha}\right)^3 - c\right]\cos\theta\sin\varphi,$$

$$M_H^z = \sin\left[\varphi - 2\pi v\left(\frac{\sin\theta\sin\varphi}{\sin\alpha}\right)^3 - c\right]\sin\theta, \tag{3.10c}$$

where ε and μ denote, respectively, the dielectric constant and the magnetic permeability of the image space, and $\boldsymbol{M}_H$ is the magnetic field polarization vector in the image space. The magnetic fields distributions described by Equations 3.8-3.10c are evidently quite different from those describing the electric fields, Equations 3.4–3.7. In terms of the three-dimensional electric and magnetic fields, the energy current is determined by the time-averaged Poynting vector [8, 9],

$$\langle S \rangle \propto \frac{c}{8\pi}\Re\left(\boldsymbol{E}_{out} \times \boldsymbol{H}_{out}^*\right), \tag{3.11}$$

where asterisk represents the operation of complex conjugation. We can then calculate the energy flux based on Equation 3.11.
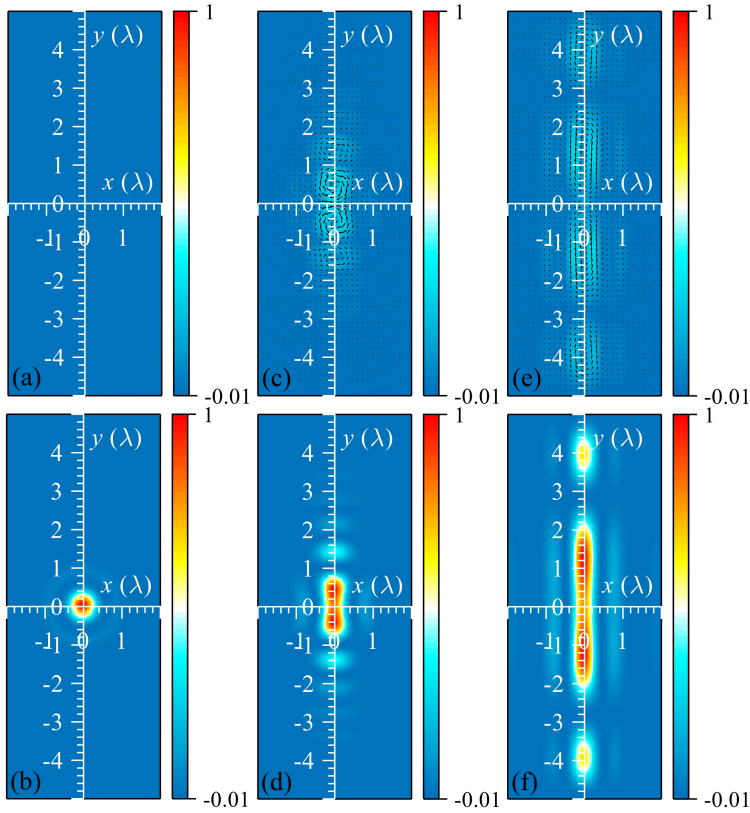

Figure 3.4: Energy flow distributions of the tightly focused input optical fields with $(v, c) = (0, \pi/2), (1, \pi/2)$, and $(20, \pi/2)$ (left, middle, and right columns, respectively). The upper and lower rows depict the transverse and longitudinal energy flows, respectively. The direction of the transverse energy flow is indicated by black arrows. All energy flow distributions are normalized by the maximum energy flow in the focal plane for each input light mode.

The Poynting vectors of the transverse and longitudinal components in the focal plane for the fields (Figure 3.2) are shown in Figure 3.4. No transverse energy flow is found in Figure 3.4(a). On the contrary, the circularly symmetric hot spot plays a dominate role in the longitudinal energy flow [see Figure 3.4(b)]. However, with nonzero v, multiple rings in the transverse energy flow along the y-axis are very clearly observed and exhibit circular [Figure 3.4(c)] and elliptical-shaped [Figure 3.4(e)] patterns for low and high values of v, respectively. Moreover, the circular symmetry of the longitudinal energy flow is broken, becoming a needle-shaped pattern for v equal to 1 [Figure 3.4(d)] and permits a further elongation along the y-axis with increasing v [Figure 3.4(f)].

3.5. CONLUSIONS

In conclusion, we have proposed a method to enhance the tightly focused field in the direction perpendicular to the optical axis assisted by a specially designed PB phase. The expression for calculating the electromagnetic and Poynting vector distributions near the focus has been derived using the Richards-Wolf vectorial diffraction methods. Physicaly, the focusing process can be treated as a simple Fourier transformation. By increasing the phase index v for the incident light field, the density of the polarization state increases along the y-direction, which corresponds to the density fluctuation of PB phase. That is equivalent to a higher spatial frequency of the incident light field along the y-direction. Consequently, the focus field, being the Fourier transform of the incident light field, is elongated along y-direction. Based on such analytical model, the transverse field enhancement depends only on the phase index v of the PB phase. As a result, a focus with controllable length and subwavelength width in the focal plane is achieved. Furthermore, the corresponding Poynting vector distributions are studied in detail. This work not only broadens the concept of structured light felds, but also has potential applications including optical micro- and nano-fabrication, micromanipulation.

REFERENCES

[1] Z. Man, **X. Dou**, and S. Fu. "Pancharatnam–Berry phase shaping for control of the transverse enhancement of focusing". In: *Optics Letters* 44.2 (2019), pp. 427–430.

[2] S. Liu, P. Li, and J. Zhao. "Pancharactnam-Berry phase used for realizing spin-dependent propagation and polarization measurement". In: *Complex Light and Optical Forces XII*. Vol. 10549. SPIE. 2018, pp. 147–154.

[3] Z. Bomzon, V. Kleiner, and E. Hasman. "Pancharatnam–Berry phase in space-variant polarization-state manipulations with subwavelength gratings". In: *Optics letters* 26.18 (2001), pp. 1424–1426.

[4] J. B. Mueller, N. A. Rubin, R. C. Devlin, B. Groever, and F. Capasso. "Metasurface polarization optics: independent phase control of arbitrary orthogonal states of polarization". In: *Physical review letters* 118.11 (2017), p. 113901.

[5] Q. Zhan. "Cylindrical vector beams: from mathematical concepts to applications". In: *Advances in Optics and Photonics* 1.1 (2009), pp. 1–57.

[6] X.-L. Wang, J. Chen, Y. Li, J. Ding, C.-S. Guo, H.-T. Wang, *et al.* "Optical orbital angular momentum from the curl of polarization". In: *Physical Review Letters* 105.25 (2010), p. 253602.

[7] K. S. Youngworth and T. G. Brown. "Focusing of high numerical aperture cylindrical-vector beams". In: *Optics Express* 7.2 (2000), pp. 77–87.

[8] B. Richards and E. Wolf. "Electromagnetic diffraction in optical systems, II. Structure of the image field in an aplanatic system". In: *Proceedings of the Royal Society of London. Series A. Mathematical and Physical Sciences* 253.1274 (1959), pp. 358–379.

[9] V. V. Kotlyar, A. A. Kovalev, and A. G. Nalimov. "Energy density and energy flux in the focus of an optical vortex: reverse flux of light energy". In: *Optics Letters* 43.12 (2018), pp. 2921–2924.

4

POLARIZATION-SENSITIVE SCATTERING FOR NANOSTRUCTURE DETECTION

In this chapter, we propose a far-field detection system to determine the steep side-wall angle (SWA) of a cliff-shaped step structure on a silicon substrate by combining a split detector with a scanning method. The far-field radiation field is asymmetric due to the scattering of the step structure, and further numerical analysis demonstrates the reliability of this far-field measurement method. In the simulations, two key variables, i.e., the polarization state and the focus position of the incident laser beam, are considered to explore their impacts. By scanning over the structure laterally and longitudinally with both TE and TM polarizations, polarization effects on the far-field occur. These effects show higher sensitivity to steep SWA variation for TM polarization than for TE. Furthermore, with a comprehensive longitudinal scanning analysis for the TM polarization case, a feasible focus interval can be optimized to retrieve the steep SWA. As the proposed method is fast, highly sensitive and easy to implement, it provides a powerful approach to investigate the scattering behavior of nanostructures.

4.1. INTRODUCTION

In the semiconductor industry, the photomask is a key component in the lithographic system. The accurate evaluation of the structures on the photomask dominates the performance of the end products. Consequently, a strictly precise description of the shape of the groove on the photomask plays an important role in the in-line process control and process development. Those structures are often gratings whose shape can be described by some geometrical parameters, such as period, middle critical dimension, height and SWA. In practical applications, the grating period is generally the best controlled parameter, the SWA is more difficult to determine optically than the middle critical dimension and the height [2].

In recent years, with continuous miniaturization of photonic and electronic devices, the mask feature sizes become smaller and smaller, and consequently, the SWA has become increasingly important in lithography mask fabrication. For example, EUV masks need steep vertical SWA, since in case of non-vertical SWA, the transferred pattern sizes on the wafer will be affected by shadowing effects. If there is a large deviation in the final etched pattern, it will deteriorate the subsequent fabrication of further layers on the nanostructure, and it may even lead to the failure of the chip. The verticality of the SWA, therefore, has become a crucial factor in mask fabrication [3]. Non-destructive determination of the SWA, especially for reconstruction of steep SWA with high precision is obviously indispensable in nanostructure metrology.

Several techniques have been used to measure the SWA, currently, AFM and SEM are the two most popular methods. For SEM [4–6], both the cross-sectional scanning electron microscopy (X-SEM) and critical dimension scanning electron microscopy (CD-SEM) have drawbacks, for instance, in the case of X-SEM, one needs to cut the sample to observe its cross-section, which might introduce extra errors, while with CD-SEM the SWAs have to be computed indirectly, with the resolution being limited by the primary electron beam diameter. For AFM [7–10], it is hard to measure SWAs greater than the slant angle of the tips, and also its low throughput is an obstacle. Moreover, these methods are all based on near-field measurements, and the experimental systems are very complex, with rigorous operating conditions.

To overcome these drawbacks in dimensional and structural metrology, a non-destructive, fast and quantitative method such as optical scatterometry has become commonly used for nanostructure profile reconstruction, in particular in in-line lithographical manufacturing process. Optical scatterometry [11, 12] is inherent a model-based metrology technique that is used to reconstruct the optimal nanostructure profile parameters by continuously matching the theoretical signatures with the measured ones. The theoretical model for the scattering process is based on the rigorous solution of Maxwell's equations. Many methods have been proposed, depending on the structure features, such as the so-called C method [13, 14], the rigorous coupled wave analysis (RCWA) [15–17], the finite element method (FEM) [18–20], and the finite difference time domain (FDTD) [21–23], etc. For instance, RCWA is primarily suitable for calculation of diffraction field of periodic structures, while FEM is more flexible to solve boundary value problems.

In this chapter, we propose a novel detection optical system for the determination of steep SWAs that explores asymmetries in the far-field scattered light. The proposed approach is appropriate for all values of SWAs but here we focus on steep SWAs because

there it is still a lot of challenges associated with them. Numerical calculations using the FDTD method are carried out to verify the detection capabilities of the scheme. The rigorous electromagnetic interaction between a cliff-like structure and the focused laser beam generated by a cylindrical lens is modeled to distinguish different steep SWAs, which is closer to the experimental situation and more accurate than the scalar analysis [24]. We conduct lateral and longitudinal scanning of the structure for both TE and TM polarization, and monitor the scattered light by a split detector to analyze the polarization effect in the far field. The results reveal that TM polarization is more sensitive for steep SWA detection, and it could be possible distinguish SWA differences below 1°, which meets the technological requirement of absorber SWA in ITRS2008 roadmap [25]. We defined a quantity called the "visibility" to quantify the influence of the longitudinal focus position to steep SWA detection in the TM case. The results reveal that there is a feasible longitudinal focus interval which can be used to distinguish steep SWAs with different heights of the structure, and within this interval, there is an optimal focus position. Our findings present a robust and sensitive determination method for steep SWAs in far-field detection, and we believe it will provide a feasible approach for accurate measurement of more complicated nanostructures.

4.2. METHODOLOGY

A cliff-like structure is shown in Figure 4.1(a). We select one cliff-like subarea as the target structure as it is the pivotal part of a general grating profile. Grating profiles are obtained by varying the height and SWA of the structure. Figure 4.1(b) is the proposed detection system for SWA determination, where the cliff-like structure is centered in a right hand coordinate system and is illuminated by a probe beam. For simplicity we assume that the cliff-structure is infinite along the x-axis and invariant with respect to the y coordinate. Consequently, the disturbances from other parameters are avoided, and the structure can be fully described by the SWA and height in the xz plane. A collimated laser beam with polarization in the pupil which is either parallel (TE) or perpendicular (TM) to the y-axis, is focused on the upper interface of the structure through a cylindrical lens. By using a cylindrical lens, the interaction of the light with the structure is a two-dimensional scattering problem.

It has been demonstrated in previous work [24, 26, 27] that an object can be described as a phase step if its slope is sufficiently steep. The phase step will introduce an offset to the scattered light due to the path difference on either side of the step, as shown in Figure 4.1(c). Furthermore, the relative movement between the structure and the incident beam will bring a dynamic variation in the far field, which can be collected through the same cylindrical lens. To get a high sensitivity at high speed, a split-detector technology is implemented, which is often used in differential phase-contrast microscope [28–30]. The split detector measures the intensity in both halves of the exit pupil and integrates each of them and then subtracts them after normalization:

$$\chi = \frac{\int_{-r}^{0} I^{\text{out}}(\xi)\, d\xi - \int_{0}^{r} I^{\text{out}}(\xi)\, d\xi}{\int_{-r}^{0} I^{\text{out}}(\xi)\, d\xi + \int_{0}^{r} I^{\text{out}}(\xi)\, d\xi}, \tag{4.1}$$

where $r = \text{NA} \cdot f$ defines the detection area, NA is the numerical aperture of the cylindrical

lens, f is the focal length, and ξ is the coordinate in the exit pupil. Theoretically, the detection sensitivity and the anti-noise performance can be improved by considering the difference of the integrals of the two halves.
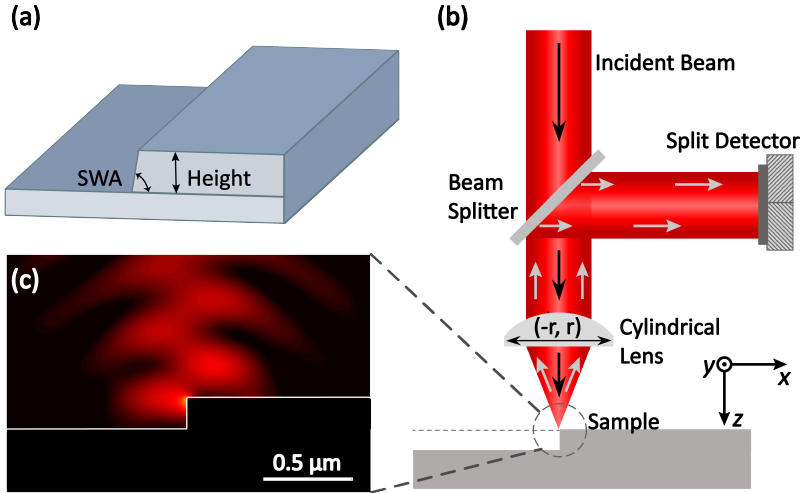

Figure 4.1: (a) Scheme of the cliff-like structure showing its geometrical parameters. The structure is fully described by height and SWA. (b) Diagram of a reflection scanning system with a split detector. A collimated laser beam with wavelength of 633 nm is focused onto the sample by a cylindrical lens with NA of 0.6. The scattered light is collected by the same lens and finally recorded by a split detector. (c) The simulated near-field intensity showing the interaction between the focused beam and silicon-based cliff-like structure in xz plane for TM polarization.

To study the interaction between the cliff-like structure and probe beam, we performed simulations using the commercial software "FDTD solutions" (Lumerical Inc., Canada). A two-dimensional FDTD model is built with a total simulation region of 10 μm × 8 μm, where the silicon step structure (as described in Figure 4.1(b)) is created in the bottom region and all other part are air. A 633 nm-wavelength TM- or TE-polarized light source is generated through a self-written script based on Refs. [31, 32], and focused on the upper surface of the silicon structure with the NA of 0.6. The refractive index of silicon is $3.882 + 0.019i$ at this wavelength as given by the FDTD material database. Perfectly matched layer (PML) boundary conditions are used at all boundaries of the simulation domain without causing reflections. In order to provide enough computational precision to distinguish different SWAs, the grid size in the cliff-shape region (as described in Figure 4.1(c)) is chosen as 2 nm in the x-direction and 5 nm in the z-direction; Finally, the far-field is calculated by projecting the scattered near field obtained from FDTD simulation to the pupil plane.

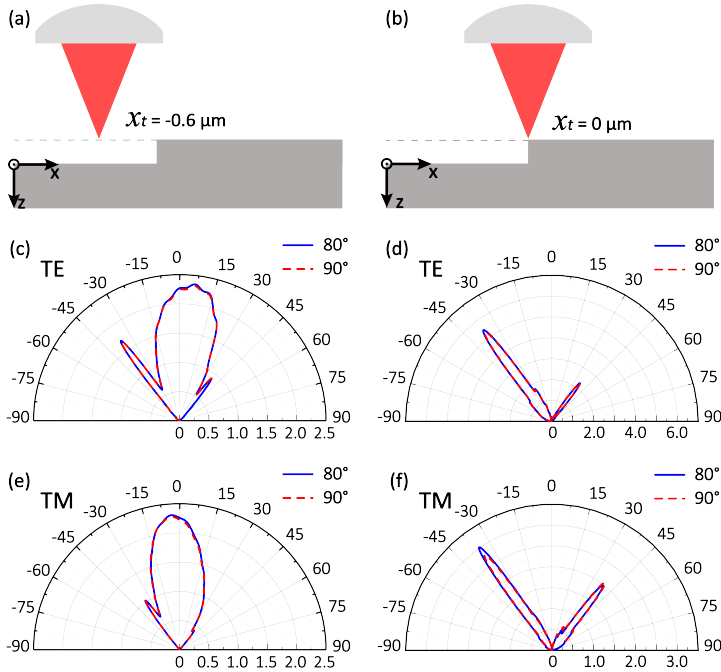## 4.3. THE COMPARISON BETWEEN TE AND TM MODES

Figure 4.2: Explanation of the process of the lateral scanning of the focused beam. The probe beam is scanned along x-axis from left to right as shown in (a) and (b). The translation is denoted by x_t. (c) and (d) are the far-field radiation field when $x_t = -0.6$ μm and 0 for the TE polarization, respectively. (e) and (f) are the far-field radiation field when $x_t = -0.6$ μm and 0 for the TM polarization.

To better understand the offset caused in the scattered light by the step, we begin with the height set to $\lambda/4$ and SWA of $90°$, which satisfies the quadrature condition (i.e. the phase difference between the reference and the signal beam is around $\pi/2$) [26]. We firstly perform a lateral scan, with the probe beam focused on the upper interface of the structure. The translation of the focus spot along the x-direction is defined by x_t, and the probe beam moves from negative to positive x_t, where $x_t = 0$ means that the centre of the spot is on the edge of the step, as shown in the Figure 4.2(a) and (b). Figure 4.2(c) and (d) show the far-field radiation field in the pupil plane for TE polarization, and Figure 4.2(e) and (f) for TM polarization. Figure 4.2(c) (e) and (d) (f) correspond to two scanning positions, namely $x_t = -0.6$ μm and 0μm, respectively. For $x_t = -0.6$ μm (Figure 4.2(c) and (e)), a major portion of the radiation field is concentrated in the center with two small side lobes, which means that when the probe beam is relatively far from the cliff-structure, the probe beam is mainly reflected by the surface. As one can see, the intensity of the two twigs in Figure 4.2(c) is much bigger than in Figure 4.2(e), which indicates that the TE and TM modes have different edge scattering behavior; for both Figure 4.2(c) and (e), the

far-field intensities for 80° and 90° highly coincide, when the probe beam is far from the cliff-structure. For the beam focused at the center $x_t = 0$, the scattered light from the right and left halves of the step exerts a π phase difference. The scattered light in the middle part becomes very weak after interference, leaving two asymmetric radiation fields at divergence angle around $\pm 40°$ with a high intensity, as shown in Figure 4.2(d) and (f). Although the intensity ratio between the two lobes in Figure 4.2(d) is larger than in Figure 4.2(f), the difference of between the intensity patterns for SWA 80° and 90° is larger for TM (Figure 4.2(f)) than for TE (Figure 4.2(d)).
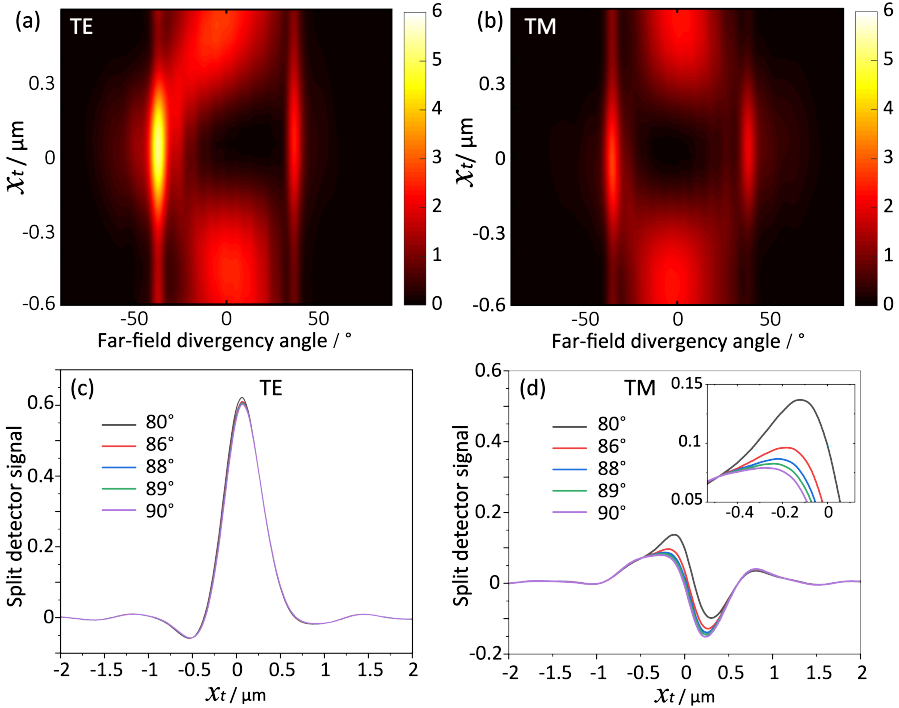

Figure 4.3: Top: Stacks of the far-field radiation field for different scanning positions x_t in (a) TE and (b) TM polarization for a cliff-like structure with height = $\lambda/4$ and SWA = 90°. Bottom: split detector signals for a cliff-like structure with different SWAs, namely 80°, 86°, 88°, 89° and 90° under two different polarizations: (c) TE polarization and (d) TM polarization.

Figure 4.3(a) shows the variation of the intensity of the scattered far field for TE polarization, for scanning position x_t in the range from $-0.6\ \mu m$ to $0.6\ \mu m$, with scanning step of $0.06\ \mu m$ and for SWA of 90°. Figure 4.3(b) is analogous to Figure 4.3(a) for TM polarization. The results show that the radiation distribution in the far field for TE and TM polarization are similar. There is however a difference in the ratio of the intensities in the two lobes when the probe crosses the edge of the step. This phenomenon can be explained by the electromagnetic boundary conditions [33]. Figure 4.3(c) and (d) shows

the split detector signals for a cliff-like structure with different SWAs as function of the scanning position x_t for TE and TM polarization, respectively. The height of the step is $\lambda/4$ again and SWA is 80°, 86°, 88°, 89° and 90°. The longitudinal position of the focus is fixed at the upper interface of the sample, in accordance with the scheme in Figure 4.2. The lateral scanning region ranges from -2 to $2\ \mu$m, with the same scanning step as before. According to Figure 4.3(a), for TE polarization the scattered intensity in the left half of the pupil is always larger than in the right half, and the split detection signal is always positive. Furthermore, the split detector signals for all five SWAs highly coincide, meaning that TE polarization is not very sensitive to changes in steep SWAs.

In contrast, for TM polarization shown in Figure 4.3(d), the split detection signal clearly differs for different SWAs. Each SWA produces a unique 'heartbeat' signal, with different amplitudes. The insert in Figure 4.3(d) shows that the difference between 89° and 90° is still visible and possibly could be measurable, which makes us conclude that the scattering due to TM polarization has the potential for applications in determining steep SWA to the order of 1°. Although the absolute value of the split detect signal for TE polarization is higher than for TM, its sensitivity to SWA variation is smaller. The results show thus that TM polarization is preferable for steep SWA determination.
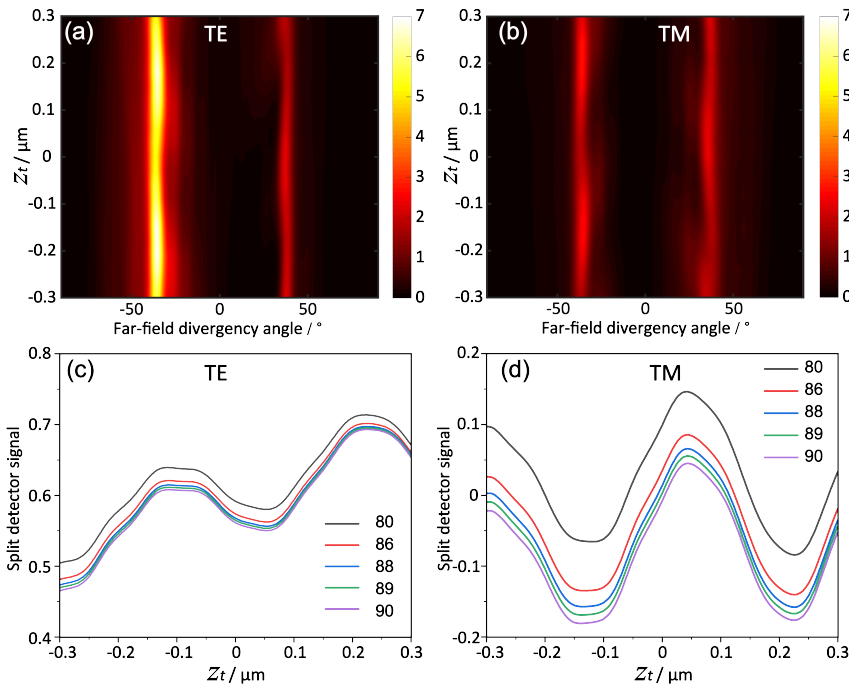

Figure 4.4: The stacks of the far-field radiation field along different vertical scanning positions z_t in (a) TE and (b) TM polarization for a cliff-like structure with height = $\lambda/4$ and SWA = 90°. The split detector signals for five different SWAs for two different polarizations: (c) TE polarization and (d) TM polarization.

Since we consider the dependence on the position of the focus of the incident spot, it is hard to determine the exact position of the focal plane of the laser beam w.r.t. the structure. Figure 4.4(a) and (b) show the longitudinal scanning results of the same structure (height = $\lambda/4$, SWA = 90°) shown in Figure 4.2 along different focal position z_t. The lateral position of the beam is fixed at $x_t = 0$, and the beam moves from top to bottom with focus plane position (z_t) changing from 0.3 μm to −0.3 μm. Note that $z_t = 0$ corresponds to the probe beam being focused at the upper interface of the structure. As shown, scattering angle where maximum field amplitude occurs is located mainly around ±40° scattering angle for both polarizations. As consequence, the scattered light could be collected without any position adjustment when the polarization changes.

In Figure 4.4, when the incident beam is TE polarization, the scattered field is for all focal positions z_t more strongly scattered to the left than to the right side of the pupil, but the ratio of the left and right intensities changes gradually with longitudinal focal position. As shown in Figure 4.4(b), the scattered field much more strongly varies with longitudinal focus for TM polarization than for TE. Figure 4.4(c) and (d) show the split detector signals for different steep SWAs for TE and TM polarizations, respectively, when $x_t = 0$. The parameters of the tested structure are kept the same in Figure 4.3, i.e., the step height is $\lambda/4$ and the SWA is 80°, 86°, 88°, 89° and 90°. The scanning range is from 0.3 μm to −0.3 μm and step size is 0.01 μm. As demonstrated in Figure 4.4(c), although the longitudinal focus position changes the far field distribution, the overall trend of the five split detection signals looks quite similar. While for the TM case, as shown in Figure 4.4(d), the difference between the split detector signals for different SWAs is more obvious. In conclusion, the split detector signals generated by changing the longitudinal focus positions could also be used to retrieve the SWAs of the nanostructure.

4.4. THE DETECTION SENSITIVITY ANALYSIS

The comparison of TE and TM polarization for both lateral and longitudinal scanning, imply that TM polarization is more sensitive than the TE polarization for difference in SWA. We have also studied the transitional polarizations between the TE and TM mode, and as result, we conclude that TM polarization is the optimal one. We therefore further explore the TM case. For a quantitative description of the detection sensitivity, we define a contrast value of split detector signals χ, as:

$$\text{visibility} = \frac{|\max(\chi)| - |\min(\chi)|}{|\max(\chi)| + |\min(\chi)|}, \tag{4.2}$$

where $\max(\chi)$ and $\min(\chi)$ are the maximum and minimum of the split detector signal. It should be noted that the absolute value of minimum χ can be greater than that of the maximum, the visibility value can be negative under some conditions.

For each vertical focus position, a horizontal scanning is performed to get a series of far-field radiation patterns, referring to the horizontal rail in Figure 4.3(b). We further get the split detector signal of the far-field from Equation 4.1 as function of x_t. The visibility value is calculated from Equation 4.2 by getting the extreme value of the split detector signal. Finally, only one scalar quantity is obtained from the stacks of far-field radiation field with respect to z_t.

The visibility is plotted as a function of the longitudinal focus position in Figure 4.5(a). It demonstrates that the visibility of 80° is always higher than the other four SWA values, and very distinguishable. For quasi-vertical SWAs, however, the optimum focus position should be used, since the difference between the visibilities is small. The largest variation of the visibility as function of focus position for SWAs close to 90° occurs for focal position z_t =0.05 μm, hence 50 nm above the upper surface. The results of visibility are logical and consistent with expectation: focusing on the upper interface of the structure is not the only valid position, there is indeed a feasible focus interval to detect steep SWAs.

The above simulations are based on the condition that the height is equal to $\lambda/4$. The cases for other heights have also been investigated, and the results are shown in Figure 4.5(b). The SWA in this case is fixed at 90° and the height is equal to 148 nm, 158 nm and 168 nm. We can see that the height also has a strong influence on the visibility values, but the focus interval around $z_t \approx 0.05$ μm is still good to use. In addition to 90°, we also investigated other SWAs with different heights. The results show the same tendency as in Figure 4.5(b). This indicates that our method is still valid when the wavelength of the focused beam is fixed and the structure height has a tolerant deviation from $\lambda/4$, and with the right focus interval we can accurately retrieve the steep SWAs. It is important to emphasize that the requirement on the physical height of the sample is not stringent. Our method can be used in a wide range of heights by adjusting the incident wavelength.
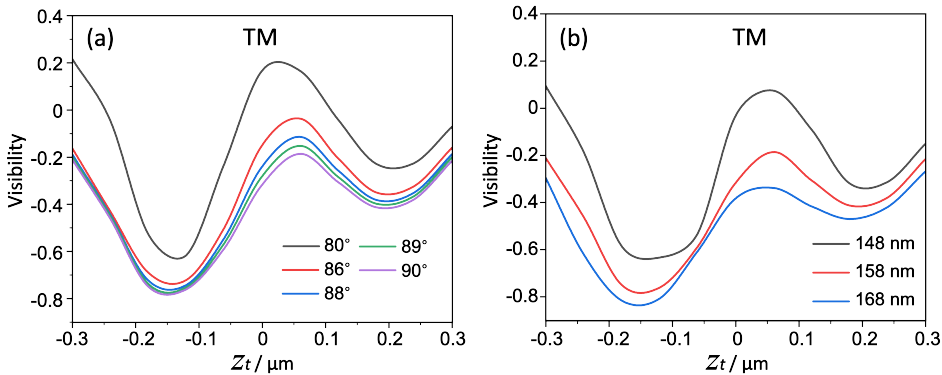

Figure 4.5: (a) Visibility of the split detector signal as function of the focal position z_t of the spot for five values of SWA. The visibility is defined by Equation 4.2, as explained in the main text. (b) The visibility as function of the focal position of the focal spot for three different heights when the SWA is fixed to 90°.

4.5. CONCLUSIONS

In conclusion, we have proposed an efficient approach for distinguishing steep SWAs of a cliff-like structure by analyzing the far-field scattering signals. An incident beam is focused onto the structure by a cylindrical lens, and the scattered light is collected by the same cylindrical lens and detected by a split-detector to record the far-field signals. Both lateral and longitudinal scanning of the structure under TE and TM polarization are

performed to optimize the detection sensitivity. The simulations demonstrate that the polarization state is an important factor to modulate the far-field scattering field, and TM polarization is much more suitable for steep SWA detection than TE polarization. A parameter called "visibility" is defined to quantify the influence of the longitudinal focus position on detecting steep SWA. There is a feasible vertical focus interval that can be used to distinguish different SWAs, and inside this interval there is an optimum focus position. For step height of a quarter wavelength, TM configuration can be applied to detect the SWA difference with accuracy higher than 1° at a suitable focus position. Also, according to simulations, the method is robust even after adding a small surface roughness to the step. The proposed approach is fast, highly sensitive and easy to implement. Moreover, the influences of height deviations are also analyzed. For realization of the experiments, there are many factors that need special attention, such as the alignment between the structure and focused beam, focusing and tilting errors. There should be also special attention to the detector, as this should have low noise amplifiers and probably combined with heterodyne techniques given that the expected voltage differences are small. We envision that, in the future, machine learning [34] can be applied to solve the inverse problem in scatterometry by building a comprehensive database based on calculations as presented in this paper to analyze the experimental data.

References

[1] **X. Dou**, S. F. Pereira, C. Min, Y. Zhang, P. Meng, H. P. Urbach, and X. Yuan. "Determination of steep sidewall angle using polarization-sensitive asymmetric scattering". In: *Measurement Science and Technology* 32.8 (2021), p. 085201.

[2] S. Peterhänsel, M. L. Gödecke, K. Frenner, and W. Osten. "Phase-structured illumination as a tool to detect nanometer asymmetries". In: *Journal of Micro/Nanolithography, MEMS, and MOEMS* 15.4 (2016), pp. 044005–044005.

[3] H. Hakii, I. Yonekura, M. Kawashita, Y. Kojima, Y. Sakamoto, and K. Tanaka. "An evaluation of a new side-wall-angle measurement technique for mask patterns by CD-SEM". In: *Photomask and Next-Generation Lithography Mask Technology XVI*. Vol. 7379. SPIE. 2009, pp. 596–607.

[4] C. Frase, W. Häßler-Grohne, G. Dai, H. Bosse, Y. A. Novikov, and A. Rakov. "SEM linewidth measurements of anisotropically etched silicon structures smaller than 0.1 μm". In: *Measurement science and technology* 18.2 (2007), p. 439.

[5] C. G. Frase, E. Buhr, and K. Dirscherl. "CD characterization of nanostructures in SEM metrology". In: *Measurement Science and Technology* 18.2 (2007), p. 510.

[6] H. Fukaya, T. Murakawa, S. Shida, M. Kuribara, T. Iwai, J. Matsumoto, T. Nakamura, H. Hakii, I. Yonekura, M. Kawashita, *et al.* "New CD-SEM metrology method for the side wall angle measurement using multiple detectors". In: *Photomask and Next-Generation Lithography Mask Technology XVIII*. Vol. 8081. SPIE. 2011, pp. 81–91.

[7] B.-F. Ju, Y.-L. Chen, W. Zhang, and F. Fang. "Rapid measurement of a high step microstructure with 90 steep sidewall". In: *Review of Scientific Instruments* 83.1 (2012), p. 013706.

[8] A. Cordes, B. Bunday, and E. Cottrell. "Sidewall slope sensitivity of CD-AFM". In: *Instrumentation, Metrology, and Standards for Nanomanufacturing, Optics, and Semiconductors V*. Vol. 8105. SPIE. 2011, pp. 30–37.

[9] D. Hussain, K. Ahmad, J. Song, and H. Xie. "Advances in the atomic force microscopy for critical dimension metrology". In: *Measurement Science and Technology* 28.1 (2016), p. 012001.

[10] A. Yacoot and L. Koenders. "Aspects of scanning force microscope probes and their effects on dimensional measurement". In: *Journal of Physics D: Applied Physics* 41.10 (2008), p. 103001.

[11] C. Raymond. "Overview of scatterometry applications in high volume silicon manufacturing". In: *AIP Conference Proceedings*. Vol. 788. 1. American Institute of Physics. 2005, pp. 394–402.

[12] C. J. Raymond. "Scatterometry for semiconductor metrology". In: *Handbook of silicon semiconductor metrology*. CRC Press, 2001, pp. 389–418.

[13] J. Chandezon, G. Raoult, and D. Maystre. "A new theoretical method for diffraction gratings and its numerical application". In: *Journal of Optics* 11.4 (1980), p. 235.

[14] G. Granet, J. Chandezon, J.-P. Plumey, and K. Raniriharinosy. "Reformulation of the coordinate transformation method through the concept of adaptive spatial resolution. Application to trapezoidal gratings". In: *JOSA A* 18.9 (2001), pp. 2102–2108.

[15] M. Moharam and T. Gaylord. "Rigorous coupled-wave analysis of planar-grating diffraction". In: *JOSA* 71.7 (1981), pp. 811–818.

[16] M. Moharam and T. K. Gaylord. "Three-dimensional vector coupled-wave analysis of planar-grating diffraction". In: *JOSA* 73.9 (1983), pp. 1105–1112.

[17] L. Li and C. W. Haggans. "Convergence of the coupled-wave method for metallic lamellar diffraction gratings". In: *JOSA A* 10.6 (1993), pp. 1184–1189.

[18] X. Wei, A. J. Wachters, and H. P. Urbach. "Finite-element model for three-dimensional optical scattering problems". In: *JOSA A* 24.3 (2007), pp. 866–881.

[19] H. Gross, R. Model, M. Bär, M. Wurm, B. Bodermann, and A. Rathsfeld. "Mathematical modelling of indirect measurements in scatterometry". In: *Measurement* 39.9 (2006), pp. 782–794.

[20] G. Demésy, F. Zolla, A. Nicolet, M. Commandré, and C. Fossati. "The finite element method as applied to the diffraction by an anisotropic grating". In: *Optics Express* 15.26 (2007), pp. 18089–18102.

[21] A. D. Papadopoulos and E. N. Glytsis. "Finite-difference-time-domain analysis of finite-number-of-periods holographic and surface-relief gratings". In: *Applied optics* 47.12 (2008), pp. 1981–1994.

[22] C. Wang, X. Chen, H. Gu, H. Jiang, C. Zhang, and S. Liu. "On the limits of low-numerical-aperture imaging scatterometry". In: *Optics express* 28.6 (2020), pp. 8445–8462.

4

[23]   S.-D. Wu and E. N. Glytsis. "Finite-number-of-periods holographic gratings with finite-width incident beams: analysis using the finite-difference frequency-domain method". In: *JOSA A* 19.10 (2002), pp. 2018–2029.

[24]   L. Cisotto, S. F. Pereira, and H. P. Urbach. "Analytical calculation on the determination of steep side wall angles from far field measurements". In: *Journal of Optics* 20.6 (2018), p. 065601.

[25]   T. Watanabe, K. Tatsumura, and I. Ohdomari. "International technology roadmap for semiconductors 2005 edition". In: *Physical Review Letters* 96.19 (2006), p. 196102.

[26]   N. Hermosa, C. Rosales-Guzmán, S. F. Pereira, and J. Torres. "Nanostep height measurement via spatial mode projection". In: *Optics letters* 39.2 (2014), pp. 299–302.

[27]   B. Zhang, D. F. Gardner, M. D. Seaberg, E. R. Shanblatt, H. C. Kapteyn, M. M. Murnane, and D. E. Adams. "High contrast 3D imaging of surfaces near the wavelength limit using tabletop EUV ptychography". In: *Ultramicroscopy* 158 (2015), pp. 98–104.

[28]   M. R. Atkinson, A. Dixon, and S. Damaskinos. "Surface-profile reconstruction using reflection differential phase-contrast microscopy". In: *Applied optics* 31.31 (1992), pp. 6765–6771.

[29]   C. W. See, M. V. Iravani, and H. Wickramasinghe. "Scanning differential phase contrast optical microscope: application to surface studies". In: *Applied optics* 24.15 (1985), pp. 2373–2379.

[30]   W. Amos, S. Reichelt, D. Cattermole, and J. Laufer. "Re-evaluation of differential phase contrast (DPC) in a scanning laser microscope using a split detector as an alternative to differential interference contrast (DIC) optics". In: *Journal of microscopy* 210.2 (2003), pp. 166–175.

[31]   C. J. Sheppard. "Cylindrical lenses—focusing and imaging: a review". In: *Applied optics* 52.4 (2013), pp. 538–545.

[32]   S. B. Purnapatra and P. P. Mondal. "Determination of electric field at and near the focus of a cylindrical lens for applications in fluorescence microscopy". In: *AIP Advances* 3.5 (2013), p. 052124.

[33]   D. Qu, X. Yuan, and R. Burge. "Polarization dependence of the electromagnetic field distribution across wavelength-sized relief grating surfaces". In: *JOSA A* 10.11 (1993), pp. 2317–2323.

[34]   L. Xu, M. Rahmani, Y. Ma, D. A. Smirnova, K. Z. Kamali, F. Deng, Y. K. Chiang, L. Huang, H. Zhang, S. Gould, *et al.* "Enhanced light–matter interactions in dielectric nanostructures via machine-learning approach". In: *Advanced Photonics* 2.2 (2020), pp. 026003–026003.

5

POLARIZATION SINGULARITY ASSISTED DETERMINATION OF STEP-SHAPED NANOSTRUCTURE

We propose a novel metrology method to determine simultaneously the height and side-wall angle of a step-shaped silicon nanostructure. By employing an optical singular beam into a typical coherent Fourier scatterometry system, both parameters can be retrieved through analyzing the intensity profile of the far-field scattering pattern. The use of singular beam is shown to be sensitive to slight changes of the parameters of the step. By changing the relative direction between the singularity and structure, the height and side-wall angle can both be retrieved with high precision. This new method is robust, simple, and can provide valuable means for micro-and-nano- metrology.

5.1. INTRODUCTION

With the continuously reduction of the dimensions of semiconductor devices, there has been a strong demand for a simple, robust, non-invasive, and far-field optical detection technique that is sensitive to nanoscale dimensions. This demand is mainly driven by the requirements of the production quality control, in-line process control and production equipment in the semiconductor industry. Several near-field microscopy systems [2–6] such as atomic force microscopy and scanning electron microscopy, can provide extremely high resolution. However, they are not suitable for industrial environment since they operate mostly off-line, they are expensive, have low throughput and some of them are invasive. In principle, optical methods are good candidates to overcome those difficulties. Optical scatterometry [7, 8], which uses the far-field optical scattering to retrieve the geometrical features of a structure, is a non-invasive in-situ detection method, with Fourier Scatterometry (FS) being distinguished by the detection plane. In FS, the light that is scattered from the structure at different angles is recorded and analyzed at the Fourier plane in one shot [9–11]. Coherent Fourier scatterometry (CFS) uses a coherent focused beam to illuminate the structure [12]. The use of coherent illumination makes CFS quite competitive and even superior to the incoherent counterpart. CFS has been successfully applied to detect the shape parameters of grating structures as well as to the detection of nano-particles and contamination [13–16].

Spatially modulated structured light, refers to a light beam with specially designed intensity, phase, or polarization distribution patterns [17–19]. It has drawn extensive attention of researchers because of its novel characteristics in many fields. Structured light beams with an optical singularity, also called singluar beams [20–22], have potential for a lot of applications. The singularity often refers to the discontinuities in phase or polarization in the light field, and the optical field intensity usually has a sharp decrease near the singularity. It has been shown that the dark singularity can be extremely sensitive to detect slight changes in the field due to its interaction with (nano)objects [23–29]. Such property of the singular beam has been verified to be feasible in precise measurement of nanostructures [25].

In this chapter, we employ a singular beam on a Coherent Fourier Scatterometry (CFS) scheme to determine both the height and side-wall angle (SWA) of a step-shaped silicon nanostructure simultaneously. A numerical 3-dimensional (3D) rigorous model is built, and the computed scattered far-field intensity is further analysed. Due to the high sensitivity driven by the singularity line of the beam, the numerical results demonstrate that the proposed approach can distinguish tiny differences in height and SWA. As an effective and robust method, this work could provide a good complement to the CFS technique for finer measurements of nanostructures.

5.2. METHODOLOGY

5.2.1. GENERATION OF THE DESIRED BEAM

In conventional CFS, the nanostructure sample is illuminated by a coherent focused beam with a truncated Gaussian spatial profile, and is then further investigated via a raster-scanning of the structure. Here, we introduce a (1,0) mode Hermite-Gaussian (HG$_{10}$) singular beam (with a line singularity in the center) into the conventional CFS to

improve the detection sensitivity and increase the scanning speed.

A novel liquid crystal polarization modulation technique is employed to generate HG_{10}, which is significantly more efficient and flexible than the previous methods. The polarization state of a laser beam is modulated at the scale of single pixel of a liquid crystal device, e.g., Q-plate and liquid crystal polymer vortex waveplate (VP) that we are going to talk about. The so-called VP is essentially a half-wave plate with a constant phase delay over the entire aperture, but the fast axis rotates continuously over the entire plate. VPs can turn linearly polarized beams into arbitrary order cylindrical vector beams (CVBs), and can also turn circularly polarized beam to optical vertices with arbitrary topological charges.

We will investigated theoretically the generation of m-th order CVB as an example to describe the inherent transform mechanism in the framework of the Jones matrix theory [30, 31]. The Jones matrix of the incident linearly polarized beam can be expressed as

$$\boldsymbol{E}_i = \begin{bmatrix} \cos\theta & \sin\theta \end{bmatrix}^T, \tag{5.1}$$

and that of the m-th order CVB as

$$\boldsymbol{E}_o = \begin{bmatrix} \cos(m\varphi + \varphi_0) & \sin(m\varphi + \varphi_0) \end{bmatrix}^T, \tag{5.2}$$

where θ represents the orientation of the incident linear polarization with respect to the x-axis, φ the azimuthal angle, and φ_0 the inner polarization rotation of the CVBs. Supposing that the Jones matrix M of VP is defined as

$$M = \begin{bmatrix} A & B \\ C & D \end{bmatrix}. \tag{5.3}$$

To generate the aimed m-th order CVBs, the input beam $\boldsymbol{E}_i$, the output beam $\boldsymbol{E}_o$, and M should satisfy the relation $M\boldsymbol{E}_i = \boldsymbol{E}_o$, i. e.

$$\begin{bmatrix} A & B \\ C & D \end{bmatrix} \begin{bmatrix} \cos\theta \\ \sin\theta \end{bmatrix} = \begin{bmatrix} \cos(m\varphi + \varphi_0 \pm \theta) \\ \sin(m\varphi + \varphi_0 \pm \theta) \end{bmatrix}, \tag{5.4}$$

the symbol $\pm$ before θ indicates either clockwise or anticlockwise changing VPs to generate the m-th order CVBs. The Jones matrix of the clockwise changing VPs can thus be expressed as

$$M_c = \begin{bmatrix} \cos(m\varphi + \varphi_0) & -\sin(m\varphi + \varphi_0) \\ \sin(m\varphi + \varphi_0) & \cos(m\varphi + \varphi_0) \end{bmatrix}, \tag{5.5}$$

while that of the anticlockwise changing VPs is

$$M_a = \begin{bmatrix} \cos(m\varphi + \varphi_0) & \sin(m\varphi + \varphi_0) \\ \sin(m\varphi + \varphi_0) & -\cos(m\varphi + \varphi_0) \end{bmatrix}. \tag{5.6}$$

The relationship between M_c and M_a is $M_c = M_a H_0$, where H_0 denotes a half waveplate with fast axis oriented horizontally. It should be noted that if incident beams are orthogonal to each other, the output CVBs remain orthogonal. For example, if a first order ($m = 1$) VP turns a x-polarized beam, namely $\theta = 0$, into radially polarized beam, then

an azimuthally polarized beam can be obtained from a y-polarized beam ($\theta = \pi/2$). The energy efficiency of this method is above 96%.

Ideally, optical devices with the Jones matrix of Equation 5.5 and 5.6 are able to convert linearly polarized beams into an arbitrary aimed m-th order CVBs. However, the precisely designing and fabricating all of the orders of the optical converters is time-consuming and expensive. To avoid this problem, the physical link among different order VPs is further investigated, as

$$M_m = M_{m\text{-}n} H_0 M_n. \tag{5.7}$$

The above Equation 5.7 reveals that a high-order VP can be achieved by cascading two low-order VPs with a half wave-plate, and there is no need to manufacture all of the high-order VPs.
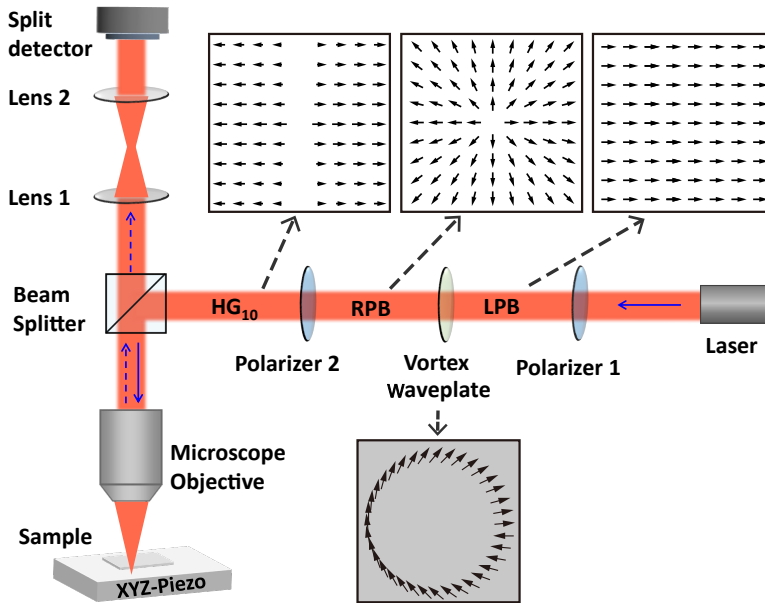
Figure 5.1: A reflective coherent scatterometer illuminated by a singular beam. A collimated laser beam passes through two linear polarizers with a vortex waveplate in between to generate the desired HG_{10} beam. This beam is then focused onto the sample by a microscope objective. The scattered and reflected light is collected by the same objective and finally analyzed by the split detector.

Our desired beam HG_{10} can be generated by a radially polarized beam, in this case, a first-order VP is applied. The schematics of the entire system is depicted in Figure 5.1. The incident collimated beam ($\lambda = 633$ nm) is firstly transformed to a linearly polarized beam by passing through the first linear polarizer, and then linearly polarized beam is converted into radially polarized beam by the VP element [30, 32]. The radially polarized beam then passes through another linear polarizer to produce the desired HG_{10} beam. As shown in the generation diagram, arrows in the squares in the upper-right corner indicate

the polarization direction of corresponding beams, while those in the circle at the bottom depicts the fast axis direction of the VP, which can clearly demonstrate the process of beam generation. Then the generated HG_{10} beam is further focused by a microscope objective (NA= 0.6) onto the sample structure. The scattered and reflected light from the structure is collected by the same objective, and the Fourier plane of the objective is imaged at a split detector through a beam splitter and a $4f$ system.

5.2.2. THE DETECTION APPROACH

The intensity and phase pattern of the generated HG_{10} beam before the microscope objective are shown in Figure 5.2(a) and (b), and the focused beam at the plane of the structure has been calculated by a three-dimensional Fourier transform method based on the Debye-Wolf integral [33–35], with FWHM of the focus size is 1.15 μm. As shown in Figure 5.2(a), a zero-intensity singularity line appears in the middle of the pattern, with a π-phase jump between the two sides across the singularity. The black arrows in Figure 5.2(a) indicates the direction of the polarization.
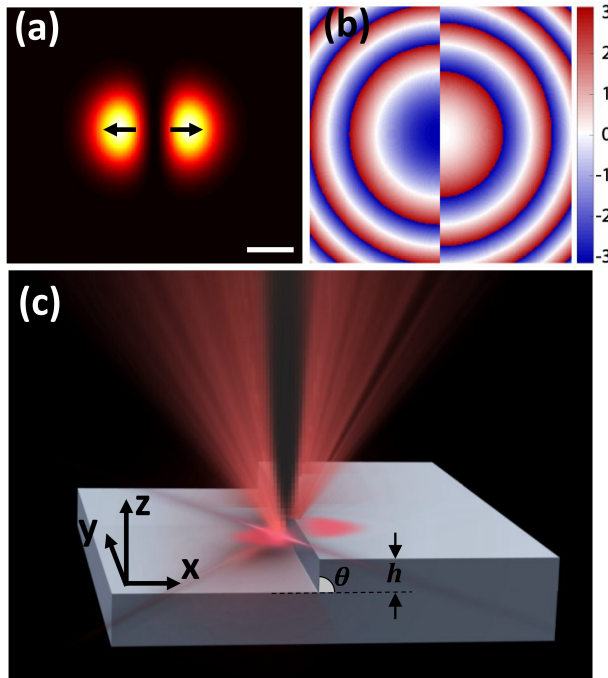
Figure 5.2: (a) The intensity and (b) phase distribution of the HG_{10} beam. The polarization is perpendicular to the singularity line as indicated by the black arrows. Scalebar is 500 nm. (c) 3D view of the interaction between HG_{10} beam and step-shaped silicon nanostructure.

Most nanostructures used to characterize the quality of nano fabrication have local steep walls and ridges of different widths. For simplicity, here, the studied structure is

selected as a step-shaped silicon structure with height and SWA which is invariant with respect to the y-coordinate. Figure 5.2(c) schematically shows the situation when the focused linear singularity is aligned along the edge of the step-shaped sample (which we will call the parallel configuration), where the left side lobe of the focused HG_{10} beam is projected onto the lower surface of the step structure and the right one onto the upper surface. The incident HG_{10} beam can be freely rotated by changing the direction of linear polarizer 2, and therefore the angle between the singularity line and the edge of nanostructure is tunable.

In addition to the parallel configuration, we also consider the other typical situation named perpendicular configuration, where the line singularity of HG_{10} beam is perpendicular to the edge of the structure, which can be achieved by rotating the polarizer 2 (or the sample) by 90° w.r.t. the parallel configuration. Note that these configurations can also be obtained by keeping the input beam fixed and rotating the sample laterally. The sensitivities of the two configurations due to the structural parameters are discussed in details in the following sections.

For numerical analysis of the scattered far field intensity of the structure, a 3D finite difference time-domain (FDTD) model is built. The HG_{10} illumination source is generated through a self-written script, and its singularity line is tunable and rotatable. In simulations, the computational convergence must be satisfied to keep the validity, and the simulation will complete successfully and shut off automatically when convergence criteria are satisfied. In the model, a fine computing grid will ensure the accuracy of the results, but meanwhile introduce additional computations to increase the run time because a finer grid requires a smaller time step. To trade off the run time and computational precision, the grid size in the step structure region (made of silicon index of refraction $n = 3.882$ at 633 nm) is set as 2 nm in xy-plane and 5 nm in the z-direction. A perfect matching layer (PML) boundary condition is employed for all simulations. To obtain a signal that is very sensitive to the structure, a split-detector aligned with its split line along the y direction is implemented here by integrating the intensities from each half of the split detector and subtracting them.

5.3. THE SCATTERED FIELD FOR DIFFERENT STRUCTURE HEIGHTS

In our previous works [36, 37], we have focused on the SWA measurements under the assumption that the height of the step-shaped structure is already known. However, in a more general case, both parameters are not known, thus we need to figure out the effects of both parameters on the scattered far-field intensity. To reveal the effect of the height of structure, Figure 5.3 presents the intensity profiles of the back-scattered field in the back focal plane of the objective at three different heights of 0 nm, 80 nm ($\approx \lambda/8$), and 160 nm ($\approx \lambda/4$). The SWA is set to be 90° in all cases. The upper row in Figure 5.3 is measured in the parallel configuration for the incident beam as indicated in Figure 5.1(c), and the lower row is measured in the perpendicular configuration. The bold solid white line in the figure corresponds to the edge of the step structure.

As shown in Figs.5.3(a) and 5.3(d) at the height of 0 nm, the scattered fields are nearly the same, because the incident beam is just reflected by a flat surface and thus the profile

is similar to the HG_{10} beam shown in Figure 5.2(a). With an increased height of the step-structure, as shown from Figure 5.3(a) to 5.3(c), the scattered intensity in the left hemisphere becomes weaker while the right lobe gradually moves to the center. In Figure 5.3(c), the scattered field with a bright spot in the center is very similar to a Gaussian beam, mainly because the phase difference of the reflected light introduced by the height of 160 nm is around π, which nicely compensates the inherent π-phase jump of HG_{10} beam as shown in Figure 5.2. Similarly, for the perpendicular configuration in Figure 5.3(d) to 5.3(f), the main lobes of the scattered field gradually move to the upper hemisphere, and another dark line is formed along the horizontal direction with the increase of height. As shown in Figure 5.3(f), the horizontal dark line caused by the sample is perpendicular to the singularity line of HG_{10} beam, and divides the scattered field into four quadrants. Notably, the far-field intensity distribution of the scattering field strongly depends on the height of the step, hence providing an alternative approach for retrieving the value of the height of the structure.
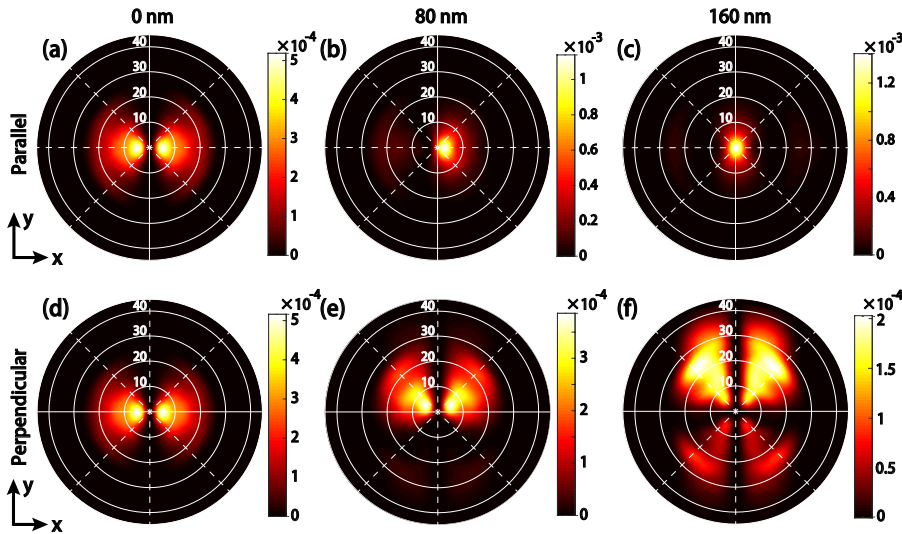
Figure 5.3: The far-field intensity distributions at the back focal plane of the objective when a HG beam is focused on a step (silicon) with variable height and fixed SWA = 90°. The upper (a-c) and lower (d-f) rows are simulated when the singularity line is parallel and perpendicular to the step (shown as a white line in the plots), respectively. The three columns correspond to three different structure heights: 0 nm, 80 nm, and 160 nm. The wavelength is 633 nm and the numerical aperture is 0.6.

5.4. SIMULTANEOUS DETECTION OF HEIGHT AND SWA

To quantify the discernibility of the configuration, the scattered signal in the far-field is divided into the left and right halves for split detection, with the split line of the split detector parallel to the step structure in accordance with Figure 5.3. The split detection

signal is obtained by integrating the intensity on both halves of the split detector and subtracting them. The signal is then normalized by the total intensity (i.e., the sum of the intensities of both halves of the split detector).

5.4.1. THE DETERMINATION OF HEIGHT

Several Height-SWA combinations are investigated by sweeping the height from 0 nm to 400 nm and SWA from 80° to 90°, in parallel and perpendicular configuration, as shown in Figures 5.4(a) and 5.4(b), respectively. The results indicate that the height of the structure has a dominating influence in the value of the split detection signal, while the SWA makes a minor impact.
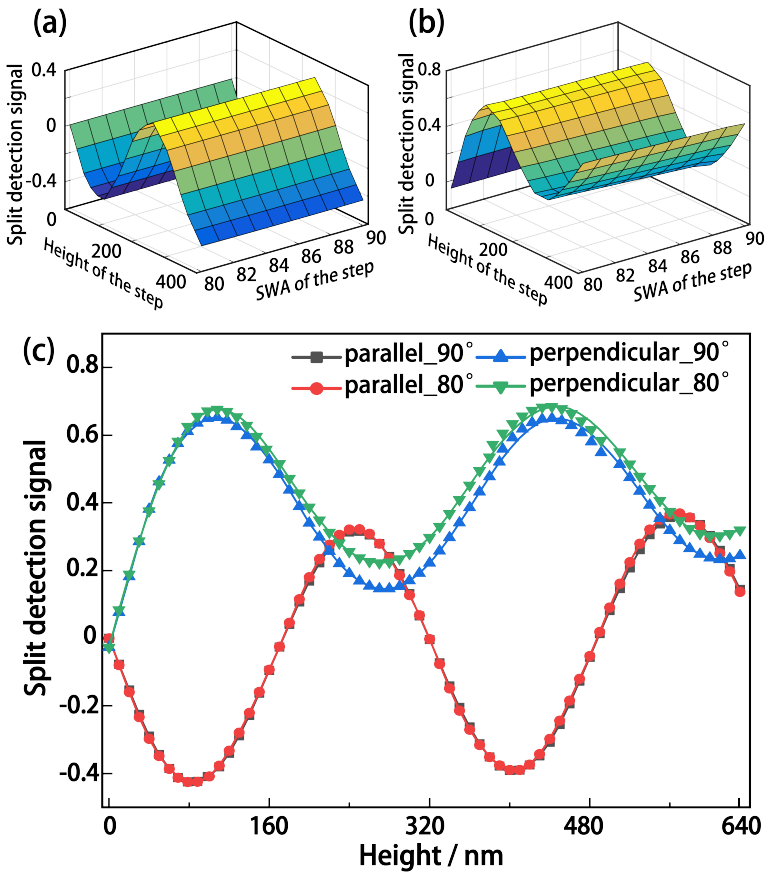
Figure 5.4: The split detection analysis for different Height-SWA combinations. 3D view of the split detection signals by sweeping both the height and the SWA of the structure in parallel (a) and perpendicular (b) configuration, respectively. Both the scale and color represent the value of split detection signal. (c) Larger region and higher precision height sweeping with SWAs of 80° and 90° in both configurations. Note that the black and red curves almost overlap everywhere.

For further confirmation of the different roles of the two parameters, a more accurate sweeping is carried out for both configurations as depicted in Figure 5.4(c). Here, the value of height is swept from 0 nm to 630 nm in both configurations, and two typical SWAs (80° and 90°) are selected for comparison. Black and red curves in the parallel configuration highly coincided in the entire range, proving that the effect of SWAs is negligible in this case. In this configuration, the changes in the split detector value are more sensitive for changes in the height of the structure, so the split detection signal can be used for accurate determination of the height.

On the contrary, the blue and green curves (corresponding to two different SWA in the perpendicular configuration) are highly coincided when the height is below 100 nm, but show differences with increasing height. The difference is much bigger around the height of 280 nm and 590 nm, corresponding to the valley of the curves. Compared to the parallel case, the perpendicular configuration shows a better performance on the discrimination of SWAs. Although in Figure 5.4(c) the effect of height is quasi-periodic in all curves, accurate height value of the structure can still be determined based on the combined results of the two configurations.

5.4.2. The determination of SWA
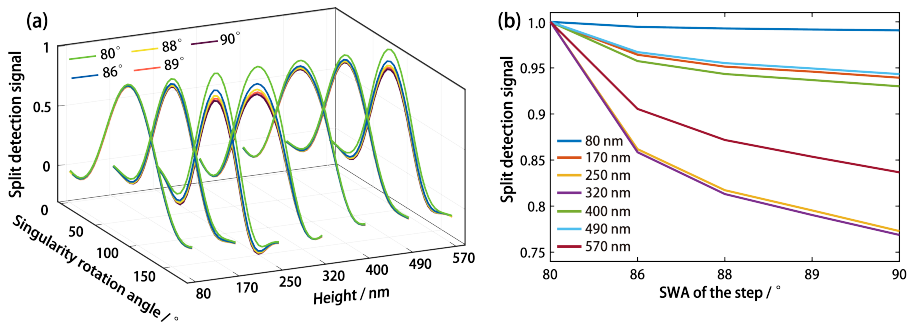
Figure 5.5: (a) The split detection signals as a function of the rotation angle for five SWAs and seven different heights. The signal is generated by rotating the singularity from 0° to 180°, of which the 0° and 180° rotation angles correspond to the parallel configuration, and the center rotation angle (90°) corresponds to the perpendicular one. (b) The normalized split detection signal in perpendicular mode as a function of the SWA for different structure heights.

With calibrated heights of the nanostructure, Figure 5.5 shows quantitative comparisons of the split detector signals for five SWAs at different heights. The position of the sample is fixed and the singularity line of the incident beam is rotated from 0° to 180°, i.e., from the parallel to the perpendicular configuration and finally back to the parallel situation. For every height, the signal is plotted as function of the rotation angle for five values of the SWA, and the signals for five different SWAs are self-normalized by the maximum value. The difference within each set of curves in Figure 5.5(a) gives the index to evaluate the distinguish capability of the singular beam. It is clear that the signals for SWAs of

$\theta = 80°$ and $90°$ are the top curve and the bottom curve, respectively, and the peaks of different values of the detected signals for various SWAs are obtained at the perpendicular mode when rotating the singularity direction of the singular beam. To clearly compare the distinguishing capability at the perpendicular mode, we plot in Figure 5.5(b) the normalized split detection signal as a function of the SWA for different heights. For a certain height, the difference value compared to the reference point (SWA= 80°) shows a monotone variation, and for each SWA, a unique split detection signal is obtained. Consequently, the perpendicular mode is capable of determining the SWAs. The slope of the curve can be used to quantify the accuracy. One notices also that it is easier to determine the SWA when the step is not very shallow.

5.5. DISCUSSIONS AND CONCLUSIONS

From the results of the perpendicular case in Figure 5.4(c), one can achieve a comprehensive understanding of the dependence of the signal on the height variations. The differences between curves for SWA of $80°$ and $90°$ are more pronounced within a certain height interval (close to integer multiples of the half-wavelength), as there then exists a π phase difference on both sides of the singularity line. This reveals that the SWAs can be better distinguished in these height intervals than for others. It should be noted that the lateral shadow of the step-structure with low height is ultra-small. For instance, the shadow difference between $89°$ and $90°$ is only 1.4 nm for the height of 80 nm, which is an extremely tiny value to be distinguished. Consequently, the five curves are highly coincident at the height $h = 80$ nm, indicating that it is still a challenge for the proposed method to distinguish the SWAs in the case of shallow steps.

Based on the above analysis, the height can be calibrated with high accuracy without the influence of SWA in the parallel configuration. By rotating the singularity line in a suitable height interval, our method can be successfully used to distinguish steep SWAs. Ultimately, with a combination of the above two processes, e.g., focusing the singularity line along the step-structure and rotating the singularity line, both the height and SWA of the structure can be retrieved simultaneously. Moreover, the mechanical vibrations can be effectively evaded by just rotating the singularity line of the incident beam. The rotation allows disambiguation and decoupling of the experimental signal from the effect of experimental noise by allowing for multiple measurements, which helps to improve the measurement accuracy. This is a great improvement compared with previous works.

The sample that occurs in practice often includes steps of which the left and right part consist of different material. Due to the different scattering and reflection efficiency of the two materials, the intensity and phase shift between the two regions will be changed and will affect the intensity contrast. Moreover, most functional structures are constituted by combining monomer units, where the boundary conditions are periodic. For this case, the numerical effort will open a new window for the CFS modelling. These are very valuable and meaningful subjects for accurate nanoscale detection in practical applications.

In conclusion, we employed a HG_{10} mode singular beam to combine with the conventional CFS system to retrieve the geometrical parameters of structures that are commonly used in the semiconductor industry. For simplicity but without loss of generality, a step-shaped structure with an invariant y-axis is selected as the sample. Using our method,

it is possible to determine both the height and the SWA of the structure simultaneously by rotating the singularity direction of HG_{10} beam and measuring the far field with a split detector. This provides a much simpler and more robust approach than the raster scanning method in conventional CFS. When the singularity is parallel to the invariant axis of the sample, the height can be accurately detected regardless of the value of the SWA. By rotating the angle of the singularity line of the singular beam w.r.t. the direction of the edge of the structure, one can retrieve the SWA with high accuracy in a suitable height interval. The proposed method can work under wide conditions, and is not limited to step-structures. The same approach applies to more varied materials, structures, wavelengths, etc., and these will be further discussed in the following research. Given that the height interval where the sensitivity is high depends on the wavelength, one can tailor the sensitivity region by varying the wavelength of the illumination. This work will open up new opportunities for precision measurements in the semiconductor industry.

REFERENCES

[1] **X. Dou**, C. Min, Y. Zhang, S. F. Pereira, and X. Yuan. "Optical singularity assisted method for accurate parameter detection of step-shaped nanostructure in coherent Fourier scatterometry". In: *Optics Express* 30.16 (2022), pp. 29287–29294.

[2] H. Wang and M. L. Gee. "AFM lateral force calibration for an integrated probe using a calibration grating". In: *Ultramicroscopy* 136 (2014), pp. 193–200.

[3] N. Jalili and K. Laxminarayana. "A review of atomic force microscopy imaging systems: application to molecular metrology and biological sciences". In: *Mechatronics* 14.8 (2004), pp. 907–945.

[4] O. Jusko, X. Zhao, H. Wolff, and G. Wilkening. "Design and three dimensional calibration of a measuring scanning tunneling microscope for metrological applications". In: *Review of scientific instruments* 65.8 (1994), pp. 2514–2518.

[5] G. Dai, M. Heidelmann, C. Kübel, R. Prang, J. Fluegge, and H. Bosse. "Reference nano-dimensional metrology by scanning transmission electron microscopy". In: *Measurement Science and Technology* 24.8 (2013), p. 085001.

[6] C. G. Frase, E. Buhr, and K. Dirscherl. "CD characterization of nanostructures in SEM metrology". In: *Measurement Science and Technology* 18.2 (2007), p. 510.

[7] C. Raymond. "Overview of scatterometry applications in high volume silicon manufacturing". In: *AIP Conference Proceedings*. Vol. 788. 1. American Institute of Physics. 2005, pp. 394–402.

[8] M. H. Madsen and P.-E. Hansen. "Scatterometry—fast and robust measurements of nano-textured surfaces". In: *Surface Topography: Metrology and Properties* 4.2 (2016), p. 023003.

[9] H. Gross, S. Heidenreich, M.-A. Henn, G. Dai, F. Scholze, and M. Bär. "Modelling line edge roughness in periodic line-space structures by Fourier optics to improve scatterometry". In: *Journal of the European Optical Society-Rapid publications* 9 (2014).

[10] P. Petrik, N. Kumar, M. Fried, B. Fodor, G. Juhász, S. F. Pereira, S. Burger, and H. P. Ur-
      bach. "Fourier ellipsometry–an ellipsometric approach to Fourier scatterometry".
      In: *Journal of the European Optical Society-Rapid publications* 10 (2015).

[11] V. Ferreras Paz, S. Peterhänsel, K. Frenner, and W. Osten. "Solving the inverse grating
      problem by white light interference Fourier scatterometry". In: *Light: Science &
      Applications* 1.11 (2012), e36–e36.

[12] O. El Gawhary, N. Kumar, S. F. Pereira, W. Coene, and H. P. Urbach. "Perfor-
      mance analysis of coherent optical scatterometry". In: *Applied Physics B* 105 (2011),
      pp. 775–781.

[13] N. Kumar, P. Petrik, G. K. Ramanandan, O. El Gawhary, S. Roy, S. F. Pereira, W. M.
      Coene, and H. P. Urbach. "Reconstruction of sub-wavelength features and nano-
      positioning of gratings using coherent Fourier scatterometry". In: *Optics express*
      22.20 (2014), pp. 24678–24688.

[14] B. Wang, M. Tanksalvala, Z. Zhang, Y. Esashi, N. W. Jenkins, M. M. Murnane, H. C.
      Kapteyn, and C.-T. Liao. "Coherent Fourier scatterometry using orbital angular
      momentum beams for defect detection". In: *Optics Express* 29.3 (2021), pp. 3342–
      3358.

[15] D. Kolenov, I. E. Zadeh, R. C. Horsten, and S. F. Pereira. "Direct detection of
      polystyrene equivalent nanoparticles with a diameter of 21 nm (λ/19) using
      coherent Fourier scatterometry". In: *Optics Express* 29.11 (2021), pp. 16487–16505.

[16] S. Roy, A. C. Assafrao, S. F. Pereira, and H. P. Urbach. "Coherent Fourier scatterome-
      try for detection of nanometer-sized particles on a planar substrate surface". In:
      Optics express 22.11 (2014), pp. 13250–13262.

[17] A. Forbes, M. de Oliveira, and M. R. Dennis. "Structured light". In: *Nature Photonics*
      15.4 (2021), pp. 253–262.

[18] Y. Yang, Y.-X. Ren, M. Chen, Y. Arita, and C. Rosales-Guzmán. "Optical trapping with
      structured light: a review". In: *Advanced Photonics* 3.3 (2021), pp. 034001–034001.

[19] H. Rubinsztein-Dunlop, A. Forbes, M. V. Berry, M. R. Dennis, D. L. Andrews, M.
      Mansuripur, C. Denz, C. Alpmann, P. Banzer, T. Bauer, *et al.* "Roadmap on struc-
      tured light". In: *Journal of Optics* 19.1 (2016), p. 013001.

[20] M. R. Dennis, K. O'holleran, and M. J. Padgett. "Singular optics: optical vortices and
      polarization singularities". In: *Progress in optics*. Vol. 53. Elsevier, 2009, pp. 293–363.

[21] D. Mao, Y. Zheng, C. Zeng, H. Lu, C. Wang, H. Zhang, W. Zhang, T. Mei, and J. Zhao.
      "Generation of polarization and phase singular beams in fibers and fiber lasers".
      In: *Advanced Photonics* 3.1 (2021), pp. 014002–014002.

[22] B. Spektor, A. Normatov, and J. Shamir. "Singular beam microscopy". In: *Applied
      optics* 47.4 (2008), A78–A87.

[23] G. H. Yuan and N. I. Zheludev. "Detecting nanometric displacements with optical
      ruler metrology". In: *Science* 364.6442 (2019), pp. 771–775.

[24] W. Wang, T. Yokozeki, R. Ishijima, A. Wada, Y. Miyamoto, M. Takeda, and S. G.
      Hanson. "Optical vortex metrology for nanometric speckle displacement measure-
      ment". In: *Optics express* 14.1 (2006), pp. 120–127.

[25] Z. Xi, L. Wei, A. J. L. Adam, H. P. Urbach, and L. Du. "Accurate feeding of nanoantenna by singular optics for nanoscale translational and rotational displacement sensing". In: *Physical Review Letters* 117.11 (2016), p. 113903.

[26] M. Gödecke, S. Peterhänsel, D. Buchta, K. Frenner, and W. Osten. "Detection of grating asymmetries by phase-structured illumination". In: *Fifth International Conference on Optical and Photonics Engineering*. Vol. 10449. SPIE. 2017, pp. 61–68.

[27] A. Faridian, V. F. Paz, K. Frenner, G. Pedrini, A. D. Boef, and W. Osten. "Phase-sensitive structured illumination to detect nanosized asymmetries in silicon trenches". In: *Journal of Micro/Nanolithography, MEMS, and MOEMS* 14.2 (2015), pp. 021104–021104.

[28] E. Hemo, B. Spektor, and J. Shamir. "Scattering of singular beams by subwavelength objects". In: *Applied Optics* 50.1 (2011), pp. 33–42.

[29] J. Shamir. "Singular beams in metrology and nanotechnology". In: *Optical Engineering* 51.7 (2012), pp. 073605–073605.

[30] **X. Dou**, A. Yang, C. Min, L. Du, Y. Zhang, X. Weng, and X. Yuan. "Polarization-controlled gap-mode surface-enhanced Raman scattering with a single nanoparticle". In: *Journal of Physics D: Applied Physics* 50.25 (2017), p. 255302.

[31] X. Weng, L. Du, A. Yang, C. Min, and X. Yuan. "Generating arbitrary order cylindrical vector beams with inherent transform mechanism". In: *IEEE Photonics Journal* 9.1 (2017), pp. 1–8.

[32] T. Zang, H. Zang, Z. Xi, J. Du, H. Wang, Y. Lu, and P. Wang. "Asymmetric excitation of surface plasmon polaritons via paired slot antennas for angstrom displacement sensing". In: *Physical Review Letters* 124.24 (2020), p. 243901.

[33] J. Lin, O. Rodrıguez-Herrera, F. Kenny, D. Lara, and J. Dainty. "Fast vectorial calculation of the volumetric focused field distribution by using a three-dimensional Fourier transform". In: *Optics express* 20.2 (2012), pp. 1060–1069.

[34] M. Leutenegger, R. Rao, R. A. Leitgeb, and T. Lasser. "Fast focus field calculations". In: *Optics express* 14.23 (2006), pp. 11277–11291.

[35] B. Richards and E. Wolf. "Electromagnetic diffraction in optical systems, II. Structure of the image field in an aplanatic system". In: *Proceedings of the Royal Society of London. Series A. Mathematical and Physical Sciences* 253.1274 (1959), pp. 358–379.

[36] **X. Dou**, S. F. Pereira, C. Min, Y. Zhang, P. Meng, H. P. Urbach, and X. Yuan. "Determination of steep sidewall angle using polarization-sensitive asymmetric scattering". In: *Measurement Science and Technology* 32.8 (2021), p. 085201.

[37] L. Cisotto, S. F. Pereira, and H. P. Urbach. "Analytical calculation on the determination of steep side wall angles from far field measurements". In: *Journal of Optics* 20.6 (2018), p. 065601.

6

TRANSVERSAL OPTICAL SINGULARITY INDUCED PRECISION MEASUREMENT OF STEP-SHAPED NANOSTRUCTURE

Optical singularity indicates zero-intensity point in space where parameters, such as phase, and polarization, are undetermined. In the case of a transversal optical singularity (TOS), the latter occurs perpendicular to the direction of propagation, and its phase integral is a positive or negative 2π in nature. Since it occurs within a nano-size range, one expects that TOSs could be sensitive to the light-matter interaction process and could provide a great possibility for accurate determination of certain parameters of nanostructure. In this chapter, we propose to use TOSs generated by a three-wave interference to illuminate a step nanostructure. After interaction with the nanostructure, the TOS is scattered into the far field. The scattering direction can have a relation with the physical parameters of the nanostructure. We show that by monitoring the spatial coordinates of the scattered TOS, its propagation direction can be determined, and as consequence, certain physical parameters of the step nanostructure can be retrieved with high precision.

6.1. INTRODUCTION

With continuing miniaturization and intelligence of optoelectronic devices and the explosive demand of the consumer market, the semiconductor industry advances towards higher-level products that need to be made with shrinking critical size and high volume, which also demonds higher requirements for metrology methods [2]. To ensure the functionality and yield of the semiconductor chips, quality assessment is always an important topic in the modern manufacturing industry. Optical scatterometry [3–5] has been used extensively in the manufacturing process, and it has shown sufficient robustness in the in-line process quality control and sufficient accuracy in critical dimension measurement.

For the next generation of lithography, in addition to the critical dimension of micro/nanostructures, more accurate measurements need to be executed to reduce the uncertainties of the determination of the side-wall angle (SWA), the surface roughness and the left/right round corners of the nanostructures. Furthermore, we identified that SWA is one of the least predicable and controllable parameters in the chip manufacturing process. Quality assessment is still a very challenging and urgent matter. The conventional optical scatterometry usually uses the amplitude, the polarization and in some cases the phase characteristics of the scattered light to determinate the parameters of the target structure. However, with the further exploration of light properties, other characteristics such as singularity [6], orbital angular momentum [7], spin angular momentum [8] also show great potential to improve such parameter determination.

An optical singularity is a point where the amplitude of the field is zero and the phase undefined [9–12]. Close to the singularity there is a high gradient. There are two main forms of optical singularity: the polarization and phase versions. Both have been widely employed in many frontier research and application areas [13–16]. The polarization singularity, which appears widely in vector beams, has been demonstrated to achieve extreme sensitivity in detecting slight changes due to the interaction with (nano)objects [17, 18]. The phase singularity is ubiquitous in complex wave systems and occur at points where the amplitude of a field component vanishes.

In recent times, structured light has become synonymous with orbital angular momentum. The richness of the topic as well as its myriad of applications has seen it attract much attention. In optical vortex beams, the helical phase circulates around a zero-field point, thus generate an orbital angular momentum to form an optical phase singularity. The phase integration around an orbital angular momentum is an integer multiple of 2π, being known as the topological charge. Physically, the phase singularity can be divided into the longitudinal and transversal states, i.e., parallel and perpendicular to the direction of propagation, respectively. The longitudinal optical singularity possesses an arbitrary topological charge. The region around the optical singularity where the amplitude is very small, usually in the size of several wavelengths. Longitudinal optical singularity has been widely used in optical interconnection, computing, and optical manipulation areas [10, 19–21].

In the case of transversal optical singularity (TOS), however, the phase integration around the singularity is 2π. The above mentioned TOS is a property of a time harmonic beam without considering changes in the temporal domain. Very recently, the generation of light with spatiotemporal TOS has been demonstrated both in theory and experiment [22–27]. It provides an additional temporal freedom, which it is expected to have impact

in frontier research. It has been shown that TOS occurs at the nodal lines with complete destructive interference as for example edge diffraction [28], interference of Gaussian beams [29], under highly focusing condition [30], or multiple plane waves overlapping in space [31–33].

In this chapter, we employ three linearly polarized Gaussian waves with intersection angle of 0° and ±45° to generate an array of TOS in the interference region. After the interaction with the step nanostructure, the scattering field also contains phase singularity which is detectable in the far field. We have seen that the scattering direction of the TOS depends highly on the parameters of the step-structure. By detecting the scattering angle of the scattered TOS, the height and SWA of the structure can be reconstructed with high precision. The numerical results demonstrate that this is an efficient and sensitive method, and it provides a good complement to coherent Fourier scatterometry technique for finer measurements of nanostructures.

6.2. METHODOLOGY

6.2.1. THE GENERATION OF DESIRED BEAM

It has been demonstrated that three plane waves are sufficient to produce transversal phase singularity [34–36]. The three-wave interference always results in an array of vortices, as long as the sum of the two smallest phasors exceeds the amplitude of the largest one. Here, without loss of generality, we consider the generation of TOSs by three Gaussian beams interference, where the beams have equal amplitude and the same polarization direction, i.e., the y-axis direction in our case.
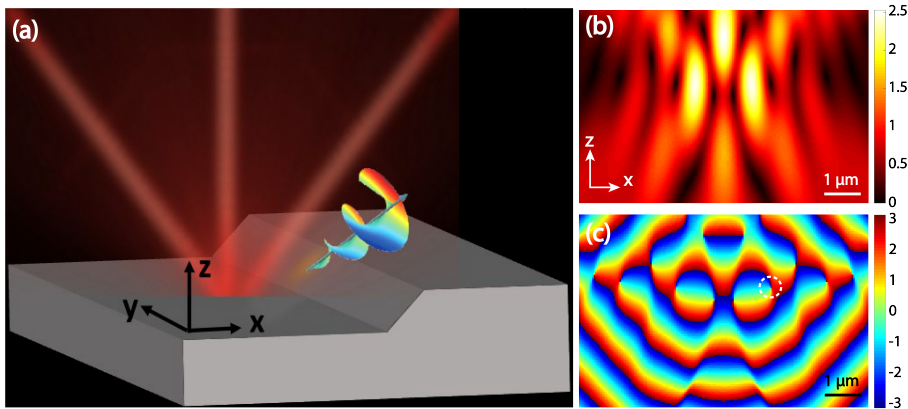
Figure 6.1: (a) Schematic of the TOS generation and its interaction with the silicon-based step nanostructure. The wavelength of the incident beam is 633 nm. (b) and (c) are the intensity and phase distribution of the interference field in a free space.

The wavelength of the incident Gaussian waves is chosen at 633 nm and their propagation angles are set as 0° and ±45° with z-axis, respectively. The three Gaussian waves are all placed in the xz-plane and symmetric with the z-axis (see Figure 6.1(a)), with waist radius of 1.02 μm, equivalent to the case of a focused beam with NA of 0.2. The interference

field forms an array of TOSs. As the three waves are distributed symmetrically with z-axis, the TOSs are also axially symmetric. Figure 6.1(b) and 6.1(c) are the field intensity and phase distribution of the interference field, respectively. TOSs are essentially the same in physical properties, under the condition of neglecting the absolute positive and negative value of its topolotical charge. Hereinafter, we will focus on a randomly selected TOS (labeled in Figure 6.1(c) by a blue circle) to investigate its changes after interacting with the structure. Here, we chose the 633 nm wavelength source, because it is a visible light and has widely been used in scatterometry for nanostructure reconstruction in many inspection systems in current semiconductor industry.

6.2.2. TWO FACTORS INFLUENCING THE DESIRED BEAM

The physical characteristics of the optical field depends on the illumination, and the spatial distribution of the TOSs will change if the illumination sources are changed. The distribution of the TOSs can be modulated by the wavelength and the angle of the incident waves. The influences of these two factors will be discussed in the following.
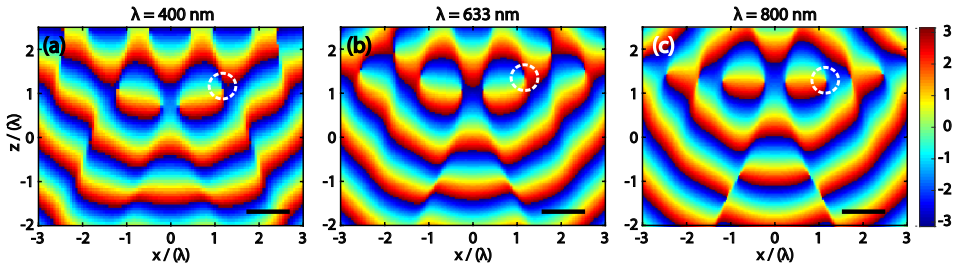
Figure 6.2: Generation of TOS field with 400 nm, 633 nm and 800 nm, for interfering beams incident under the angles of 0° and ±45°.

As the characteristic of TOS is indistinctive in physics, it can be reasonably inferred that its scattering behavior follows similar pattern and it is scalable in a wide range of wavelengths. Figure 6.2 depicts the phase distribution of the TOS field with three different wavelengths, proving that the generation of TOSs is universal. It should be noted that, some typical features, e.g., the position of the TOS, is closely related to the wavelength. Consequently, for other wavelengths, the only issue is that the relative position between the source and step structure should be changed according to the wavelength, to make sure that the TOS can interact with the sample structure.

In experiments, the incident angles of the beams may be slightly deviate. Therefore we need also to study its influence on the TOS field. Figure 6.3 depicts the phase distribution of the interference field when the illuminating angle from the two sides rotates with a small angle (from ±45° to −43° and 47◦). It shows that spatial position of the TOS (indicated by blue circle) shifts slightly, but without obvious change in phase distribution around the blue circles.

A 3D finite-different time-domain (FDTD) model is built for numerical analysis from a commercial FDTD solver (Lumerical FDTD solutions 2020 R2.4). The material of the step structure is set as silicon, the input medium is air, their material index are default values
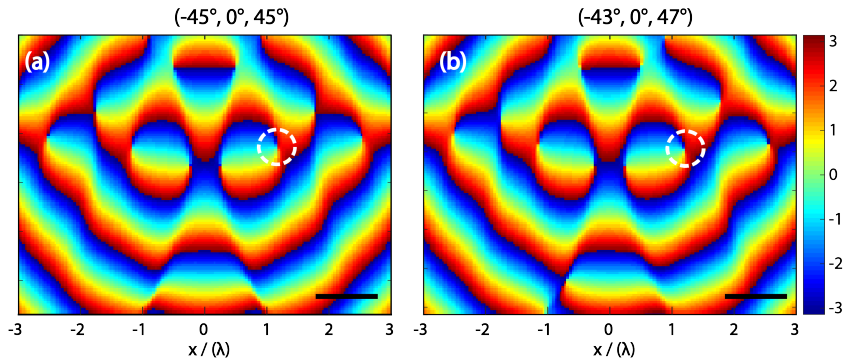
Figure 6.3: Comparison of the phase distribution of the interference field generated by three beams with different incident angles. The top numbers denote the incident angles of the three incident beams. The wavelength is 633 nm.

given in the Material Library. The wavelength of the three incident Gaussian beams is 633 nm, and they are also the built-in source in the solver, which are typically linearly polarized. Both the propagation direction and the waist of the Gaussian beam can be modified by the user. The adjustment of the propagation direction of three Gaussian beams can control the spatial location of the singularity, and the setting of the waist is equivalent to changing of the NA of the objective to alter the focusing conditions. As a TOS is always distributed within a nanoscale range, the calculating resolution should be fine enough to ensure the final accuracy. The grid size in the step structure region is therefore set as 5 nm in xy-plane and 2 nm in z-direction. In the other computational region, the grid size is uniformly set as 25 nm in three directions. Finally, a perfect matching layer (PML) boundary condition is employed for all simulations.

6.2.3. THE DETECTION APPROACH

POSITION CALIBRATION BETWEEN TOS AND STRUCTURE

When the beam is focused on a flat substrate, the original interference field will be redistributed due to the influence of the substrate, as shown in Figure 6.4(a) and (b). The coordinate of the selected TOS in Figure 6.4(b) needs to be extracted to ensure that the step structure can be accurately placed on this position. The intensity and phase distribution in the plane $y = 0$ for the interaction between TOS field and the step nanostructure are depicted in Figure 6.4(c) and 6.4(d), respectively. Figure 6.4(d) indicates that the selected TOS will interact with the step nanostructure. In the interaction process, the original localized TOSs will be scattered into the far field, keeping its topological charge valid in the scattering process [37–39].It needs a certain propagation distance to retrieve the scattered TOS, thus no TOS is retrieved in Figure 6.4(d) (Figure 6.4(d) is the phase pattern in the plane $y = 0$). The position of the scattered TOS is highly dependent on the physical properties of the step structure. Detecting this position of the scattered TOS can be an alternative approach to retrieve the parameters of the step, which in our case are its height and SWA. Naturally, the scattered field we are interested in is the differences

between the optical field with a step nanostructure and with a flat substrate. The position of the scattered TOS is determined by monitoring the spatial coordinates of the phase singularity.
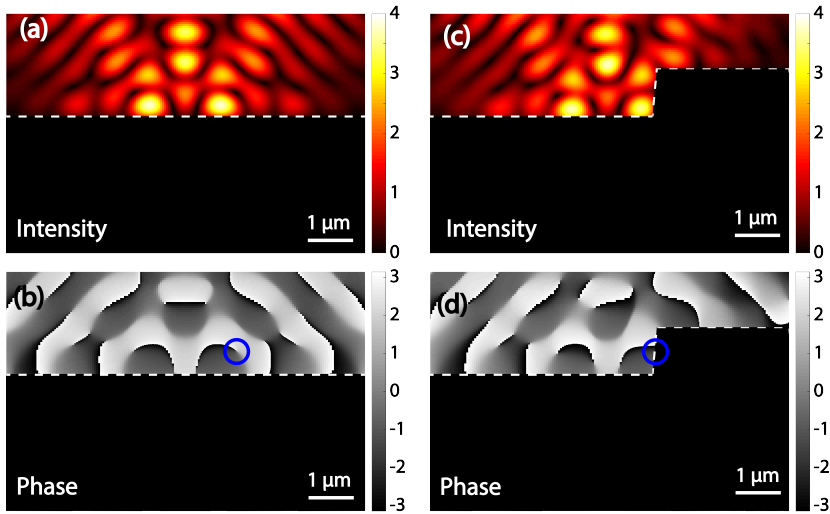

Figure 6.4: Scheme of the TOS induced precise detection. (a) and (c) are the total field after interaction with the flat substrate and the step-structure. (b) and (d) are the phase distribution of the fields corresponding to (a) and (c). The position of the generated TOS is marked by a blue circle. (d) indicates that the TOS interacts with the edge of the step nanostructure.

When interaction occurs between the TOS and the step nanostructure, the original TOS will be scattered into the far field at a specific scattering direction. As the TOS possesses a spiral phase around the singularity in xz-plane, the spatial position of the scattered TOS can be determined by the interference field of the scattered field and a reference field. By varying the y-value along the y-axis and recording the spatial position of the TOS at corresponding xz-planes, its three-dimensional propagation trajectory line can be achieved. On this basis, the scattering direction can be retrieved by fitting a straight line with the spatial coordinates of TOSs. The slope of the fitting line refers to the scattered direction of the TOS, which directly reflects parameters of the step structure.

The trajectory of scattered TOS

Given the geometry of the model, the scattering is symmetric with respect to the y-coordinate. Without loss of generality here, we focus on the positive y-axis. To reduce disturbance, the spatial position of the optical source and structure are both fixed in the following analysis. Figure 6.5(a) shows the process to obtain the trajectory line of the scattered TOS as function of y. The spatial location of the scattered TOS is determined by the spiral-shaped phase distribution in different cross sections along the y-axis. The yellow circles in the profiles denote the retrieved TOS. By connecting the location of the

TOS in each plane, we can obtain its scattering trajectory line. Figure 6.5(b) shows the trajectories of the scattered TOS with fixed height (633 nm) for various SWAs. As the legends indicate, the yellow line for SWA= 82°, the blue line for 85°, and the red one for 88°. It is obvious that SWAs can influence the location of scattered TOS and further change its spatial trajectory, in other words, the trajectory line is closely related to the value of the SWA.

In addition to the SWA, the step height also give rise to changes in propagation direction of the scattered TOS. Figure 6.5(c) shows the trajectory line of the scattered TOS for different step heights when the SWA is fixed to 85°. In the cross-section of $y = 2.0 \mu m$, the positions of the scattered TOS for these three heights (675 nm/ 633 nm/ 600 nm) almost coincide. For the $y = 2.5$ and 3.0 μm plane, the singularity positions are dispersed. Likewise, the trajectory line of the scattered TOSs is then achieved by connecting the location of TOS in each plane. It is clear from these results that the trajectory line shows visible difference in these three cases, which means that the trajectory line is also sensitive to the height of step. We also find that the trajectory line changes fastest along the y-axis, followed by the x-axis, and z-axis, so the change of the trajectory line in xy-plane should be the most obvious one to be considered.
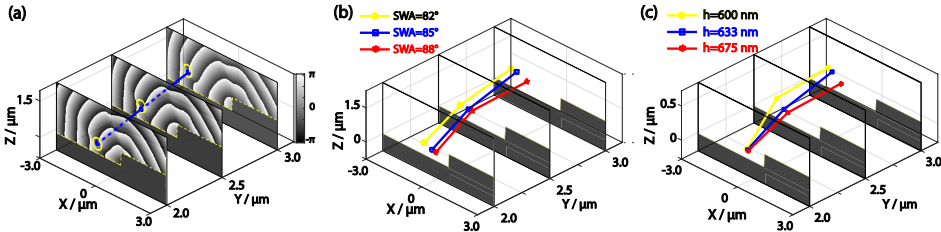
Figure 6.5: Spatial trajectory line of scattered TOS by a step nanostructure with different geometrical parameters. (a) The process of tracking the scattered TOS. The trajectory line of the scattered TOS is built by connecting all the position makers along the y-axis. The bottom dark gray region indicates the step structure. (b) The scattered TOS trajectories with step height of 633 nm but various sidewall angles (SWAs). (c) The trajectory line of TOS scattered by the step nanostructure with different heights, while the SWA is 85° for all cases. The simulation results clearly show that the scattering trajectory line is highly dependent on both the height and SWAs.

THE SCATTERING ANGLE

By fitting a straight line with the spatial positions of the scattered TOSs, the slope of the line then reflects physical parameters of the step structure. In Figure 6.6, we do the same simulation with a larger calculating range of $\pm 10 \mu m$ along the y-axis, and show how to calculate the scattering angle in xy-plane. Figure 6.6(a) shows the spatial distribution of the scattered TOS in the xz-plane at different y-value. In 6.6(b), the x-coordinate of the retrieved TOS as function of y shows a good linear trajectory in this larger scale (more than 10 wavelengths), where the fitted trajectory line matches well with the retrieval points. This result supports the stability of our method. Consequently, the slope of the

fitted curves is calculated to get the scattering angles that characterize the directionality of the TOSs. Here, the scattering angle refers to the angle between the fitted straight line and the y-axis.
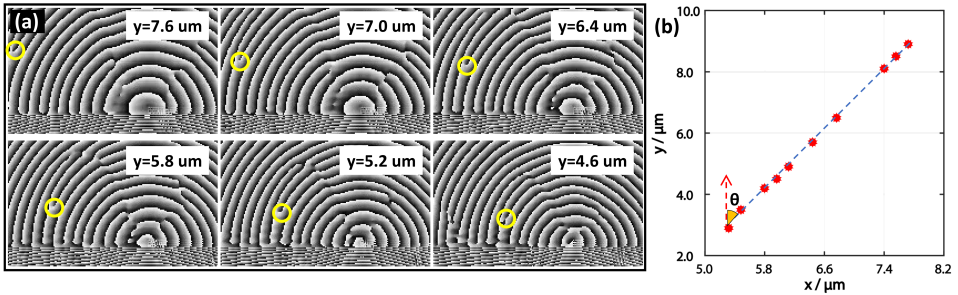

Figure 6.6: The spatial distribution of the scattered TOS. (a) The spatial distribution of the TOS, where the top-right label denotes the position in y-axis and the yellow circle denotes the position of the TOS. (b) The x-coordinate of the retrieved scattered TOS as function of y, where the red dots are the spatial position of the TOS, and the blue dashed line is the linear fit and the yellow sector is the scattering angle.

6.3. SIMULATION RESULTS

6.3.1. THE SCATTERING ANGLE IN THE xy-PLANE

To make a preliminary assessment of the dependence of the scattered TOS on the SWA and height of the step nanostructure in particular, the SWA and height are swept independently to analyze the scattered behavior of TOS in the xy-plane. In the retrieval of SWAs, the structure height is fixed as 633 nm, and the selected TOS is located at the middle of the oblique surface of the step. The SWA is swept from 81° to 89° with intervals of 1°, and the projection of the 3D trajectories on xy-plane and its fitting curve are plotted in Figure 6.7(a). Here, the fitting curves are nearly linear, which reveals that the scattered TOS possesses high directional property. Consequently, the slope of the fitted curves is calculated to get the scattering angles that characterize the directionality of the TOSs.

Figure 6.7(b) shows the distribution of the scattering angle for different SWAs. We find that different SWAs correspond to different scattering angles, where the maximum value appears at 85° for this condition. The variation range of the scattering angle is typically wider than 5°, which is large enough to be distinguished. For the retrieval of height, the SWA is fixed at 85°, and other eight heights are chosen around 633 nm. The selected TOS is still fixed at the middle of the step oblique surface when the height equals to 633 nm. Figure 6.7(c) and Figure 6.7(d) give the fitting curves and scattering angles for different heights, respectively. Like Figure 6.7(a) and Figure 6.7(b), the changes in height also influence the scattering angle. Each height can be encoded to one scattering angle, and the maximum value appears at 633 nm. Based on these results, one can safely conclude that the scattering direction is highly dependent on changes in SWA and height. In Figure 6.7(b) and (d), the scattering angles both show a tendency of first increasing and then

decreasing with respect to the changing of SWA/height, which shows that the relationship between the scattering angle and SWA/height is not unique. Consequently, only one scattering angle is not sufficient for unique detection.
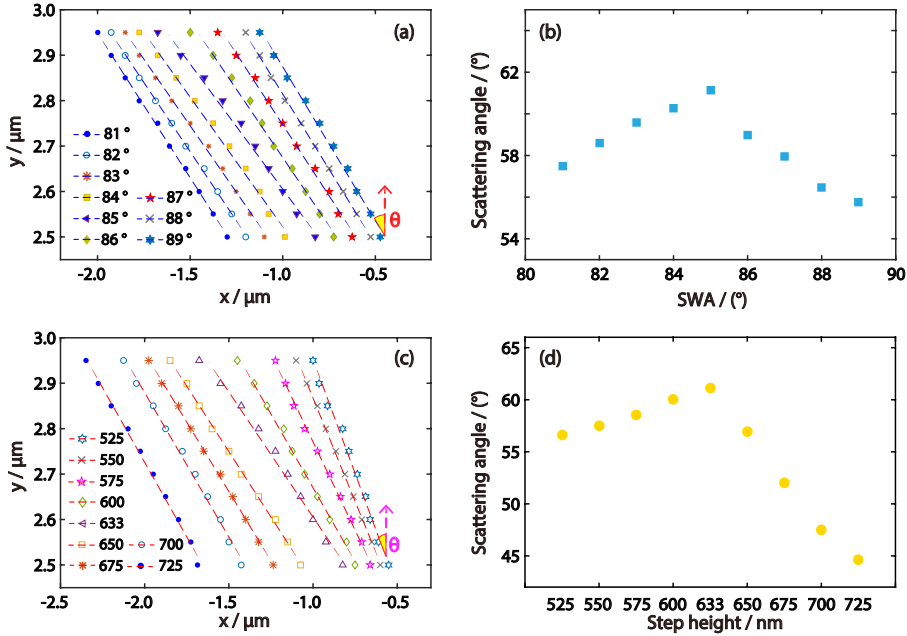

Figure 6.7: Properties of the scattered TOS against the height and steep SWA. (a) Recorded spatial position of scattered TOS in the xy-plane and the fitted lines for a 633 nm-height step with different SWAs. (b) Retrieved scattering angle of the scattered TOS to the y-axis corresponding to the SWAs shown in (a). (c) and (d) are the corresponding fitted lines and scattering angles for step-structure with different heights.

6.3.2. CONTRIBUTION OF SCATTERING ANGLES IN THREE DIFFERENT PLANES

As mentioned in Figure 6.5, the space curve of the TOS changes along all three axes, so it is easy to extend the scattering angle calculation onto the other two planes. Figure 6.8(a) plots the 3D trajectory line of the scattered TOSs, as well as their projection in three planes, for three different SWAs, namely 80°, 85°, and 89°. The height of the structure is still fixed as 633 nm, and the selected TOS is still located at the middle of the oblique surface, i.e., the same conditions as applied in Figure 6.7(a). It is apparent here that their projections in each plane possesses high directional property. The scattering angles in yz- and xz- plane are defined as the angles between the TOS propagation and the y-and z-axis, as the bright yellow triangles indicate. The data acquisition conditions for Figure 6.8(b) are the same as for Figure 6.7(c), which shows the 3D trajectories for three different heights, and the corresponding fitting lines in three projection planes.

Not only the scattering angles on the xy-plane, but also the scattering angles on the xz- and yz-planes show significant difference. Here we can conclude that the set of three scattering angles provides better possibilities to determine the structural parameters, which can help to overcome the non-uniqueness problem that follows from Figure 6.7 resulting in great potential in precision measurement.
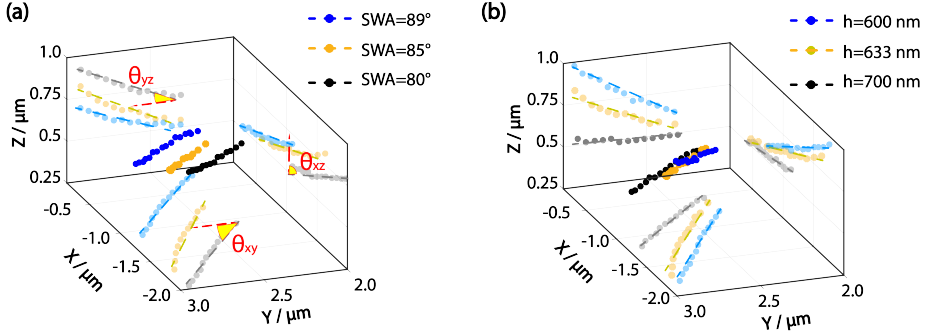
Figure 6.8: 3D trajectory line of the scattered TOS against the SWA and step height. (a) The height of the step is fixed at 633 nm, but the SWA varies. The scattering angle in each plane is presented by the bright yellow triangle. (b) The SWA is fixed at 85° with various heights. The trajectory line is projected onto xy-, xz-, and yz-planes, and the fitted curves in each plane exhibit high linearity characteristic.

6
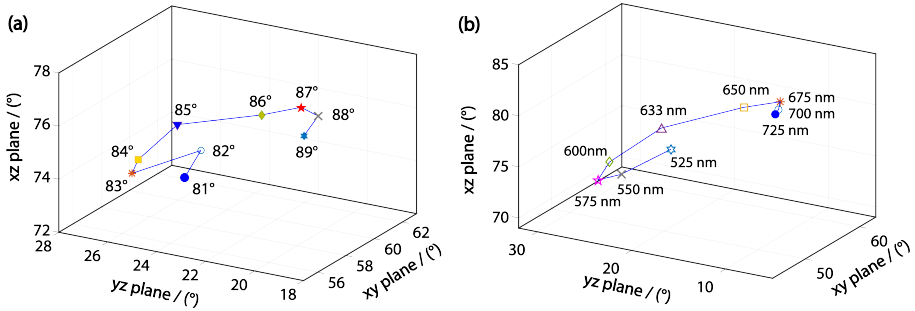
Figure 6.9: The unique retrieval of SWA and height of the step structure by using three scattering angle projections. (a) retrieval of the SWA. (b) retrieval of the height.

Finally, Figure 6.9 shows the 3D distribution of the scattering angles of the TOSs for step nanostructure with varying parameters. Figure 6.9(a) depicts the spatial position governed by three scattering angles for different SWAs, and Figure 6.9(b) plots the results for different heights. It demonstrates that the scattering angle possesses a dispersed distribution in the 3D space, which means that the parameters of the step structure can be uniquely distinguished by the set of three scattering angles. The spatial distance between two adjacent parameters reflects the degree of discrimination between them. For angle measurement techniques, the distance is large enough to distinguish the difference

in the nanostructure parameters.

Since the scattering angle is sensitive to both height and SWA, we need to build a data library of various SWA-height combination. For each SWA-height combination, there will be a unique set of scattering angles (as shown in Figure 6.9(a) and Figure 6.9(b)) corresponding to a certain structure. Angle measurement methods are very mature, and it is easy to realize a measurement accuracy up to 1 arcsec [40]. Therefore, the TOS can be suitable for precision measurement of parameters of the step nanostructures.

6.4. DISCUSSIONS AND CONCLUSIONS

It should be pointed out that since the illuminated area is very small on the sample, roughness should not be a big issue if one considers high quality printed nanostructures. In previous work of one of the authors [41], they have demonstrated that it is possible to acquire the optical field data that is reliable enough to reconstruct subwavelength features of gratings without considering roughness in the simulations.

In the simulation scenario, the phase information is calculated directly, and the angle information can be obtained by fitting the spatial coordinates of the phase singularity. In experiments, realistically, the phase cannot be measured directly, but one can consider using a reference beam and measuring the intensity after interference [42–47]. Finally, it should be noted that the composite optical field is composed of the reflected and the scattered field after interaction between the source and the structure, and the TOS is included in the scattering component. To fetch this valuable information, a calibration measurement with a flat substrate is necessary to eliminate the impact of the reflected field. In experiments, this can be achieved by moving the sample to an area without any structure as the flat reference.

In conclusion, we propose a three-wave interference generated TOS method to retrieve the geometrical parameters of a step nanostructure. Without loss of generality, the step structure is invariant along the y-direction. After interaction with the step structure, the TOS is scattered into the far field, with specific angle depending on the parameters of the step. By detecting the spatial position of the scattered TOS, the scattering angles with the axes are achievable. With this method, it is possible to retrieve both the height and SWA of the structure with high precision. Furthermore, this TOS can also work under a strong focusing mode, which will help to improve the detection accuracy. The TOS, meanwhile, is not limited to the parameter retrieval as described here, but it is expected to play a role in many other broaden scenarios, such as ultra-sensitive sensing, information storage, etc.

REFERENCES

[1] **X. Dou**, J. Zhou, Y. Zhang, C. Min, S. F. Pereira, and X. Yuan. "Transversal optical singularity induced precision measurement of step-nanostructures". In: *Optics Express* 31.20 (2023), pp. 32840–32848.

[2] M. Neisser. "International roadmap for devices and systems lithography roadmap". In: *Journal of Micro/Nanopatterning, Materials, and Metrology* 20.4 (2021), pp. 044601–044601.

[3]   M. H. Madsen and P.-E. Hansen. "Scatterometry—fast and robust measurements of nano-textured surfaces". In: *Surface Topography: Metrology and Properties* 4.2 (2016), p. 023003.

[4]   C. J. Raymond, M. R. Murnane, S. L. Prins, S. Sohail, H. Naqvi, J. R. McNeil, and J. W. Hosch. "Multiparameter grating metrology using optical scatterometry". In: *Journal of Vacuum Science & Technology B: Microelectronics and Nanometer Structures Processing, Measurement, and Phenomena* 15.2 (1997), pp. 361–368.

[5]   O. El Gawhary, N. Kumar, S. F. Pereira, W. Coene, and H. P. Urbach. "Performance analysis of coherent optical scatterometry". In: *Applied Physics B* 105 (2011), pp. 775–781.

[6]   Z. Xi, L. Wei, A. J. L. Adam, H. P. Urbach, and L. Du. "Accurate feeding of nanoantenna by singular optics for nanoscale translational and rotational displacement sensing". In: *Physical Review Letters* 117.11 (2016), p. 113903.

[7]   B. Wang, M. Tanksalvala, Z. Zhang, Y. Esashi, N. W. Jenkins, M. M. Murnane, H. C. Kapteyn, and C.-T. Liao. "Coherent Fourier scatterometry using orbital angular momentum beams for defect detection". In: *Optics Express* 29.3 (2021), pp. 3342–3358.

[8]   Z. Xi and H. P. Urbach. "Retrieving the size of deep-subwavelength objects via tunable optical spin-orbit coupling". In: *Physical Review Letters* 120.25 (2018), p. 253901.

[9]   A. M. Yao and M. J. Padgett. "Orbital angular momentum: origins, behavior and applications". In: *Advances in optics and photonics* 3.2 (2011), pp. 161–204.

[10] Y. Shen, X. Wang, Z. Xie, C. Min, X. Fu, Q. Liu, M. Gong, and X. Yuan. "Optical vortices 30 years on: OAM manipulation from topological charge to multiple singularities". In: *Light: Science & Applications* 8.1 (2019), p. 90.

[11] T. Ozawa, H. M. Price, A. Amo, N. Goldman, M. Hafezi, L. Lu, M. C. Rechtsman, D. Schuster, J. Simon, O. Zilberberg, *et al.* "Topological photonics". In: *Reviews of Modern Physics* 91.1 (2019), p. 015006.

[12] Q. Zhan. "Cylindrical vector beams: from mathematical concepts to applications". In: *Advances in Optics and Photonics* 1.1 (2009), pp. 1–57.

[13] Y. Zhang, J. Shen, C. Min, Y. Jin, Y. Jiang, J. Liu, S. Zhu, Y. Sheng, A. V. Zayats, and X. Yuan. "Nonlinearity-induced multiplexed optical trapping and manipulation with femtosecond vector beams". In: *Nano letters* 18.9 (2018), pp. 5538–5543.

[14] T. Brunet, J.-L. Thomas, and R. Marchiano. "Transverse shift of helical beams and subdiffraction imaging". In: *Physical review letters* 105.3 (2010), p. 034301.

[15] D. Mao, Y. Zheng, C. Zeng, H. Lu, C. Wang, H. Zhang, W. Zhang, T. Mei, and J. Zhao. "Generation of polarization and phase singular beams in fibers and fiber lasers". In: *Advanced Photonics* 3.1 (2021), pp. 014002–014002.

[16] J. Chen, C. Wan, and Q. Zhan. "Engineering photonic angular momentum with structured light: a review". In: *Advanced Photonics* 3.6 (2021), pp. 064001–064001.

[17] M. Burresi, R. Engelen, A. Opheij, D. van Oosten, D. Mori, T. Baba, and L. Kuipers. "Observation of polarization singularities at the nanoscale". In: *Physical review letters* 102.3 (2009), p. 033902.

[18] H. Larocque, D. Sugic, D. Mortimer, A. J. Taylor, R. Fickler, R. W. Boyd, M. R. Dennis, and E. Karimi. "Reconstructing the topology of optical polarization knots". In: *Nature Physics* 14.11 (2018), pp. 1079–1082.

[19] J. Wang. "Advances in communications using optical vortices". In: *Photonics Research* 4.5 (2016), B14–B28.

[20] J. Wang. "High-dimensional orbital angular momentum comb". In: *Advanced Photonics* 4.5 (2022), p. 050501.

[21] D. G. Grier. "A revolution in optical manipulation". In: *nature* 424.6950 (2003), pp. 810–816.

[22] A. Chong, C. Wan, J. Chen, and Q. Zhan. "Generation of spatiotemporal optical vortices with controllable transverse orbital angular momentum". In: *Nature Photonics* 14.6 (2020), pp. 350–354.

[23] C. Wan, Q. Cao, J. Chen, A. Chong, and Q. Zhan. "Toroidal vortices of light". In: *Nature Photonics* 16.7 (2022), pp. 519–522.

[24] K. Y. Bliokh. "Spatiotemporal vortex pulses: angular momenta and spin-orbit interaction". In: *Physical Review Letters* 126.24 (2021), p. 243601.

[25] H. Wang, C. Guo, W. Jin, A. Y. Song, and S. Fan. "Engineering arbitrarily oriented spatiotemporal optical vortices using transmission nodal lines". In: *Optica* 8.7 (2021), pp. 966–971.

[26] G. Gui, N. J. Brooks, H. C. Kapteyn, M. M. Murnane, and C.-T. Liao. "Second-harmonic generation and the conservation of spatiotemporal orbital angular momentum of light". In: *Nature Photonics* 15.8 (2021), pp. 608–613.

[27] G. Gui, N. J. Brooks, B. Wang, H. C. Kapteyn, M. M. Murnane, and C.-T. Liao. "Single-frame characterization of ultrafast pulses with spatiotemporal orbital angular momentum". In: *ACS photonics* 9.8 (2022), pp. 2802–2808.

[28] M. V. Berry. "Geometry of phase and polarization singularities illustrated by edge diffraction and the tides". In: *Second International Conference on Singular Optics (Optical Vortices): Fundamentals and Applications*. Vol. 4403. SPIE. 2001, pp. 1–12.

[29] V. Pas' ko, M. Soskin, and M. Vasnetsov. "Transversal optical vortex". In: *Optics communications* 198.1-3 (2001), pp. 49–56.

[30] P. Liu and B. Lü. "Phase singularities of the transverse field component of high numerical aperture dark-hollow Gaussian beams in the focal region". In: *Optics communications* 272.1 (2007), pp. 1–8.

[31] K. O'holleran, M. J. Padgett, and M. R. Dennis. "Topology of optical vortex lines formed by the interference of three, four, and five plane waves". In: *Optics Express* 14.7 (2006), pp. 3039–3044.

[32] M. R. Dennis, K. O'holleran, and M. J. Padgett. "Singular optics: optical vortices and polarization singularities". In: *Progress in optics*. Vol. 53. Elsevier, 2009, pp. 293–363.

6

[33]   X. Wang, Z. Nie, Y. Liang, J. Wang, T. Li, and B. Jia. "Recent advances on optical vortex generation". In: *Nanophotonics* 7.9 (2018), pp. 1533–1556.

[34]   J. Masajada and B. Dubik. "Optical vortex generation by three plane wave interference". In: *Optics Communications* 198.1-3 (2001), pp. 21–27.

[35]   K. W. Nicholls and J. Nye. "Three-beam model for studying dislocations in wave pulses". In: *Journal of Physics A: Mathematical and General* 20.14 (1987), p. 4673.

[36]   G. Ruben and D. M. Paganin. "Phase vortices from a Young's three-pinhole interferometer". In: *Physical Review E* 75.6 (2007), p. 066613.

[37]   X. Cai, J. Wang, M. J. Strain, B. Johnson-Morris, J. Zhu, M. Sorel, J. L. O'Brien, M. G. Thompson, and S. Yu. "Integrated compact optical vortex beam emitters". In: *Science* 338.6105 (2012), pp. 363–366.

[38]   N. Biton, J. Kupferman, and S. Arnon. "OAM light propagation through tissue". In: *Scientific Reports* 11.1 (2021), p. 2407.

[39]   Z. Xie, T. Lei, F. Li, H. Qiu, Z. Zhang, H. Wang, C. Min, L. Du, Z. Li, and X. Yuan. "Ultra-broadband on-chip twisted light emitter for optical communications". In: *Light: Science & Applications* 7.4 (2018), pp. 18001–18001.

[40]   W. Ren, J. Cui, and J. Tan. "Parallel beam generation method for a high-precision roll angle measurement with a long working distance". In: *Optics express* 28.23 (2020), pp. 34489–34500.

[41]   N. Kumar, P. Petrik, G. K. Ramanandan, O. El Gawhary, S. Roy, S. F. Pereira, W. M. Coene, and H. P. Urbach. "Reconstruction of sub-wavelength features and nano-positioning of gratings using coherent Fourier scatterometry". In: *Optics express* 22.20 (2014), pp. 24678–24688.

[42]   R. Trebino and D. J. Kane. "Using phase retrieval to measure the intensity and phase of ultrashort pulses: frequency-resolved optical gating". In: *JOSA A* 10.5 (1993), pp. 1101–1111.

[43]   R. Barczyk, S. Nechayev, M. A. Butt, G. Leuchs, and P. Banzer. "Vectorial vortex generation and phase singularities upon Brewster reflection". In: *Physical Review A* 99.6 (2019), p. 063820.

[44]   T. Scharf, M.-S. Kim, and H. P. Herzig. "Measuring amplitude and phase of light emerging from microstructures with HRIM". In: *Proceedings SPIE*. Vol. 8082. CONF. SPIE Digital Library. 2011.

[45]   A. Nesci, R. Daendliker, M. Salt, and H. P. Herzig. "Optical near-field phase singularities produced by microstructures". In: *Controlling and Using Light in Nanometric Domains*. Vol. 4456. SPIE. 2001, pp. 68–77.

[46]   M. Totzeck and H. Tiziani. "Phase-singularities in 2D diffraction fields and interference microscopy". In: *Optics communications* 138.4-6 (1997), pp. 365–382.

[47]   M. Eberler, S. Quabis, R. Dorn, and G. Leuchs. "Polarization-dependent effects on phase singularities in the vicinity of sub-lambda structures". In: *Interferometry XI: Techniques and Analysis*. Vol. 4777. SPIE. 2002, pp. 362–370.

6

7

CONCLUSION AND OUTLOOK

7.1. CONCLUSION

In this thesis, we aim to fully leverage the coherent characteristics of the light source for accurate determination of a step-shape nanostructure using far field information.

In Chapter 1, we first gave an overview of the existing metrology methods in the IC manufacturing field and explained their advantages and disadvantages. We provided a comprehensive explanation on the characteristics of phase, polarization, and PB phase in coherent light. Moreover, we systematically introduced the several types of beams that are directly relevant to the subsequent sections, including their mathematical expressions, physical characteristics. This section can be regarded as the foundation theory related to our research.

Chapter 2 can be considered as the recipe for our research endeavors. In this chapter, we presented a semi-analytical approach for addressing scattering problems, including the vectorial diffraction theory to generate the desired source and the numerical simulation method to calculate the interaction between the source and the structure, and finally the Fresnel diffraction integral to obtain the far field of scattering light.

The main contribution of the thesis are laid out in Chapter 3, 4, 5, 6, namely:

- elongating the focused field in the direction perpendicular to the optical axis by shaping the Pancharactnam–Berry (PB) phase;

- studying the influence of the polarization state and the focus position of the incident beam in the estimation of SWAs of a cliff-shape step structure;

- determining parameters of a cliff-shape step structure by using polarization singularity;

- determinatining parameters of a cliff-shape step structure by using phase singularity.

The achievements in this dissertation are encouraging and promising, and the results show that our method can function as a good complement to the CFS technique to improve the parameter retrieval of nanostructures. It is important to note that, although we conduct most analysis with specific source field and selected structures, the principles

of this research are not limited by these conditions but can work under other conditions too. Furthermore, regarding the work we have proposed involving the flexibility in shaping the light field, one may envision many useful applications in ultra-sensitive sensing, information storage and on-chip manufacturing process. Given the effectiveness of our analysis, we hope that this research will open new opportunities for the semiconductor industry as well as other industrial applications.

7.2. Outlook

Regarding the work we have proposed and demonstrated involving optical field shaping and its application in the profile retrieval of nanostructures, we hope that our results will inspire further research in future, considering different types of nanostructures and experimental realizations. In this section, we will discuss possible research topics and focus areas that could be of great interest in continuing research in this field.

Feasible experimental design

In this thesis, we have focused on theoretical and numerical analysis of new ways to determine parameters of nanostructures by shaping the light field that interacts with the structures and detecting the scattered field in the far field. To make the approach more realistic, as well as to test its feasibility and determine its potential in actual industrial applications, real experiments should be performed to calibrate accuracy and limitations of the proposed methods. Recent experimental results [1] on the reconstruction of SWA and height of a step structure using uniform illumination CFS encourage us to believe that our proposed schemes here could also work as well. Furthermore, it will be interesting to compare the effect of using structured beams instead of uniform beam illumination on the reconstruction.

Structured beams such as the one discussed in Chapter 6 can be generated by a spatial light modulator or a specially designed phase mask can be used to generate the three laser beams, which are then incident into an objective lens to generate the focused field with TOSs onto the step structure. The position of the step structure can be controlled by a piezo-electric translation platform to align the structure with the TOS. The scattered TOS field along the y-direction can be collected by another objective lens on the side of the step structure. Then, the scattered field after the objective lens should interfere with an oblique plane wave with the same wavelength to generate the interference fringe field captured by a CCD. Based on this recorded field, the phase distribution of the singular light field can be retrieved by the Fourier-transform method, and thus the spatial location of the singularity can be retrieved. Finally, the trajectory of the TOS can be obtained by scanning the interference field along the scattering direction with a piezo actuator. With the measured intensity distribution of the interference field, the phase distribution can be calculated through two Fourier transformations of the interference field. Thus, information about the singularity can be retrieved for further analysis.

---

[1]A.Paul, J.Rafighdoost, X.Dou and S.F.Pereira."Investigation of coherent Fourier scatterometry as a calibration tool for determination of steep side wall angle and height of a nanostructure", submitted for publication

EFFICIENT METHODS FOR SOLVING INVERSE PROBLEMS

As we all know, the success of optical scatterometry techniques not only relies on the forward optical modeling for nanostructures, but also depends on the process of solving the inverse problems. Our work have given exciting results, but this is just a first step for this topic. In fact, solving the inverse problem is also a very important issue and further research is needed. Consequently, we envision that in future, using artificial intelligence methods to solve the inverse problem in scatterometry by building a comprehensive database based on calculations as presented in this thesis can be used to analyze the experimental data.

7

A

POLARIZATION TRANSFORMATION OF HIGH NA LENSES

The geometric description of the focusing process of a high numerical aperture objective is shown in the Figure A.1.
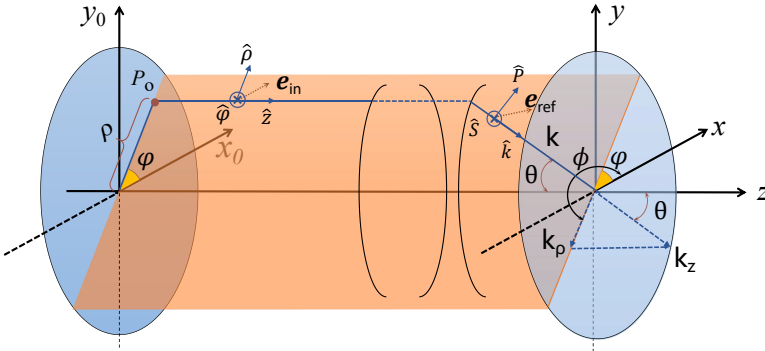
Figure A.1: Schematic of the geometry of the strong focus model

Consider a monochromatic incident wave propagating along the z direction, in other words, z is the direction of the optical axis, extending from object space to image space. An arbitrary point P_o in the object space forms a meridional plane with the optical axis z. $\boldsymbol{e}_{\text{in}}$ represents the incident light field, and $\boldsymbol{e}_{\text{ref}}$ represents the refraction light field through a spherical objective lens, $\hat{k}$ is a unit vector representing the propagation direction of the light in the image space. We assume that $\hat{e}_{\text{in}}$ and $\hat{e}_{\text{ref}}$ are the unit vectors representing the vibration directions of $\boldsymbol{e}_{\text{in}}$ and $\boldsymbol{e}_{\text{ref}}$, and l_{in} and l_{ref} are the amplitude factors, respectively. By accounting for energy conservation, we obtain the apodization function of the lens as

$$l_{\text{ref}} = l_{\text{in}}\sqrt{\cos\theta}. \tag{A.1}$$

The 'strength factor' $a(\theta, \varphi)$ in Equation 2.5 is given by

$$\mathbf{a}(\theta, \varphi) = f\, l_{\text{in}}\sqrt{\cos\theta}\,\hat{e}_{\text{ref}}. \tag{A.2}$$

105

The next crucial step is to get the specific form of $\hat{e}_{\text{ref}}$. We introduce two sets of unit vectors $(\hat{\rho}, \hat{\varphi}, \hat{z})$ and $(\hat{P}, \hat{S}, \hat{k})$, among which $\hat{\rho}$ and $\hat{P}$ are placed in the meridional plane, such that $\hat{\rho}$ is perpendicular to the optical axis z in the object space and $\hat{P}$ is perpendicular to the propagation direction $\hat{k}$ in the image space. Both unit vectors $\hat{\varphi}$ and $\hat{S}$ are perpendicular to the meridional plane and point inward. The reason for using the polar basis in entrance pupil is that the radial component of the electric field in the entrance pupil becomes a P-component of the plane waves behind the lens, while the azimuthal component becomes the S-component of the plane waves. There is no cross-talk between these components. The $\hat{e}_{\text{ref}}$ lies in the plane of $\hat{P}$ and $\hat{S}$, hence

$$\hat{e}_{\text{ref}} = \alpha \hat{P} + \beta \hat{S}, \tag{A.3}$$

where α and β are two constants, and satisfy the relation $\alpha^2 + \beta^2 = 1$. Let (θ_0, ϕ_0) and (θ_1, ϕ_1) be the polar angles of $\hat{\rho}$ and $\hat{P}$, respectively, which can be uniquely determined by (θ, ϕ). From the geometric schematic of Figure A.1, it also clear that $\phi = \varphi + \pi$, evidently

$$\theta_0 = \frac{\pi}{2}, \quad \phi_0 = \phi - \pi = \varphi,$$
$$\theta_1 = \frac{\pi}{2} - \theta, \quad \phi_1 = \phi - \pi = \varphi, \tag{A.4}$$

Then we have

$$\hat{\rho} = \begin{bmatrix} \sin\theta_0 \cos\phi_0 \\ \sin\theta_0 \sin\phi_0 \\ \cos\theta_0 \end{bmatrix} = \begin{bmatrix} \cos\varphi \\ \sin\varphi \\ 0 \end{bmatrix}, \quad \hat{\varphi} = \begin{bmatrix} \sin\theta_0 \sin\phi_0 \\ -\sin\theta_0 \cos\phi_0 \\ \cos\theta_0 \end{bmatrix} = \begin{bmatrix} \cos\varphi \\ \sin\varphi \\ 0 \end{bmatrix}. \tag{A.5}$$

And $\hat{P}$ and $\hat{S}$ are the unit vectors given by

$$\hat{P} = \begin{bmatrix} \sin\theta_1 \cos\phi_1 \\ \sin\theta_1 \sin\phi_1 \\ \cos\theta_1 \end{bmatrix} = \begin{bmatrix} \cos\theta \cos\varphi \\ \cos\theta \sin\varphi \\ \sin\theta \end{bmatrix}, \quad \hat{S} = \begin{bmatrix} \sin\varphi \\ -\cos\varphi \\ 0 \end{bmatrix}. \tag{A.6}$$

According to Debye–Wolf theory, the wave components upon focusing do not change their polarization in local coordinate basis attached to them, namely that as the light traverses the system, the angle between the electric (and also the magnetic) vector and the meridional plane of the ray remains constant, hence

$$\hat{\rho} \bullet \hat{e}_{\text{in}} = \hat{P} \bullet \hat{e}_{\text{ref}},$$
$$\hat{\varphi} \bullet \hat{e}_{\text{in}} = \hat{S} \bullet \hat{e}_{\text{ref}}. \tag{A.7}$$

If the incident beam is paraxial, the input beam has mainly transverse component, while longitudinal component is neglected, it implies that $\hat{e}_{\text{in}}$ has the form of $\hat{e}_{\text{in}}(x, y, 0)$. The unite vector $\hat{e}_{\text{in}}(x, y, 0)$ can be expressed as

$$\hat{e}_{\text{in}}(x, y, 0) = e_{\text{in}}^x \hat{x} + e_{\text{in}}^y \hat{y}, \tag{A.8}$$

By substituting Equation A.3 into Equation A.7, we get

$$\alpha = \hat{\rho} \bullet \hat{e}_{\text{in}} = e_{\text{in}}^x \cos\phi + e_{\text{in}}^y \sin\phi$$
$$\beta = \hat{\varphi} \bullet \hat{e}_{\text{in}} = e_{\text{in}}^x \sin\phi - e_{\text{in}}^y \cos\phi. \tag{A.9}$$

Hence, Eqution A.2 follows the form as

$$\mathbf{a}(\theta,\varphi) = f\, l_{\text{in}} \sqrt{\cos\theta}\, (\alpha \hat{P} + \beta \hat{S}),\tag{A.10}$$

Plugging Equations A.6 and Equations A.9 in Equation A.10 gives

$$\mathbf{a}(\theta,\varphi) = f\, l_{\text{in}} \sqrt{\cos\theta}\, (e_{\text{in}}^{x}\cos\varphi + e_{\text{in}}^{y}\sin\varphi) \begin{bmatrix} \cos\theta\cos\varphi \\ \cos\theta\sin\varphi \\ \sin\theta \end{bmatrix} + (e_{\text{in}}^{x}\sin\phi - e_{\text{in}}^{y}\cos\phi) \begin{bmatrix} \sin\varphi \\ -\cos\varphi \\ 0 \end{bmatrix}$$

$$= f\, l_{\text{in}} \sqrt{\cos\theta}\, \begin{bmatrix} e_{\text{in}}^{x}\{\cos\theta + \sin^{2}\varphi(1-\cos\theta)\} + e_{\text{in}}^{y}\{\cos\varphi\sin\varphi(\cos\theta - 1)\} \\ e_{\text{in}}^{x}\{\cos\varphi\sin\varphi(\cos\theta - 1)\} + e_{\text{in}}^{y}\{1 - \sin^{2}\varphi(1-\cos\theta)\} \\ e_{\text{in}}^{x}\sin\theta\cos\varphi + e_{\text{in}}^{y}\sin\theta\sin\varphi \end{bmatrix}$$
$$\tag{A.11}$$

According to the Equation 2.3, the 'strength factor' $b(\theta,\varphi)$ of magnectic field can be write as

$$\mathbf{b}(\theta,\varphi) = \sqrt{\frac{\varepsilon}{\mu}} f\, l_{\text{in}} \sqrt{\cos\theta}\, \hat{k} \times a(\theta,\varphi)$$

$$= \sqrt{\frac{\varepsilon}{\mu}} f\, l_{\text{in}} \sqrt{\cos\theta}\, \begin{bmatrix} -e_{\text{in}}^{y}\{\cos\theta + \sin^{2}\varphi(1-\cos\theta)\} + e_{\text{in}}^{x}\{\cos\varphi\sin\varphi(\cos\theta - 1)\} \\ -e_{\text{in}}^{y}\{\cos\varphi\sin\varphi(\cos\theta - 1)\} + e_{\text{in}}^{x}\{1 - \sin^{2}\varphi(1-\cos\theta)\} \\ -e_{\text{in}}^{y}\sin\theta\cos\varphi + e_{\text{in}}^{x}\sin\theta\sin\varphi \end{bmatrix}$$
$$\tag{A.12}$$

ACKNOWLEDGEMENTS

It has taken me six and a half years to get here, and there is so much I want to say but I do not know where to start. Looking back at the years, the fragments of memory flashed through my brain, bringing many emotions to my heart. During the PhD there was little time for fun and most of the time was a laborious exploration. But someone told me that things that are truly worthwhile are likely to be difficult. On the completion of my thesis, I would like to acknowledge many people who gave me immense help and support in this long, long journey.

First and foremost, I would like to give my heartfelt thanks to my promotors of the Delft University of Technology, Prof. Paul Urbach and, Dr. Silvania Pereira. Paul, thank you for your constructive and insightful comments on my research and thesis, which have been very enlightening to me. I greatly admire your achievements in theoretical optics, which have helped me to have a deeper understanding of my own work. You are serious and conscientious in research, and you are tolerant and humorous in life. Thank you for teaching me how to properly respond to scientific inquiries and how to roll my tongue. I extend my appreciation to Silvania for her constant guidance and support, and for being the most important person during my whole PhD. Silvania, you participated in all my research work and provided me with abundant help; you kept track of my progress and gave me critical advice; you always encouraged me and responded promptly to my needs. I highly appreciate your incredible patience, enormous efforts and great responsibility. It is my luck to have you as my promotor and supervisor.

I would like to give my tremendous thanks to my promotor, Prof. Xiaocong Yuan, and daily supervisor, Prof. Changjun Min, of the Shenzhen University. Prof. Yuan was also my promotor during my master, and nearly one third of my life so far has been spent under his guidance. His farsighted wisdom, broad academic vision, rigorous academic attitude and noble ethics have a profound impact on my academic career. Prof. Yuan, I thank you for everything you have taught me, I would not be here without your support from the beginning to the end. I also want to express my gratitude to Prof. Min, who has a solid academic foundation, open academic thinking and a gentle disposition. Prof. Min, thank you for your selfless help and patient guidance, you have always been my role model. I am also grateful to Prof. Zhongsheng Man and Prof. Yuquan Zhang for their patient answers and inspiration when I was confused. Moreover, special thanks to all members of the thesis committee for their careful reading and valuable feedback.

I would like to thank the staff and faculty in the Optics Research Group. Yvonne van Aalst and Lidija Nikolic, our former and current group assistant, thank you both for helping me survive through the cumbersome administrative problems. I also want to express my particular thanks to Yvonne for her help when I was dealing with a case of rent fraud. She accompanied me to the police office and quickly helped me find an apartment through the university. Yvonne gave me tremendous help in my life in Delft. Thank

CURRICULUM VITÆ

Xiujie DOU

27-02-1991   Born in Xingtai, China.

EDUCATION

2009–2013   B.Sc. in Optical information Science and Technology
The College of Post and Telecommunication of WIT
Wuhan, China

2014–2017   M.S. in Optical Engineering
Nanophotonics Research Centre (NRC), Shenzhen University
Shenzhen, China

2017   PhD. in Physics
Optics Research Group, Delft University of Technology
Delft, The Netherlands
Thesis: Coherent Forier Scatterometry
Promotor: Prof. dr. H. P. Urbarch
Prof. dr. X.C. Yuan
Assoc. Prof. dr. S. F. Pereira

AWARDS

2018   First prize of NRC, Shenzhen University

2017   Outstanding graduates of Shenzhen University

Grand prize of NRC, Shenzhen University

2016   National Postgraduate Student Scholarship

Excellent Postgraduate Student Award of Shenzhen University

Grand prize of NRC, Shenzhen University

LIST OF PUBLICATIONS

Journal Publications

14. A.Paul, J.Rafighdoost, **X.Dou** and S.F.Pereira."Investigation of coherent Fourier scatterometry as a calibration tool for determination of steep side wall angle and height of a nanostructure". In: *Measurement Science and Technology* (2024). (**Accepted**)

13. **X. Dou**, J. Zhou, Y. Zhang, C. Min, S. F. Pereira, and X. Yuan. "Transversal optical singularity induced precision measurement of step-nanostructures". In: *Optics Express* 31.20 (2023), pp. 32840–32848.

12. **X. Dou**, C. Min, Y. Zhang, S. F. Pereira, and X. Yuan. "Optical singularity assisted method for accurate parameter detection of step-shaped nanostructure in coherent Fourier scatterometry". In: *Optics Express* 30.16 (2022), pp. 29287–29294.

11. **X. Dou**, S. F. Pereira, C. Min, Y. Zhang, P. Meng, H. P. Urbach, and X. Yuan. "Determination of steep sidewall angle using polarization-sensitive asymmetric scattering". In: *Measurement Science and Technology* 32.8 (2021), p. 085201.

10. Y. Zhang, C. Min, **X. Dou**, X. Wang, H. P. Urbach, M. G. Somekh, and X. Yuan. "Plasmonic tweezers: for nanoscale optical trapping and beyond". In: *Light: Science & Applications* 10.1 (2021), p. 59.

9. Z. Man, **X. Dou**, and H. P. Urbach. "The evolutions of spin density and energy flux of strongly focused standard full Poincaré beams". In: *Optics Communications* 458 (2020), p. 124790.

8. P. Meng, S. F. Pereira, **X. Dou**, and H. P. Urbach. "Superresolution effect due to a thin dielectric slab for imaging with radially polarized light". In: *Optics Express* 28.14 (2020), pp. 20660–20668.

7. Z. Man, **X. Dou**, and S. Fu. "Pancharatnam–Berry phase shaping for control of the transverse enhancement of focusing". In: *Optics Letters* 44.2 (2019), pp. 427–430.

6. Y. Zhang, **X. Dou**, Y. Dai, X. Wang, C. Min, and X. Yuan. "All-optical manipulation of micrometer sized metallic particles". In: *Photonics Research* 6.2 (2018), pp. 66–71.

5. A. Yang, L. Du, **X. Dou**, F. Meng, C. Zhang, C. Min, J. Lin, and X. Yuan. "Sensitive gap-enhanced Raman spectroscopy with a perfect radially polarized beam". In: *Plasmonics* 13 (2018), pp. 991–996.

4. **X. Dou**, A. Yang, C. Min, L. Du, Y. Zhang, X. Weng, and X. Yuan. "Polarization-controlled gap-mode surface-enhanced Raman scattering with a single nanoparticle". In: *Journal of Physics D: Applied Physics* 50.25 (2017), p. 255302.

3. Y. Zhang, **X. Dou**, Y. Yang, C. Xie, J. Bu, C. Min, and X. Yuan. "Flexible generation of femtosecond cylindrical vector beams". In: *Chinese Optics Letters* 15.3 (2017), p. 030007.

2. Y. Zhang, J. Shen, Z. Xie, **X. Dou**, C. Min, T. Lei, J. Liu, S. Zhu, and X. Yuan. "Dynamic plasmonic nano-traps for single molecule surface-enhanced Raman scattering". In: *Nanoscale* 9.30 (2017), pp. 10694–10700.

1. L. Zhang, **X. Dou**, C. Min, Y. Zhang, L. Du, Z. Xie, J. Shen, Y. Zeng, and X. Yuan. "In-plane trapping and manipulation of ZnO nanowires by a hybrid plasmonic field". In: *Nanoscale* 8.18 (2016), pp. 9756–9763. (**Equal contribution first author**)

Conference Proceedings

2. **X. Dou**, C. Min, L. Zhang, Y. Zhang, and X. Yuan. "Dynamic plasmonic trapping and manipulation of nanoparticles and nanowires". In: *CLEO: QELS_Fundamental Science*. Optica Publishing Group. 2016, FM2B–7.

1. L. Zhang, **X. Dou**, C. Min, Y. Zhang, and X. Yuan. "In-plane trapping and manipulation of ZnO nanowires on a metallic surface". In: *CLEO: QELS_Fundamental Science*. Optica Publishing Group. 2016, JW2A–90.

Conference Presentations and Posters

3. "Transversal optical singularity assisted precision measurement of nanostructures," oral presentation at the 14th International Conference on Information Optics and Photonics (CIOP), Xi'an, China, (August 2023).

2. "The application of structure light field in the determination of step-shape nanostructures," poster presentation at the 15th National Conference on Laser Technology and Optoelectronics (LTO), Shanghai, China, (October 2020).

1. "Study of determination of steep side wall angles based on far field measurements," poster presentation at the European Optical Society Biennial Meeting (EOSAM), Delft, the Netherlands (October 2018).